THE UNIVERSITY *of* EDINBURGH

Molecular simulation studies of gas adsorption and separation in metal-organic frameworks

Peyman Zoroufchian Moghadam

PhD

The University of Edinburgh
Institute for Materials and Processes

2012

Declaration

I hereby declare that this thesis is my own work and effort except where acknowledged in the text. This work has not been submitted for any other degree and it was carried out entirely by myself in the School of Engineering, The University of Edinburgh.

Peyman Zoroufchian Moghadam

Abstract

Adsorption in porous materials plays a significant role in industrial separation processes. Here, the host-guest interaction and the pore shape influence the distribution of products. Metal-organic frameworks (MOFs) are promising materials for separation purposes as their diversity due to their building block synthesis from metal corners and organic linker gives rise to a wide range of porous structures. The selectivity differs from MOF to MOF as the size and shapes of their pores are tuneable by altering the organic linkers and thus changing the host-guest interactions in the pores.

Using mainly molecular simulation techniques, this work focuses on three types of separations using MOFs. Firstly, the experimental incorporation of calix[4]arenes in MOFs as a linker to create additional adsorption sites is investigated. For a mixture of methane and hydrogen, it is shown that in the calix[4]arene-based MOFs, methane is adsorbed preferentially over hydrogen with much higher selectivities compared to other MOFs in the literature. Remarkably, it was shown that extra voids created by calix[4]arene-based linkers, were accessible to only hydrogen molecules. Secondly, the strong correlation between different pore sizes and shapes in MOFs and their capabilities to separate xylene isomers were investigated for a number of MOFs. Finally, the underlying molecular mechanism of enantioseparation behaviour in a homochiral MOF for a number of chiral diols is presented. The simulation results showed good agreement with experimental enantioselectivity values. It was observed that high enantioselectivity occurs only at high loadings and when a perfect match in terms of size and shape exists between the pore size and the adsorbates.

Ultimately, the information obtained from molecular simulations will further our understanding of how network topology, pore size and shape in MOFs influence their performance as selective adsorbents for desired applications.

Acknowledgments

First and foremost I would like to thank my supervisor Tina Düren. It has been an honour working in her group. I appreciate all her contributions of time, advice and ideas from beginning to the end that made this thesis possible. I am truly grateful for her patience, enthusiasm and guidance that made her a great mentor.

I would like to thank David Fairen-Jimenez for his valuable suggestions and for the wonderful conversations we had on science and social aspects. I also want to thank our collaborators Andrew Burrows and Vio Sebestyen, University of Bath, and Sean Bew's group, University of East Anglia, for their help with the organic linker synthesis. I am grateful to all my colleagues from the Institute for Materials and Processes for their insights, friendship and support. I am especially grateful to Ana Banu, Naomi Cessford, Linjiang Chen, Carlos Ferreiro, Zoe Kapetaki, Matthew Lennox, Payam Malek and Jennifer Williams. My special thanks to Noushin Moharrami for her encouragements and selflessly helping me during my PhD. I am beyond grateful to my parents and my brothers Yasser and Pejman for their faith and support.

Finally, I wish to acknowledge the University of Edinburgh employees, especially those who provided help with my simulations in computer clusters CLX, VLX and EDDIE. I thank EPSRC for providing financial support to this research project.

Table of Contents

Chapter 1 Introduction

Adsorptive storage and separation is widely used in industry. Porous adsorbents such as zeolites, activated carbons and silica gels play a pivotal role for adsorptive separation processes, as different interactions of adsorbates with the internal surfaces determines the separation performance (Li *et al.* (2009)). This performance is directly related to adsorption kinetics and equilibrium characteristics. Increasing demand for more economic, efficient, and environmentally friendly adsorptive processes has lead to development of numerous novel adsorbents. Among these, metal-organic frameworks (MOFs) have attracted a great attention recently (Ma (2009)). MOFs are built in a self-assembly process from a combination of metal clusters and organic linkers and can be highly porous. Due to the numerous structures, pore shapes, sizes and topologies formed by different building blocks, it is possible to target the synthesis of a MOF for a particular application. The pore size and shape in MOFs can be controlled through for example changing the metal cluster, linker length, or functionalising the organic linker to tailor the pore surface chemistry for desired applications. Therefore, the pores created in these structures provide a great deal of opportunities for new functional materials especially in gas adsorption and separation applications (Schröder (2010)).

Since a large number of MOFs has already been synthesised and many more are possible, experimental analysis and screening for appropriate applications becomes a formidable task. As a different approach, molecular simulations can provide molecular level information and theoretical guidelines that are not often accessible or difficult to obtain in experiments. Molecular simulations are well suited to study interactions between adsorbates and MOFs. From simulation results, useful information such as adsorption isotherms, favourable adsorption sites, interaction energies, selectivities as well as dynamical properties such as diffusion coefficients can be obtained and compared with experimental data where available. In this regard, computational screening of MOFs in different process conditions can be investigated by means of molecular simulations (Greathouse *et al.* (2010)) even for hypothetical materials (Wilmer *et al.* (2012)) without the need for expensive and time consuming

experiments. Ultimately, the simulation results will be used to predict target structures with optimal properties for different separation purposes. The objective of this research is to investigate how the pore space and therefore adsorption and diffusion of adsorbates in MOFs is affected by the size, shape and surface functional groups of the ligands using molecular simulations. The obtained information provides atomistic insight into the performance of different MOFs for the separation of three mixtures: hydrogen / methane, xylene isomers and different enantiomeric diols.

1.1 Outline of the thesis

This thesis is divided into six chapters and is structured as follows:

Chapter 2 gives an overview to porous materials and MOFs and describes why MOFs are promising adsorbents for storage and separation applications.

In Chapter 3, MOFs containing tert-butylcalix[4]arene-based ligands are introduced. These MOFs, which have been synthesised as part of this work, are hierarchically-porous materials with two levels of porosity associated with both the ligand and the structural framework itself. The synthesised MOFs are carefully characterised using both experimental and computational methods. Additionally, molecular simulation of competitive adsorption and diffusion of methane and hydrogen is investigated.

In Chapter 4, a number of MOFs are assessed for their potential for the separation of xylene isomers. The MOFs are categorised according to their pore diameters into large, medium and small pore MOFs and each category is tested for preferential adsorption of xylene isomers using grand canonical Monte Carlo simulations. The influence of pore size as well as ligands and functional groups on selectivity is also presented.

In Chapter 5, the enantioselectivity of a homochiral metal-organic framework [Ni_2(L-asp)$_2$(bipy)] for a number of chiral diol molecules is probed and the results are compared to experimental data from the literature. Racemic mixture adsorption and single component isotherms are studied using configurational-biased grand canonical Monte Carlo simulations. The relationship between enantioselectivity and size and shape of the chiral diols are examined. In addition, the influence of the framework channel size on enantioselectivity is reported.

The closing chapter, Chapter 6, contains a summary of this work, conclusions, and suggestions for future work.

1.2 Publications and presentations

Parts of this thesis have been reported in the following publications and presentations:

Publications

P. Z. Moghadam and T. Düren "*Origin of Enantioselectivity in A Chiral Metal-Organic Framework: A Molecular Simulation Study*", Journal of Physical Chemistry C, 116 (39), 20874-20881, 2012

S. P. Bew, A. D. Burrows, T. Düren, M. F. Mahon, P. Z. Moghadam, V. M. Sebestyen, S. Thurston "*Calixarene-based Metal-Organic Frameworks: Towards Hierarchically Porous Materials*", Chemical Communications, 48, 4824-4826, 2012

F. Vermootele, M. Maes, P. Z. Moghadam, M. J. Lennox, F. Ragon, M. Boulhout, S. Biswas, K. G. M. Laurier, I. Beurroies, R. Denoyel, M. Roeffaers, N. Stock, T. Düren, C. Serre, D. E. De Vos, "*p-Xylene Selective Metal-Organic Frameworks: A Case of Topology-Directed Selectivity*", Journal of American Chemical Society, 133 (46), 18526-18529, 2011

Conference presentations:

3rd International Conference on Metal-Organic Frameworks and Open Framework Compounds; Edinburgh, UK. September 2012, Poster presentation "*Origin of Enantioselectivity in A Chiral Metal-Organic Framework: A Molecular Simulation Study*" P. Z. Moghadam and T. Düren

35th Annual British Zeolite Association Conference. Chester, UK. August 2012, Poster presentation, "*Origin of Enantioselectivity in A Chiral Metal-Organic Framework: A Molecular Simulation Study*" P. Z. Moghadam and T. Düren

34th Annual British Zeolite Association Conference. Edinburgh, UK. April 2011, Oral presentation, "*Molecular Simulation Studies of Xylene Separation in Metal-Organic Frameworks*" P. Z. Moghadam, M. J. Lennox and T. Düren

2nd International Conference on Metal-Organic Frameworks and Open Framework Compounds; Marseille, France. September 2010, Poster presentation "*Molecular Simulation Studies of Liquid Adsorption in Metal-Organic Frameworks*" P. Z. Moghadam and T. Düren

CECAM Workshop "Gas separation and gas storage using porous materials", Lausanne, Switzerland. May 2010, Poster presentation "*Catalytic Applications of Metal-Organic Frameworks*" P. Z. Moghadam and T. Düren

Chapter 2 Materials and Methodology

Porous materials with large internal surface areas serve as a host for different applications, for example; gas storage, mixture separation and catalysis ((Dunne and Manos (2009), Čejka (2012)). Guest-host interactions in porous materials decisively influence the molecular transport and adsorption mechanisms occurring in the pores. This is why controlling the pores size, shape and assembly of their building blocks is one of the most challenging areas in chemistry of these materials. Porous materials are classified by their pore size according to the International Union of Pure and Applied Chemistry (IUPAC) (Rouquerol *et al.* (1994)):

- Microporous materials have pore diameters of less than 20 Å
- Mesoporous materials have pore diameters between 20 and 500 Å
- Macroporous materials have pore diameters greater than 500 Å

The pore size can play a crucial role in the adsorption and diffusion of adsorbates and consequently on their final separation performance. In micropores, where the adsorbate size and pore size is comparable, van der Waals and electrostatic interactions of guest molecules and pore walls as well as guest-guest interactions become significant making them good candidates for gas storage and separation applications. In these conditions, preferential adsorption, steric hindrance and molecular sieving effects can all contribute to the separation of different adsorbate molecules. In mesopores, interactions between adsorbates occur more frequently compared to weaker interactions between adsorbates and the framework walls but high adsorption capacity is still achievable. In macropores, the specific surface area is very small and they hardly play a role in adsorption.

One class of novel porous materials that has attracted interest in both academia and industry is metal-organic frameworks (MOFs). Currently, MOFs are being extensively studied to exploit their unique properties and compared with traditional materials such as zeolites that are widely used in industry.

2.1 Metal-organic Frameworks

Metal-organic frameworks (MOF) or coordination polymers are a rather new class of porous materials that have attracted considerable attention. MOFs are comprised of metal clusters linked together with organic linkers (Figure 2-1) that form periodic porous structures with often high porosities (up to 90 %), large surface area (up to 6500 m^2/g) and various geometries (Xuan *et al.* (2012), Pham *et al.* (2011)). By choosing from a wide range of organic linkers and metals, MOFs can – in principle – be designed for specific applications making them for example size and shape selective. This type of pore structure flexibility is absent from more traditional microporous materials such as zeolites or activated carbons which have been in use for a long time in many industrial applications such as separation and catalysis (Kulprathipanja (2010)). Moderate heat of adsorption in MOFs also allows for regeneration and thermal desorption of MOF-based adsorbents. In comparison to zeolites which have pure inorganic, robust structures, MOFs may not be well suited for separation processes under extreme industrial conditions due to their relatively lower hydrothermal stability (Lee *et al.* (2009)). The stability in MOFs is affected by the composition of the metal clusters as well as its coordination with the organic linker that can define its thermal stability. Flexibility and chemical functionality of the linkers can also influence the structural stability in MOFs (Kang *et al.* (2011)). Under milder conditions MOFs unique properties can target separations in gas and liquid phase, more valuable reactions such as the production of chiral chemical compounds and delicate materials used as feedstocks for pharmaceutical and fine chemical industries (Huxford *et al.* (2010), Seo *et al.* (2000), Xie *et al.* (2011)).

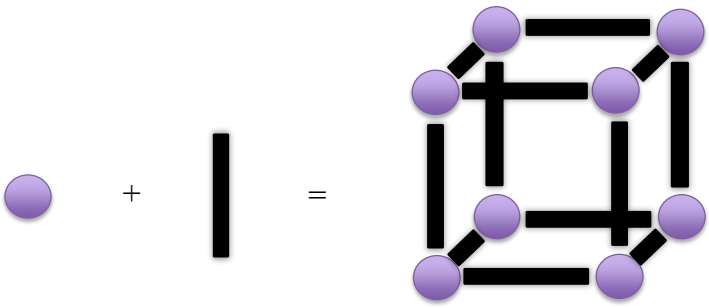

Figure 2-1: Schematic representation of metal-organic frameworks with metal clusters (spheres) and organic linkers (rods).

MOFs are normally synthesised by solvothermal syntheses, where metal salts are treated with the corresponding organic linkers in a suitable solvent at high temperature as well as lower temperatures (i.e. room temperature) (Tranchemontagne *et al.* (2008)). For many potential applications in MOFs, it is necessary that the pores or channels are present and accessible to guest molecules after synthesis. However, some MOFs are prone to partial or full collapse of their structures upon the removal of guest molecules such as solvents. Therefore, the available surface area and adsorption performance in MOFs is highly influenced by the synthesis and activation methods (Hafizovic *et al.* (2007)). This is also why care should be taken into consideration when experimental results are compared with simulation results where solvent-free perfect rigid crystals are often used to study the adsorption in MOFs (Li *et al.* (2012)).

While much of the research on MOF applications has focused on gas storage (Murray *et al.* (2009), Konstas *et al.* (2012)) and CO_2 capture (Yazaydin *et al.* (2009), Xiang *et al.* (2012)) by selective adsorption, more recently there has been interest in variety of other separation applications and catalytic properties (Wee *et al.* (2011), Dhakshinamoorthy *et al.* (2012), Li *et al.* (2009), Schröder (2010)). Owing to their tuneable functionalities, in the past few years, MOFs have been also studied for chiral separation (Xie *et al.* (2011)), as well as biological and medical applications such as drug delivery (McKinlay *et al.* (2010)) and delivery of biologically active gases like nitric oxide (Hinks *et al.* (2010)). In this regard, finding innovative, theoretical strategies for optimal usage of existing MOFs and smart synthesis of new MOFs for different applications is very attractive.

Understanding the guest-host interaction in MOFs is the key to targeted design of sorption and separative properties and applications in molecular recognition systems. Molecular simulations can provide not only reliable and fast predictions of adsorption and diffusion of guest molecules in porous materials, but also give detailed molecular-level insight into different structural information and interaction mechanisms that are impossible to obtain by experiments alone.

2.2 Molecular Simulations

2.2.1 Statistical Mechanics

A principal aim of molecular simulation is to calculate the macroscopic behaviour of a system based on microscopic interaction models between molecules. Statistical mechanics relates these microscopic properties to macroscopic properties. A basic concept in statistical mechanics is the ensemble. An ensemble is the collection of all possible microstates of a N body system. A microstate or snapshot of a system contains complete information about the positions and momenta of all molecules and atoms. On the macroscopic level, the system is characterised by averages across the ensemble. It is common to refer to an ensemble by the set of thermodynamic constraints that define its macroscopic state. Some important ensembles are:

- Microcanonical ensemble (*NVE*): the system is isolated with fixed number of molecules, volume and energy
- Canonical ensemble (*NVT*): the system is connected to a heat bath with fixed number of molecules, volume and temperature
- Isothermal-isobaric ensemble (NPT): where the number of molecules, pressure and temperature are constant
- Grand-canonical ensemble (μVT): where the number of molecules is allowed to fluctuate while the chemical potential, volume and temperature are kept constant

Equilibrium thermodynamic observables can be measured by averaging the properties of an ensemble. In a molecular dynamics simulation, each microstate is obtained from the previous one by solving the equations of motion and the microstates are averaged over time. In Monte Carlo simulations, large numbers of microstates in the phase space that correspond to the same macroscopic system are averaged defining the ensemble average. The fundamental hypothesis of statistical mechanics states that the ensemble exhibits the same average properties in space as a single system exhibits in time. Consequently, the time-average and the ensemble-average are the same and the system is “ergodic” (Hill (1960)).

A given macroscopic observable A can be calculated by summing up the corresponding microstate property A_i for all possible states weighted with the probability of observing the system in a microstate P_i :

$$\langle A \rangle = \sum A_i P_i \qquad \textbf{2-1}$$

Where $\langle ... \rangle$ denotes the ensemble average. In the canonical ensemble where the number of molecules N , volume V and the temperature T are constant the probability of a microstate i to occur with energy E in a system is given by:

$$P_i = \frac{1}{Q_{NVT}} e^{(-\beta E_i)} \qquad \textbf{2-2}$$

with $\beta = \frac{1}{k_B T}$, where k_B is the Boltzmann constant and Q_{NVT} is the partition function for the canonical ensemble which is defined as the sum over all microstates in the system with N particles:

$$Q_{NVT} = \sum_{i,N} e^{(-\beta E_i)} \qquad \textbf{2-3}$$

Substituting equation 2-2 into equation 2-1 gives:

$$\langle A \rangle_{NVT} = \frac{1}{Q_{NVT}} \sum_{i,N} A_i e^{(-\beta E_i)} \qquad \textbf{2-4}$$

The classical equivalent of the above quantum Boltzmann distribution (the exponential term in equation 2-4) for a system becomes an integral over all positions and momenta where a point in the phase space corresponds to a microstate. The total energy E can be separated into the kinetic energy which depends on the momenta, and the potential energy which depends on the positions of the particles, so that equation 2-4 becomes:

$$\langle A \rangle_{NVT} = \frac{1}{Q_{NVT}} \sum_{N} \frac{1}{N!} \frac{V^N}{\Lambda^{3N}} \int dr^N A(r^N) e^{-\beta U} \qquad \textbf{2-5}$$

where Λ is the De Broglie wave length which is derived from the integration of the momentum part of partition function for a monatomic gas and is given by:

$$\Lambda = \sqrt{\beta h^2 / 2\pi m} \qquad \text{2-6}$$

where h is Planck's constant and m is the mass of the molecule.

The calculation of equation 2-5 is not straight forward as numerical integration is not feasible for large systems. Monte Carlo methods are therefore employed.

2.2.2 Monte Carlo simulations

A Monte Carlo integration in its simplest form samples the microstates uniformly. This means that the sampling points are evenly spread over the integration and their contribution to the integral value is unweighted. However, most randomly generated configurations will have negligible Boltzmann weight ($e^{-\beta U}$) for example due to particle overlap which is not energetically favourable. Hence, to improve the efficiency of this approach, it would be preferable if computational time is not spent on low-probability states that do not contribute to the average and focus sampling on important configurations instead, which make significant contributions to the partition function and ensemble averages. This is called importance sampling. To visit states with the correct frequency, the Metropolis Monte Carlo algorithm is used (Metropolis *et al.* (1953)). In this algorithm, a Markov chain of configurations/states is constructed. A Markov chain is a sequence of trials that satisfies two conditions:

- The outcome of each trial belongs to a finite set of outcomes.
- The outcome of each trial depends only on the outcome of the trial that immediately precedes it.

An important property of such a Markov chain of trials is that it can be generated in such a way that its limiting distribution tends towards a fixed distribution. The Metropolis method produces the same result as a simple Monte Carlo integration, but it is much faster when the average properties of systems with large number of accessible states are calculated. For example in an NVT ensemble, a starting (old) configuration is drawn from a Boltzmann distribution. A new configuration (n) is created by randomly moving a randomly selected particle from the old state (o). The

resulting change in potential energy ΔU is calculated. This move is always accepted unconditionally if the new state results in lower potential energy. Otherwise, the move is accepted or rejected with a probability defined by the Boltzmann factor:

$$acc(o \rightarrow n) = \min(1, e^{-\beta \Delta U}) \qquad \textbf{2-7}$$

If a trial move is rejected, the system retains its old configuration.

The move probabilities consist of trial probability and acceptance probability. The trial probability of different moves must ensure efficient sampling of the system. The acceptance probability depends on the energy difference between the old and the new state governed by detailed balance rules that guarantees desired equilibrium probability distribution of generated configurations (Frenkel and Smit (2002)).

The ensemble used in adsorption studies is the grand-canonical ensemble, where the chemical potential is constant and the number of molecules is allowed to change and the corresponding Monte Carlo method is called grand-canonical Monte Carlo (GCMC) method. Therefore, the simulation of this ensemble must permit trial insertions and deletions of the molecules to yield configurations according to GCMC probabilities.

2.2.3 Grand-canonical Monte Carlo simulation of adsorption

For a system where a fluid is adsorbing in a porous material, the grand-canonical Monte Carlo technique is used to determine the equilibrium properties where the chemical potential μ, volume V and temperature T are kept fixed while the number of molecules fluctuates to mimic adsorption experiments where the adsorbed phase is in equilibrium with the bulk phase. The configurations are generated by creating random moves inside the simulation box according to probabilities, just as in the case of MC in the canonical ensemble, based on statistical mechanics. These trial moves include particle insertion, deletion, translation, and rotation. After the equilibrium is reached, the thermodynamical properties are computed as averages over a large

number of configurations in the simulation. Equation 2-5 for the μVT ensemble becomes:

$$\langle A \rangle_{\mu VT} = \frac{1}{\Xi_{\mu VT}} \sum_N \frac{1}{N!} \frac{V^N}{\Lambda^{3N}} \int dr^N A(r^N) e^{\beta(N\mu - U)} \quad \textbf{2-8}$$

Where the partition function $\Xi_{\mu VT}$ in the grand-canonical ensemble is defined as the sum of all possible microstates:

$$\Xi_{\mu VT} = \sum_N Q_{NVT} e^{\beta N \mu} \quad \textbf{2-9}$$

Here the chemical potential, μ, is related to the fugacity of the bulk phase, f, which is normally used as input for GCMC simulations, by:

$$\mu = \frac{1}{\beta} \ln(\beta f \Lambda^3) \quad \textbf{2-10}$$

When the canonical partition function in equation 2-9 is expanded, the ratio of $\frac{e^{\beta\mu}}{\Lambda^3}$ gives the activity z.

$$z = \frac{e^{\beta\mu}}{\Lambda^3} \quad \textbf{2-11}$$

As mentioned earlier, in GCMC simulations, to impose constant chemical potential, fluctuations in the number of molecules N are required. This is achieved by random particle insertions or deletions. When a particle is inserted, the number of molecules increases from N to $N+1$ with an acceptance probability of:

$$acc(o \to n) = \min\left(1, \frac{p(N+1)}{p(N)} = \frac{zVe^{-\beta\Delta U}}{(N+1)}\right) \quad \textbf{2-12}$$

Similarly, when a particle is deleted, the number of molecules decreases from N to $N-1$ with an acceptance probability of:

$$acc(o \to n) = \min\left(1, \frac{p(N-1)}{p(N)} = \frac{Ne^{-\beta\Delta U}}{zV}\right) \quad \textbf{2-13}$$

The acceptance probability of conventional insertion/deletion moves becomes very low for larger flexible molecules and normal GCMC becomes time consuming and unfeasible. Therefore, in order to efficiently create trial configurations of flexible chain molecules, the configurational-bias grand-canonical Monte Carlo (CBGCMC) is applied to simulate the adsorption of these systems. In this method, the molecular conformation is grown segment by segment biasing the growth towards energetically favourable conformations. When CBGCMC is used, the energy of segments and their so-called Rosenbluth weights are calculated and are used instead of Boltzmann factor when the new configuration is compared with the old configuration in the acceptance rules. For a more complete discussion about this technique and other molecular simulation techniques used in this work, the reader is referred to standard textbooks on molecular simulations such as Allen and Tildesley (1989), Rapaport (1995), Haile (1997), Frenkel and Smit (2002).

2.2.4 Molecular Dynamics

The motion of atoms in the porous materials is an inherent property to all physical and chemical properties such as temperature and pressure. Molecular dynamics is a deterministic computational technique used to estimate equilibrium and transport properties, generating successive configurations by solving the classical equations of motion for a molecular many-body system. Like Monte Carlo, the system interacts through a pair potential function but allows prediction of dynamic properties by calculating the points in the ensemble sequentially in time.

Molecular dynamics proceeds iteratively by calculating the force simply according to classical Newton's equation of motion:

$$F_i = m_i a_i = m_i \frac{d^2 r_i(t)}{dt^2} \qquad \textbf{2-14}$$

Where $r_i(t) = (x_i(t), y_i(t), z_i(t))$ is the position vector of the *i*-th atom, F_i is the force acting upon *i*-th atom at time *t*, m_i is the mass of the atom, and a_i is the acceleration which is the second derivative of position with respect to time. The

force is calculated for each atom from the gradient of the potential energy $U(r^N)$ with respect to the change in their positions.

$$F_i = -\frac{\partial}{\partial r_i} U(r^N) \qquad \textbf{2-15}$$

The interaction energies are calculated using force fields (see section 2.2.6). The trajectory of a molecule is computed through the course of simulation (i.e. in the order of picoseconds (10^{-12} seconds)) by successively solving the equations of motions using a specified time step Δt which is typically in the order of femtoseconds (10^{-15} seconds). Numerical methods such as Verlet, velocity-Verlet and leapfrog algorithms have been developed to integrate the equations of motion and calculate the trajectories. All these algorithms approximate the positions, velocities and accelerations by Taylor series expansions. The simulation has to run for a certain time until the system has equilibrated. After equilibration, the final step of the simulation is to run the simulation in the production period for the desired length of time. It is during this period that thermodynamic properties are averaged. Similar to Monte Carlo simulations, molecular dynamics simulations can be run in different ensembles. For example in an NVT ensemble, a heat bath is used in a way that the motion of particles is coupled to a thermostat in order to conserve the average kinetic energy. The Nosé-Hoover thermostat is one of the main temperature coupling methods and is thoroughly discussed in molecular dynamics textbooks (Rapaport (1995)).

As discussed before, during a molecular dynamics simulation the positions of the molecules are calculated as a function of time. During this process, desired parameters such as the mean-squared-displacement (MSD) can be calculated. From these data, elementary mechanisms of diffusion on a microscopic scale can be reliably calculated.

According to Fick's law of diffusion the macroscopic flux of species is related to the negative gradient of macroscopic loading or concentration with the transport

diffusivity coefficient (Krishna (2009), Kärger and Ruthven (1992)). While for this type of diffusivity a gradient of chemical potential is necessary, self-diffusion is an equilibrium process. Self-diffusivity (D_s) measures the travelled distance of a labelled species when the system is in equilibrium i.e. it describes Brownian motion. According to the Einstein equation (Equation 2-16) in a three-dimensional system such as a crystal, D_s can be related to the mean square displacement (MSD) of the labelled species.

$$< r^2(t) >= \frac{1}{N} \sum (r_i(t))^2 = 6D_s t \qquad \textbf{2-16}$$

Where $< r^2(t) >$ is the ensemble average of the MSD. Figure 2-2 shows that the self-diffusion coefficient can be derived from MSD versus time curves. At short times the non-linear part of the graph is associated with the so-called ballistic regime that occurs before particles experience collision. The self-diffusion coefficient measures the linear growth of MSD and can be derived from the slope of the MSD versus time curves at long times and equilibrium.

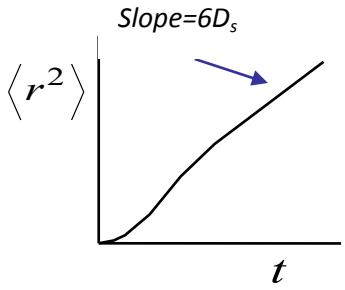

Figure 2-2: Plot of time vs. square of travelled distance

2.2.5 Periodic boundary conditions

Molecular simulations are run to predict and study the macroscopic properties of real systems. Therefore, it is desired to treat the system in a way that molecules experience forces as if they were in a bulk environment rather than simulating a small number of molecules in an isolated simulation cell with a few nanometres of length. Periodic boundary conditions (PBC) enable this by replicating the simulation cell throughout the phase space to form an infinite lattice. This means that any

molecule in the primary simulation cell can interact not only with molecules in its own cell, but also with those positioned in neighbouring cells as long as they are within the interaction cut-off distance. One condition that is combined with the PBC idea is the "minimum image convention". This condition states the simulation cell must be at least twice as large as the cut-off distance which ensures that each particle only interacts with its nearest neighbour image. Figure 2-3 illustrates the concept of periodic boundary condition in a two-dimensional system with the primary unit cell surrounded by another eight image cells. The implementation of periodic boundary conditions avoids finite size effects and reduces the computation costs considerably.

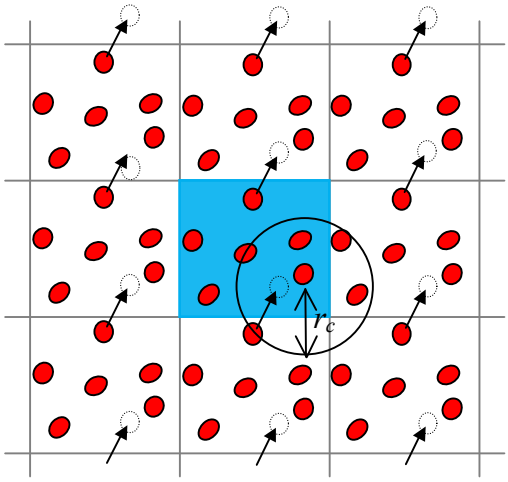

Figure 2-3: Schematic showing periodic boundary condition for a two dimensional system. The primary simulation cell is coloured in blue which is surrounded by 8 of its images. When a particle leaves a simulation box, it appears from the opposite side of the box. The "minimum image convention" concept is shown with the circle. Each particle only interacts with its nearest neighbour image within the cut-off radius (r_c).

2.2.6 Potentials

In order to perform molecular simulations to measure adsorptive or diffusive properties of various adsorbates in MOFs, force fields defining interactions between the adsorbate and the framework and the adsorbate molecules themselves are required. For this purpose, general-purpose force fields such as the universal force field (UFF) (Rappe *et al.* (1992)), the DREIDING force field (Mayo *et al.* (1990)) and OPLS (Jorgensen (1986)) are normally used to represent the interactions between the MOFs and adsorbates. In the literature, there are also reports where

force field parameters are refined to match simulation predictions with experimental measurements. These calculations should be considered with caution though, as the accuracy of experimental data is affected by defects of the synthesised MOFs and incomplete activation of samples (Liu *et al.* (2007), Keskin and Sholl (2009)). Quantum mechanical calculations are also used to provide more accurate potential parameters (i.e. Wang (2012), Tafipolsky *et al.* (2010)).

Some MOFs are relatively rigid and some exhibit framework flexibility. None of the MOFs considered in this thesis exhibit extreme modes of flexibility such as breathing (Serre *et al.* (2002), Ramsahye *et al.* (2007)) or gate opening (Nijem *et al.* (2012)) but can be considered as rigid with limited flexibility such as rotational flexibility of the linkers. Some computational studies in the literature show that such lattice dynamics have a considerable effect on the diffusion of guest molecules in MOFs (Amirjalayer *et al.* (2007)). Nevertheless, in many cases, good agreement between simulation and experimental adsorption results were obtained when the framework is considered as rigid (Düren *et al.* (2009), Keskin *et al.* (2009)). In other studies the effects of framework flexibility on adsorption were found to be nominal unless for the structures with breathing or gating effects (Greathouse *et al.* (2009), Ford *et al.* (2009)). In this work as in most simulation studies, MOFs are considered rigid frameworks hence only the interactions between the adsorbate and framework atoms are taken into account. This assumption also reduces significantly the computation time as the inclusion of framework flexibility becomes computationally expensive.

The force field parameters are typically divided into bonded and non-bonded interactions. Bonded interactions include bond stretching, bond bending and torsion. Non-bonded interactions include pairwise potentials of van der Waals attraction and repulsion, and Coulombic interactions (Figure 2-4). The total energy of a system is calculated by:

$$\Phi_{total} = \sum_{pairs} \Phi_{LJ} + \sum_{pairs} \Phi_{coul} + \sum_{bonds} \Phi_{bond} + \sum_{angles} \Phi_{angles} + \sum_{torsions} \Phi_{torsion} \qquad \textbf{2-17}$$

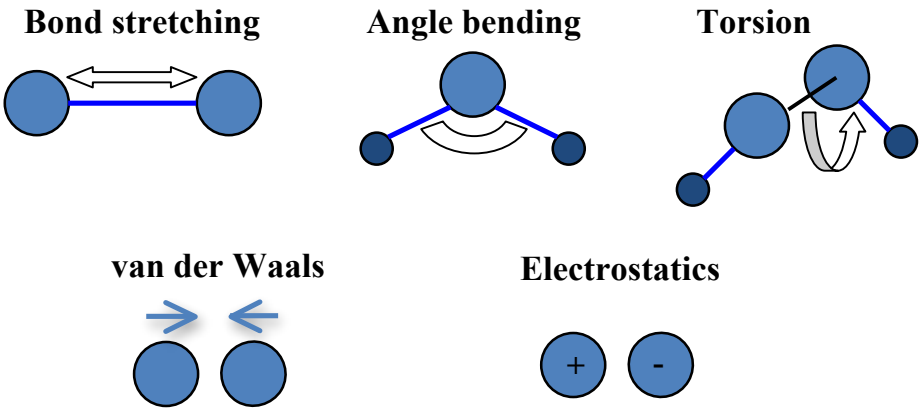

Figure 2-4: Illustration of bonded and non-bonded interactions in a force field.

2.2.6.1 Non-Bonded potentials

One of the most widely used pair potentials for describing van der Waals interactions is the Lennard-Jones (LJ) potential.

$$U(r_{ij}) = 4\varepsilon_{ij}\left[\left(\frac{\sigma_{ij}}{r_{ij}}\right)^{12} - \left(\frac{\sigma_{ij}}{r_{ij}}\right)^{6}\right] \qquad 2\text{-}18$$

where $U(r_{ij})$ is the intermolecular energy, r_{ij} is the distance between molecules i and j, ε_{ij} is the depth of potential well and σ_{ij} is the hard sphere diameter. In this thesis, the adsorbate molecules are represented by explicit and also united atom interaction sites. In the united-atom model, for example methane molecules or methyl groups in xylenes are modelled as one LJ site. The models and interaction sites for each adsorbate is described in the simulation section of each chapter. LJ parameters for mixed interactions are obtained from the Lorentz-Berthelot mixing rules:

$$\sigma_{ij} = 0.5(\sigma_i + \sigma_j) \qquad \textbf{2-19}$$

$$\varepsilon_{ij} = \sqrt{\varepsilon_i \varepsilon_j} \qquad \textbf{2-20}$$

In molecular simulation, the contribution of distant atoms can be neglected as the potential approaches zero very quickly for larger separation distances. Therefore, a

cut-off radius is defined and pair interactions beyond the cut-off are neglected for computational efficiency.

The long-ranged electrostatic interactions of species are represented by point charges. Using the Ewald summation technique (Frenkel and Smit (2002)), the intermolecular electrostatic interaction for a system containing point charges is modelled using Coulomb's law:

$$U_{Coul} = \sum_{i=1}^{N} \sum_{j=i+1}^{N} \frac{q_i q_j}{4\pi\varepsilon_0 r_{ij}} \qquad \textbf{2-21}$$

Where ε_0 is the permittivity in vacuum, q_i and q_j are the charges on atoms i and j, respectively, and r_{ij} is the interatomic distance between atoms i and j. In this work, the values for the point charges in MOFs are obtained from a first principles calculation method called density functional theory (DFT) (Sholl and Steckel (2009)) either from literature or calculated directly using Gaussian 09 package (Frisch *et al.* (2009)).

2.2.6.2 Bonded interactions

For flexible molecules, one has to account for coupling between stretching and bending in adjacent bonds along with torsional potential between different molecular planes (three consecutive bond vectors). The bonded interactions used in this thesis are taken from the OPLS-AA force field (Jorgensen *et al.* (1996)). The contributions of bonded interactions are calculated using the following equations:

Bond stretching: The bond stretching potential describes the change in energy as the bond stretches and contracts. It can be described with the harmonic potential according to Hook's law:

$$U_{stretch} = \frac{1}{2} K_{stretch} (r - r_{eq})^2 \qquad \textbf{2-22}$$

where $K_{stretch}$ is the bond force constant controlling the stiffness of the bond spring, r_{eq} is the equilibrium (reference) bond length and r is the distance between the two bonded atoms. It has been shown that replacing stretching potential with fixed bond lengths have no significant effect in Monte Carlo simulations (Chen *et al.* (2001)).

Bending potential: A harmonic potential is also used to describe bond bending in the angle formed by bonded triplet of atoms (θ). The energy associated with bending around the equilibrium bond angle (θ_{eq}), U_{bend} is given by:

$$U_{bend} = \frac{1}{2} K_{bend} (\theta - \theta_{eq})^2 \qquad \textbf{2-23}$$

where K_{bend} is the bending force constant.

Torsion potential: Torsion energy, $U_{torsion}$, is calculated from a periodic function that describes the out-of-plane angles of four atoms (The middle bond of three bonds formed by four atoms).

$$U_{torsion} = K_1 + \frac{K_2}{2}(1 + \cos\phi) + \frac{K_3}{2}(1 - \cos 2\phi) + \frac{K_4}{2}(1 + \cos 3\phi) \qquad \textbf{2-24}$$

where K_i are the dihedral force constants and ϕ is the dihedral angle.

Using the models and simulation techniques discussed in this chapter, in the remainder of this thesis the underlying adsorption and separation mechanisms of different mixtures in MOFs are studied. In the next chapter the separation of methane and hydrogen in calix[4]arenes and MOFs with calix[4]arene-based linkers is investigated.

Chapter 3 Calix[4]arene-based MOFs

In this Chapter, MOFs with *tert*-butylcalix[4]arene-based (TBC4) ligands and two levels of porosity associated with both the ligand and the structural framework are studied. As part of the collaboration with the groups of Andrew Burrows, materials chemistry, and Sean Bew, organic chemistry, laboratory synthesis of the MOFs and their linkers were carried out at the Universities of Bath and East Anglia, respectively. Here, firstly, TBC4 and its incorporation in MOFs as linkers is introduced. In Section 3.2, details of the molecular dynamics and GCMC models are given. Section 3.3 reports simulation results of dynamic properties and adsorption of methane and hydrogen in TBC4 itself. Section 3.4 deals with the synthesis of calix-based linkers by functionalising the upper- and lower-rims of TBC4 prepared at the University of East Anglia. Section 3.5 focuses on characterisation as well as molecular simulation studies of the prepared MOFs with the synthesised calix-based linkers. Finally, the conclusions are given in Section 3.6.

3.1 Introduction

As discussed in chapter 2, MOFs are built from metal clusters and organic linkers. The linkers of a MOF cannot only act for example as a catalytically active centre (Farrusseng *et al.* (2009), Isaeva and Kustov (2010)) but also provide extra adsorption sites for example by using structures from the calix[4]arene family (Figure 3-1).

Figure 3-1: Schematic figure of metal-organic frameworks with metal clusters and linkers. The structure of calix[4]arene which is a potential linker is shown on the right.

The cavity between the upper- and lower-rims in calix[4]arenes can host a variety of molecules and can be functionalised to be selective towards specific molecules for various applications such as gas separation and storage ((Atwood *et al.* (2005);

Thallapally *et al.* (2005), Enright *et al.* (2003), Thallapally *et al.* (2007)). Organic linkers based on *tert*-butylcalix[4]arene (TBC4) are attractive MOF linkers as they offer additional adsorption sites in the linker itself. The TBC4 molecule is a cup-shaped (Figure 3-2a) cyclic polyphenol and is composed of four phenyl rings connected by methylene linkers as shown in Figure 3-2a. Depending on the crystal phase, the structure may be open or filled with the *tert*-butyl moiety from the opposite layer (Ripmeester *et al.* (2006)). In this work, only the low density open form is studied. This conformation creates ABCD repeating layers along the *z* axis of the unit cell (Alavi *et al.* (2006), Alavi and Ripmeester (2008)) (Figure 3-2b).

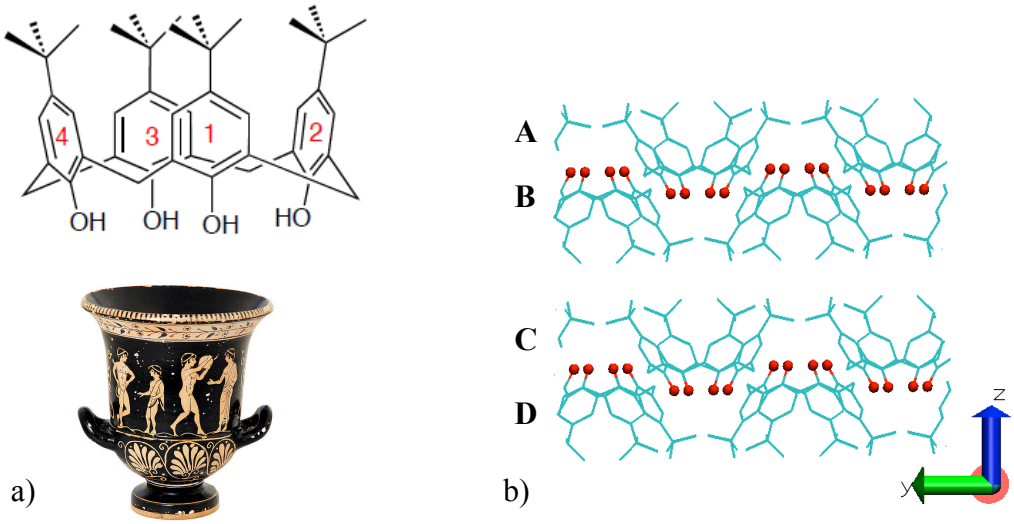

Figure 3-2: a) Cup-shape structure of tert-butylcalix[4]arene (TBC4). b) The structure of TBC4 in its open low density phase consisting of ABCD rows. The red spheres represent oxygen atoms. Hydrogen atoms are not shown for clarity.

Calixarene-based frameworks have been the subject of some reports in the literature because of their unique structure. For example, coordination networks have been prepared by *p*-sulfonated functionalisation of the upper-rims of calix[4]arenes (Dalgarno *et al.* (2004)) and calix[6]arenes (Dalgarno *et al.* (2004), Liu *et al.* (2009)). Similarly, structures with lower-rim modifications containing pyridine groups (Olguin *et al.* (2009)) and calixarene analogues with sulphur-bridged aryl groups (Chen *et al.* (2009)) have been also reported. Other functionalised calix[4]arenes such as *p*-octanoyl-calix[4]arenes have also been synthesised and tested for their gas sorption properties (Ananchenko *et al.* (2008)). Carboxylates are one of the most

commonly used groups in constructing MOFs, however there are very few reports of metal coordinated frameworks with calix[4]arene-based polycarboxylates. The study carried out by Kennedy *et al.* (2010) showed that dimeric upper-rim p-carboxylatocalix[4]arenes self-assemble into infinite hydrogen-bonded nanotubes, whereas *p*-carboxylatocalix[4]arenes-*O*-methyl ethers generate nanocapsules.

In this work, it is demonstrated how the upper- and lower-rim of TBC4 can be functionalised to form the 1,3-dicarboxylic acid H_2caldc (Figure 3-3). The free carboxylic acids were chosen to connect ligands to the metal building blocks in the MOF synthesis. The functionalisation of TBC4 was carried out by me in the organic chemistry lab at the University of East Anglia. The synthesised H_2caldc were then used to prepare MOFs containing copper, cobalt and cadmium at the University of Bath.

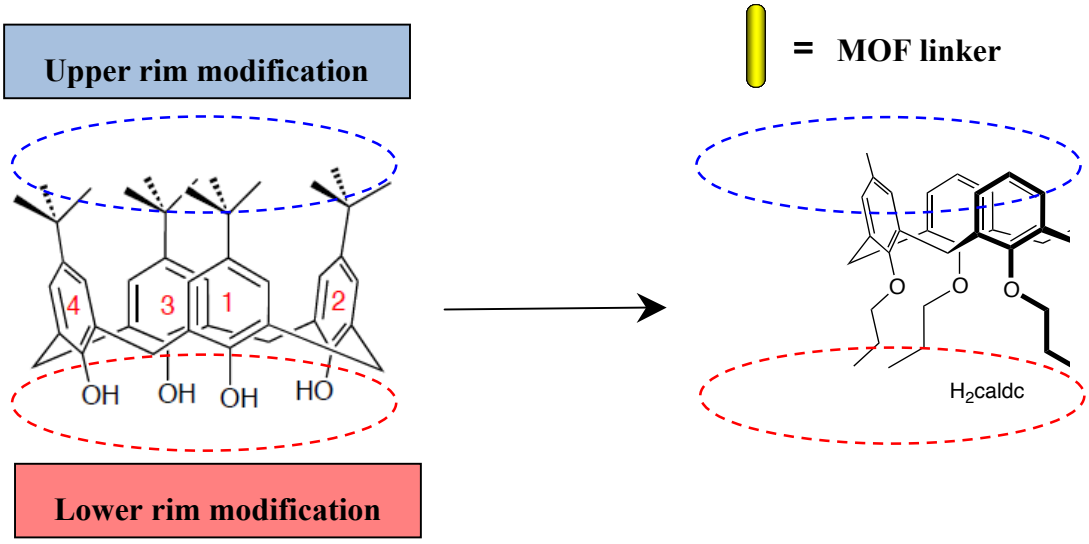

Figure 3-3: Modification of upper and lower rim of *tert*-butylcalix[4]arene (left structure) to synthesise H_2caldc (right structure) which can be used as a MOF linker.

As both TBC4 and the calix-based MOF can act as hosts for small molecules, the adsorptive/separative and dynamical properties of hydrogen and methane are studied in both. Growing demand for hydrogen in various fields such as fuel cells and petrochemical industries has lead to finding innovative strategies for hydrogen separation and purification. Hydrogen purification is commonly carried out by steam

reforming of methane (Herm *et al.* (2012)). An energy-efficient method to separate CH_4/H_2 is to use adsorptive separation in a packed bed of porous materials. Unlike other impurities in H_2 stream (i.e. CO, CO_2) methane has no permanent dipole or quadrupole moment and is difficult to remove due to its weaker interactions with the adsorbent. CH_4/H_2 separation is also important in refinery off gas processing where equimolar CH_4/H_2 mixture is separated between 5-10 bar (Wu *et al.* (2012)). In this chapter, after introducing the simulation details in section 3.2, first the simulation results for TBC4 will be presented followed by a description of the synthesis of the calix-based MOFs and the simulation results in these structures.

3.2 Simulation details

Molecular simulations of methane and hydrogen in calixarenes and calixarene-based MOFs were computed using molecular dynamics (MD) and GCMC simulations implemented in the RASPA simulation package (Dubbeldam *et al.* (2008)). Self-diffusion was studied using equilibrium MD in the NVT ensemble using the Nosé-Hoover thermostat. The equations of motion were integrated with a time step of 0.5 fs using the velocity-Verlet algorithm (Frenkel and Smit (2002)). For the calculation of both the guest-guest and the guest-framework interactions, the Lennard-Jones (LJ) potential was used with a cut-off radius of 12.8 Å. The LJ parameters for the frameworks were taken from the Dreiding force field (Mayo *et al.* (1990)) except for metal atoms which were taken from UFF force field (Rappe *et al.* (1992)). The potential parameters for methane were taken from Goodbody *et al.* (1991). In this model, the methane molecule is modelled as a single sphere. Hydrogen was modelled as a two site LJ molecule (Yang and Zhong (2006)). The Lorenz-Berthelot mixing rules were used to calculate mixed LJ parameters. The LJ potential parameters used in this work are listed in Table 3-1.

Table 3-1: Lennard-Jones parameters.

Species	Site	σ (Å)	ε k_B^{-1} (K)	Reference
MOF	Cu	3.11	2.56	Rappe *et al.* (1992)
	Co	2.55	7.04	Rappe *et al.* (1992)
	Cd	2.53	114	Rappe *et al.* (1992)
	O	3.03	48.19	Mayo *et al.* (1990)
	C	3.47	47.86	Mayo *et al.* (1990)
	H	2.85	7.65	Mayo *et al.* (1990)
Methane	CH_4	3.73	148	Goodbody *et al.* (1991)
Hydrogen	H_2	2.72	10	Yang and Zhong (2005)

Adsorption isotherms were calculated using GCMC simulations where molecules are randomly inserted, deleted, and translated and in the case of non-spherical molecules such as hydrogen also rotated. For binary mixtures, identity swap moves were also used for faster equilibration times. For all pure component isotherms, 1×10^5 equilibration and 2×10^5 production cycles were used for each point whereas for mixtures as many as 3×10^5 cycles were used for each equilibration and production run. Here, a cycle is defined as one MC move per molecule. Each simulation cell consisted of eight (2×2×2) unit cells with 25.44×25.44×25.17 $Å^3$ dimensions to allow for good statistics. The unit cell parameters for the synthesised MOFs are shown in Table 3-2. All frameworks are considered as rigid and their atoms were kept fixed at their crystallographic positions. The input fugacities for the GCMC simulations, which are related to the chemical potential by an equation of state, were calculated from the Peng-Robinson equation of state. It is noteworthy to mention that at sufficiently low pressures (i.e. less than 1 bar), methane behaves like an ideal gas and fugacity and pressure are similar. At higher pressures the fugacity deviates from pressure to essentially account for the non-ideality of the system. All results are reported as absolute amount adsorbed.

3.3 Adsorption and diffusion in tert-butyl-calix[4]arene

3.3.1 GCMC simulations of adsorption in tert-butyl-calix[4]arene

To examine the adsorption properties of TCB4, GCMC simulations of pure component and mixtures were carried out for methane and hydrogen. Figure 3-4 compares pure component adsorption isotherms for methane and hydrogen at 300 K. The isotherm for methane shows that methane is adsorbed more strongly than hydrogen and reaches the saturation plateau of ~ 3 molec/uc at 200 bar. At ~ 0.5 bar, the simulation results agree well with the experiments carried out by Atwood *et al.* (2005) where each unit cell is occupied by two molecules of methane. The largest difference between the two isotherms occurs between 0.5 to 10 bar where the adsorption enthalpy of methane (25.3±0.4 kJ/mol) is much larger compare to hydrogen (9.7±0.1 kJ/mol) as the strongest adsorption sites are occupied at low pressures. In the case of the less strongly adsorbed component, hydrogen, the amount adsorbed is much smaller compare to methane and substantial pore filling occurs only at higher pressures.

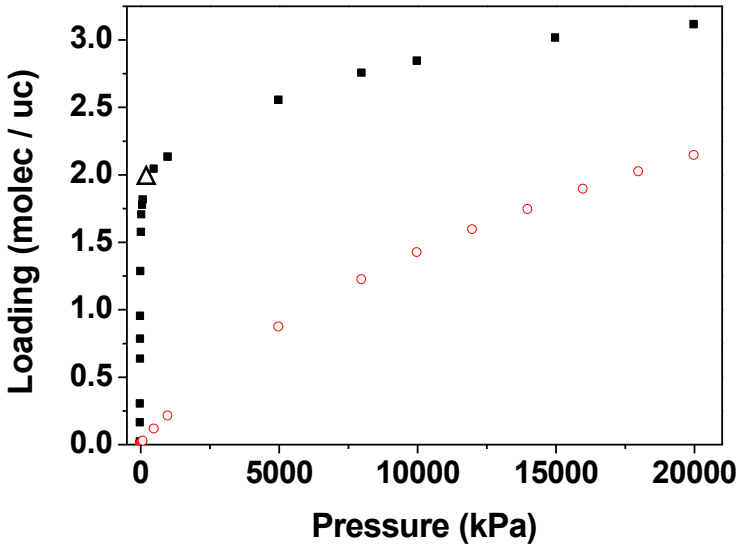

Figure 3-4: Single component isotherms for methane (closed squares) and hydrogen (open circles) at 300 K in TBC4. The experimental point is shown with the open triangle (Atwood *et al.* (2005)).

To obtain a visualisation of favourable adsorption sites, snapshots for both methane and hydrogen at 200 bar and 300 K are shown in Figure 3-5. The equilibrium adsorption sites in the cavities are the same for both molecules. The saturation loading of 3 molec/uc for methane corresponds to configurations where two molecules are adsorbed in the TBC4 cages in addition to another methane sitting in the interstitial site. However, in the case of the less strongly adsorbing hydrogen, the occupancy for these sites is lower by about 1 molec/uc.

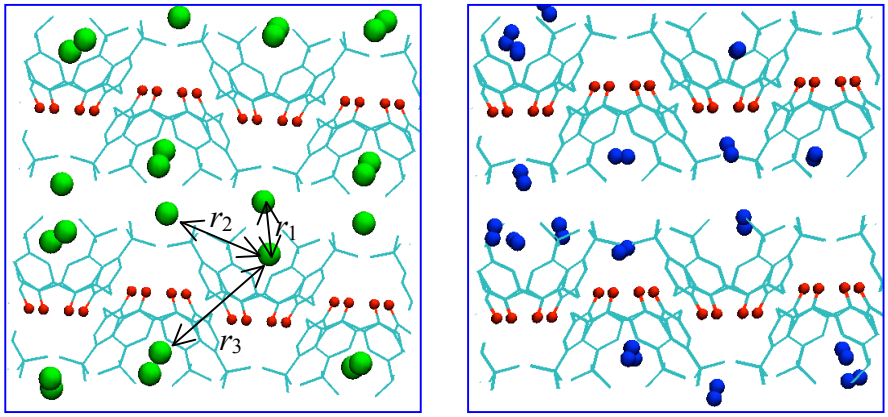

Figure 3-5: Snapshots of methane (green) and hydrogen (blue) adsorption in TBC4 at 200 bar and 300 K. Corresponding peaks in the RDF (Figure 3-6) are marked with r_1, r_2, r_3.

The distribution of adsorbates in TBC4 was also examined by calculating the radial distribution functions (RDF) for methane and hydrogen. The radial distribution function (RDF) or pair correlation function characterises how different atoms correlate with each other with increasing separation distance. As shown in Figure 3-6, RDF is a measure of probability of finding atoms in each shell dr (see red atoms) at a particular distance r from reference atom (blue atom) providing information about spatial distribution of atoms.

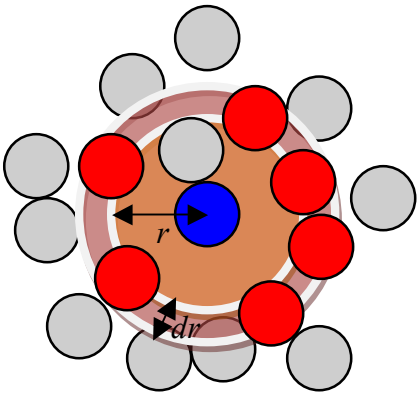

Figure 3-6: Evaluation of radial distribution function used to extract the structural information from simulations

The RDF results for methane-methane and hydrogen-hydrogen at 200 bar are plotted in Figure 3-7.

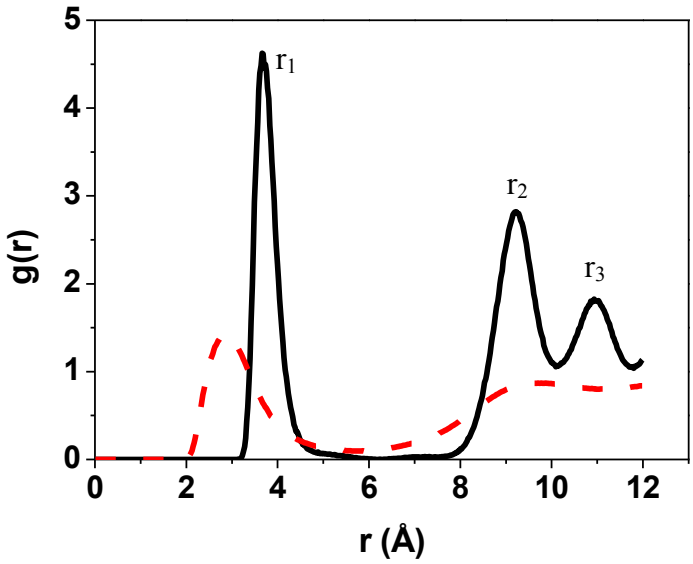

Figure 3-7: Radial distribution functions for the centre of mass CH_4-CH_4 (solid line) and H_2-H_2 (dashed line) at 200 bar and 300 K.

The first peak for methane lies in the repulsive region of the LJ methane-methane interaction potential around 3.7 Å and corresponds to the TBC4 cage and interstitial adsorption sites as marked with r_1 in Figure 3-5. This means that up to 2 methane molecules per cage can interact with each other. The two other long-range peaks correspond to the separation of methane molecules in the next nearest neighbours in adjacent TBC4 cages as shown by r_2 and r_3. Similar adsorption sites were observed for hydrogen although the peaks are broader indication that the hydrogen molecules

are less localised than the methane molecules. The first peak describing the separation of two hydrogen molecules in the cage of the TBC4 cage occurs at ~ 2.8 Å due to the smaller size of the hydrogen atoms.

Competitive adsorption simulations were also performed for mixtures of methane and hydrogen at 300 K. In accordance with the trend seen in pure component results, equimolar mixture simulations also show that only methane adsorbs preferentially up to 5-10 bar due to its better size match with calix bowls. Hydrogen only adsorbs at higher pressures with average methane selectivity values of ~37.0 in a range of 10 to 180 bar.

3.3.2 Molecular dynamics simulations of methane and hydrogen in tert-butyl-calix[4]arene

Molecular dynamics is a powerful tool to follow the evolution of molecules interacting through intermolecular forces and it has been used to study various guest-host properties such as diffusivity, sites of interaction and spatial information (Rodríguez-Ropero *et al.* (2008), Alavi *et al.* (2010)). Alavi and Ripmeester (2008) compared multiple calix occupancies of a number of adsorbates and found higher guest inclusion energies for xenon > carbon dioxide > methane > hydrogen. In other studies carried out by Alavi *et al.* (2006) and Daschbach *et al.* (2009), the structural properties for a number of guest molecules and carbon dioxide inside TBC4 were investigated using molecular dynamics simulations where no guest-guest interactions were found at loadings below 2 molecule per unit cell of TBC4. To get a better understanding of the guest-host behaviour in our synthesised calix-based MOFs discussed in section 3.5, in this work, a similar but more detailed molecular dynamics simulation study is carried out for two different loadings of 2 and 4 molec/uc for hydrogen and methane. As each unit cell consists of two TBC4 cages, these loadings correspond to 1 and 2 molecules per TBC4 cage respectively. The occupancy probability of hydrogen and methane measured for the centre of mass at the two loadings is depicted in Figure 3-8. As it can be seen, at the loading of 2 molec/uc the favourable locations are positioned inside the TCB4 cages and the

area between opposite neighbours of butyl tails becomes more accessible at 4 molec/uc loading for both molecules. The density distribution figure for hydrogen shows that hydrogen molecules are more mobile and are exchanged between the two sites especially at 4 molec/uc. This was also observed by the visualisation of trajectories. In contrast to hydrogen, methane sits tightly inside the cages without any significant movement. This is consistent with the RDF results obtained from the GCMC simulations where sharper peaks were observed for methane molecules.

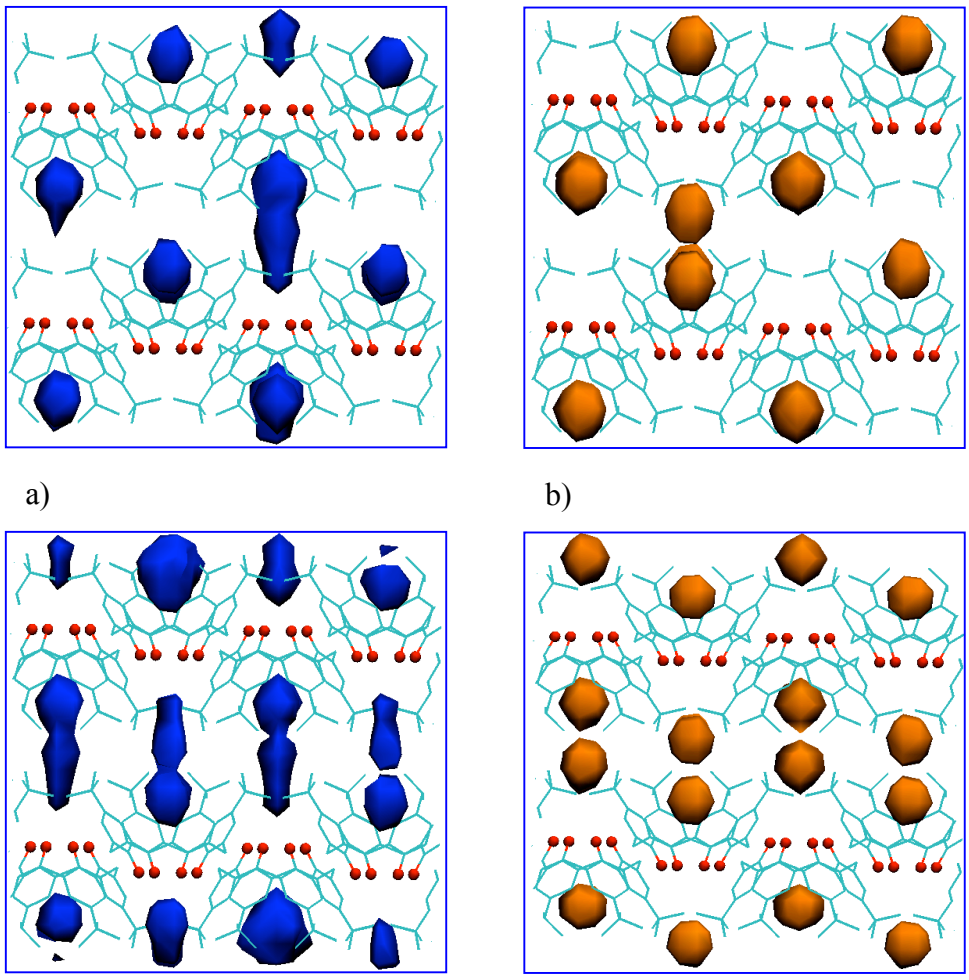

Figure 3-8: Probability density distribution of a) hydrogen (blue) and b) methane (orange) in TBC4 at 300 K and loadings of 2 molec/uc (top) and 4 molec/uc (bottom). Each unit cell consists of two TBC4 cages. Hydrogen atoms of the framework are not shown for clarity.

In order to investigate the underlying nature of the dynamical motion of methane and hydrogen in calix cages, the mean square displacement (MSD) and velocity autocorrelation function (VACF) were determined at the loading of 2 molec/uc. As mentioned in chapter 2, the MSD is computed from the positions of a molecule averaged over all configurations and the slope of the MSD over time yields the self-diffusion coefficient. The VACF is normally calculated for the analysis of vibrational or diffusive motion of molecules and it relates the velocity of a particle at a certain time to the velocity of the same particle at a later time during the course of simulation. If the velocity vector of a molecule is $v(t)$, then the VACF, $Z_v(t)$ can be written as:

$$Z_v(t) = \frac{\langle v(0) \cdot v(t) \rangle}{\langle v(0) \cdot v(0) \rangle} \qquad \textbf{3-1}$$

where, $v(t)$ is the velocity of the centre of mass of the molecule. As shown in Figure 3-9, methane and hydrogen tend to form an oscillatory pattern in both the MSD and VACF curves. Normally, by assuming that the molecules move according to a random walk, it is shown that for long times, the MSD changes linearly with time according to Einstein relation (chapter 2, equation 2.16). In this system, the small-amplitude fluctuations of both MSD and VACF curves are indicative of the fact that molecules are confined to the TBC4 cages and they do not show diffusive motion. The results from the VACF curves show that the velocity of the molecules is self-correlating in a periodic fashion caused by the calix[4]arene walls. The periods of MSD and VACF motions are smaller for methane molecules than the ones observed for hydrogen. Similar periodic motion to methane was also observed for xenon and nitrogen guest molecules at the same loading (Alavi *et al.* (2006)). This suggests that hydrogen molecules are more mobile in the calix framework. This was expected because methane is larger and interacts more strongly with the calix cages in comparison to the smaller hydrogen molecules that are able to move and rotate more freely.

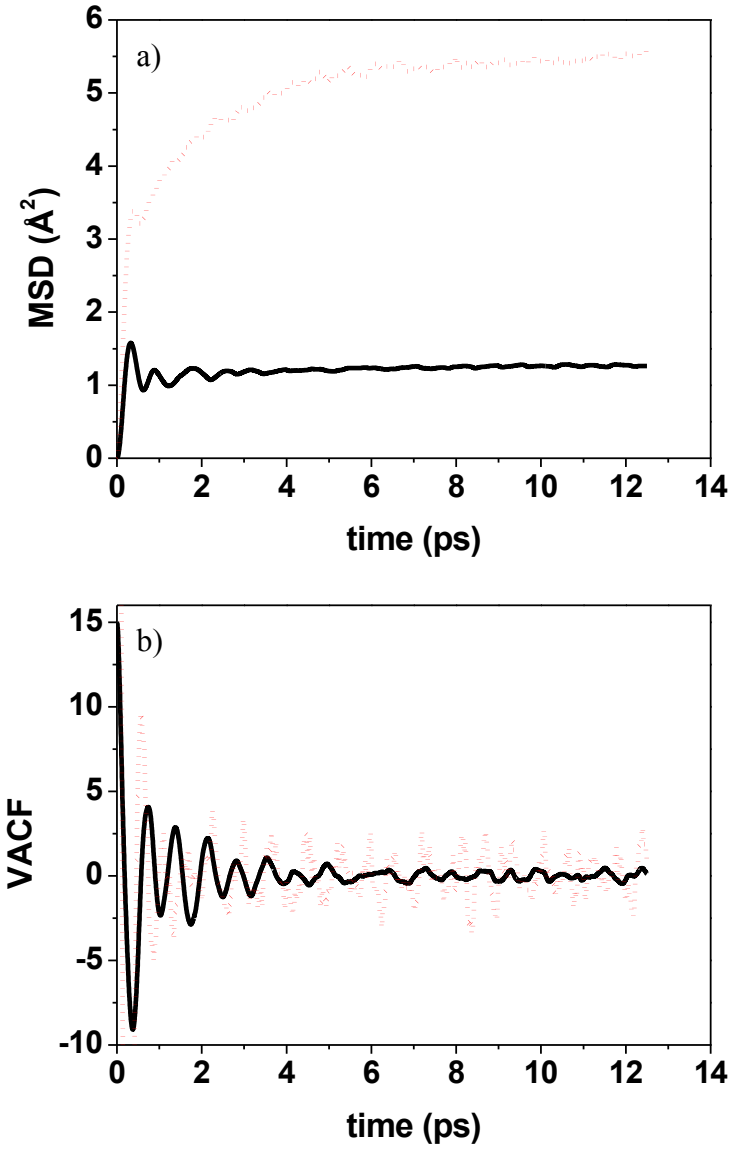

Figure 3-9: a) Mean square displacement (MSD) and b) Velocity autocorrelation function (VACF) for methane (solid line) and hydrogen (dotted line) for the loading of 2 molec/uc.

In accordance with the previous results suggesting a tighter fit for the methane molecules, the analysis of the guest-framework interactions shows stronger affinity for methane compared to hydrogen. At the loading of 2 molec/uc, the average methane potential energy is -23.6 ± 0.1 kJ/mol, whereas in the case of hydrogen this value is much lower at around -6.4 ± 0.09 kJ/mol. It is also observed that the interaction between both methane-methane and hydrogen-hydrogen is negligible at this loading due to the large separation between them. At higher loadings of 2

molecules per cage of TBC4 (corresponding to 4 molec/uc), the guest-guest interaction energies become repulsive but are still very low compare to guest-framework energies.

The molecular dynamics and GCMC simulation results presented here along with other studies in the literature (Ripmeester *et al.* (2006)), suggest that TBC4 displays interesting adsorptive characteristics. These properties make these materials good candidates for adsorptive and separation purposes. This is why the idea of harnessing these properties in addition to the intrinsic characteristics of MOFs is very interesting. To achieve this goal, the synthesis of the organic linker based on TBC4 was carried out and is reported in the next section. The MOFs build from the synthesised linkers were then characterised and tested for their adsorption capabilities.

3.4 Synthesis of calix[4]arene-based linker

In order to synthesise the calix[4]arene based linker, *tert*-butylcalix[4]arene pre-synthesised at the University of East Anglia following the method reported by Gutsche (1998) was used (Figure 3-10). In order to incorporate the new linker into MOFs, it was necessary to functionalise the lower- and upper-rims of TBC4. In this section, the synthesis of the new linker based on the upper rim appended 1,3-dicarboxylate acid, 25,26,27,28-tetrapropoxycalix[4]arene-5,17-dicarboxylic acid (H_2caldc) is described step-by-step.

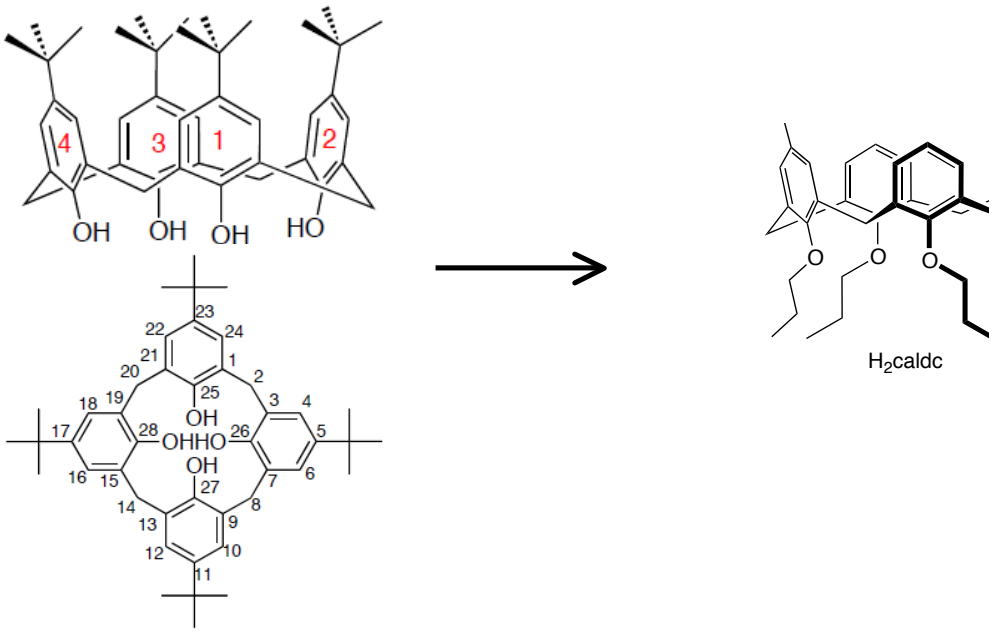

Figure 3-10: Schematic of the synthesis of 25,26,27,28-tetrapropoxycalix[4]arene-5,17-dicarboxylic acid (H_2caldc) (right) from 5,11,17,23-tetra-tert-butyl-25,26,27,28-hydroxycalix[4]arene (TBC4) (left).

The synthesis of H_2caldc from *tert*-butylcalix[4]arene was carried out in six steps at the organic chemistry lab at the University of East Anglia following a method developed by Dr. Sean Bew's group. At the end of each step, the structures were confirmed by proton nuclear magnetic NMR (HNMR) spectroscopy. HNMR is a powerful method used in the determination of structure of organic compounds. The HNMR spectrum of an organic compound provides information about the number of different types of hydrogens, relative number of different hydrogens and the electronic environment of the different types of hydrogens. The HNMRs were recorded on Oxford 300 MHz spectrometer machines and samples were prepared as solutions of $CDCL_3$. Chemical shifts are reported in parts per million (ppm) (δ). The coupling constant J_{HH} are given in Hz. Higher quality NMRs and Figure 3-11 are taken from Viorica Sebestyen from the University of Bath who was my lab partner during the synthesis of H_2caldc. A detailed schematic of the synthesis process is given in Figure 3-11.

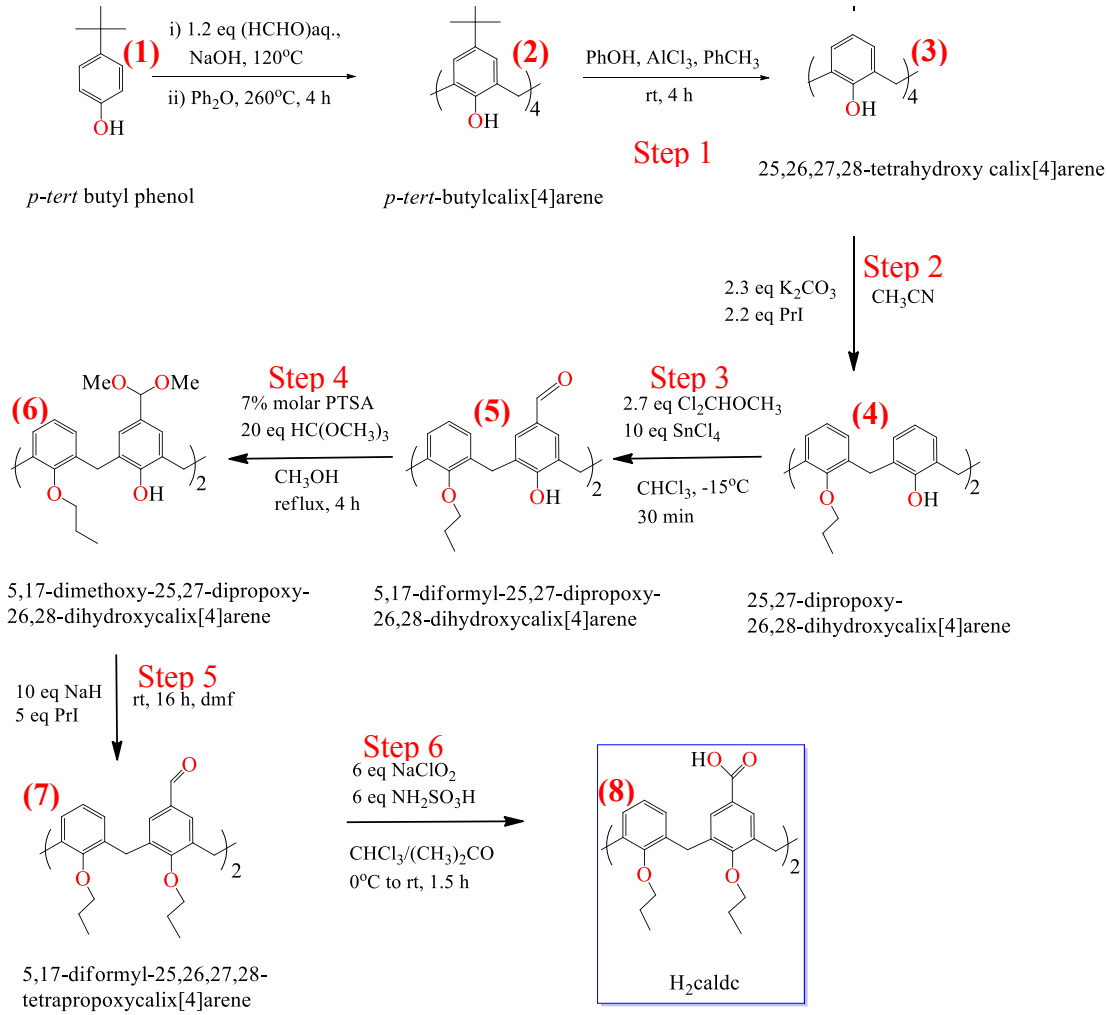

Figure 3-11: Synthesis of H_2caldc (25,26,27,28-tetrapropoxycalix[4]arene-5,17-dicarboxylic acid (8) from TBC4(2)).

Step 1: Synthesis of 25,26,27,28-tetrahydroxycalix[4]arene **(3)** (Removal of the *tert*-butyl moiety).

In order to functionalise *p-tert*-butylcalix[4]arenes **(2)** at the lower rim, it is necessary to remove the *tert*-butyl moiety from the component's upper rim, generating **(3)**. This was achieved by adding 50 mL of anhydrous toluene to a round-bottom flask charged with 12 g of *p-tert*-butyl-calix[4]arene under nitrogen at room temperature. Phenol (2.59 g) was added in one portion and the reaction mixture was stirred for 10 minutes. Phenol acts as an acceptor *tert*-butyl cation generated from the

reaction. Aluminium chloride (12 g) was slowly added to the mixture and further stirred for three hours before being poured onto crushed ice (100 g) to quench the reaction. Aluminium chloride is used as a Lewis acid, to remove the *tert*-butyl moiety from the calix[4]arene. The reaction flask was rinsed with ice followed by dichloromethane (50 mL). These washings were added to the mixture before being transferred to a 1 L separating funnel. The aqueous phase was further extracted with dichloromethane (100 mL) and the combined organic phases were washed successively with a 1 M aqueous solution of hydrochloric acid (3×200 mL) and water (2×200 mL). The solvent was then removed *in vacuo* to afford an orange solid. Diethyl ether was added to the solid with subsequent cooling to -15 ºC for one hour. The obtained precipitate was collected by vacuum suction filtration to give a bright white powder (6.07 g). Analysis of the NMR revealed the *tert*-butyl moiety was successfully removed and compound **(3)** was obtained (Figure 3-12). ^{1}H NMR (400MHz, $CDCl_3$): δ 10.16 (s, 4H, O*H*), 7.02 (d, 8H, *m*-HOAr*H*, *J* = 7.54 Hz), 6.70 (t, 4H, *p*-HOAr*H*, *J* = 7.54 Hz), 4.23 (broad, 4H, ArCHax*Heq*Ar, *J* = 13.6 Hz), 3.51 (broad, 4H, ArCHax*Heq*Ar, *J* = 13.6 Hz). As mentioned before, phenol acts as the acceptor of *tert*-butyl moiety and therefore, this reaction produces 2,4,6-*tert*-butylphenol as the by-product.

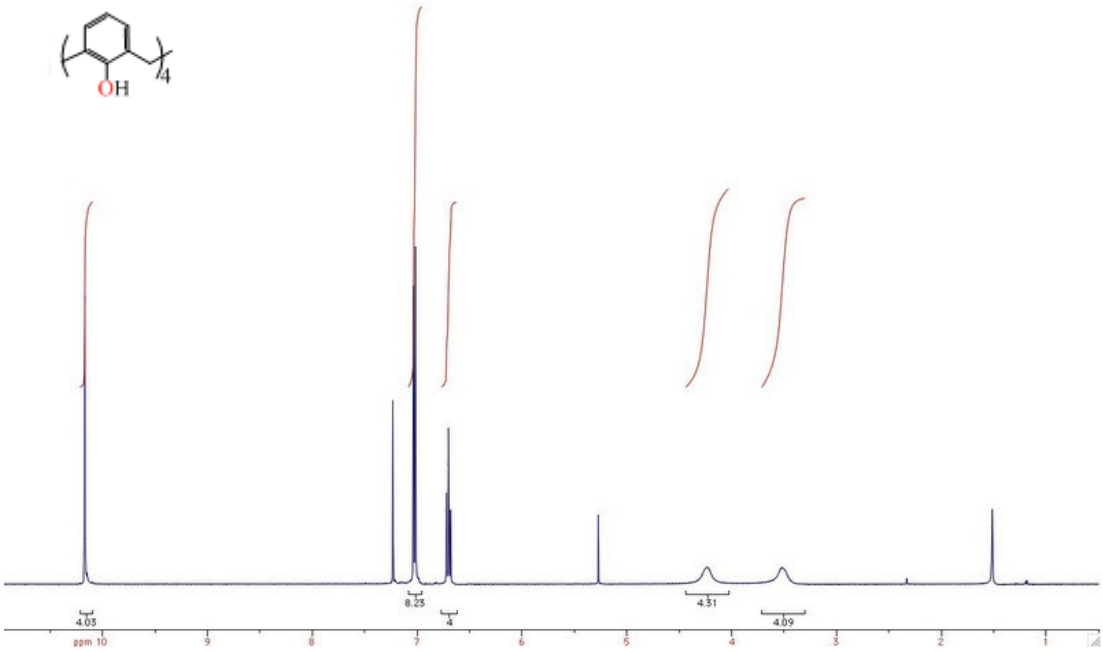

Figure 3-12: HNMR spectrum of 25, 26, 27, 28-tetrahydroxycalix[4]arene (3) in $CDCl_3$.

Step 2: Synthesis of 25,27-dipropoxy-26,28-dihydroxycalix[4]arene **(4).**

In order to functionalise calix[4]arene's upper-rim, it is necessary to first selectively protect the lower rim hydroxyl groups to deactivate the arene group. This was achieved by alkylating the opposing hydroxyl groups by 1-iodopropane. To do this, a 100 mL round-bottom flask was charged with a solution of **(3)** (4.31 g) in anhydrous acetonitrile (50 mL) at room temperature. In addition, 2.3 equivalent of potassium carbonate (3.20g) was used to selectively de-protonate opposing hydroxyl groups. 1-iodopropane (6.55 mL) was then added. The mixture was heated under reflux for 16 hours. The reaction mixture was then cooled to room temperature and the solvent was removed *in vacuo*. The solid was redissolved in dichloromethane (50 mL). The dichloromethane solution was washed with a 1 M hydrochloric acid (2×200 mL) followed by brine (50 mL) in a separating funnel. The organic layer was then filtered and concentrated *in vacuo* to give a white powder. HNMR confirmed the structure to be 25,27-dipropoxy-26,28-dihydroxycalix[4]arene **(4)** **(**Figure 3-13**)**. ^{1}H NMR (300MHz, $CDCl_3$): δ 8.22 (s, 2H, O*H*), 6.98 (d, 4H, *m*-HOAr*H*, *J* = 7.35 Hz), 6.85

(d, 4H, *m*-PrOAr*H*, *J* = 7.54 Hz), 6.67 (t, 2H, *p*-HOAr*H*, *J* = 7.35 Hz), 6.57 (t, 2H, *p*-PrOAr*H*, *J* = 7.54 Hz), 4.25 (4H, ArC*Hax*HeqAr, *J* = 14.00 Hz), 3.91 (t, 4H, ArOCH_2CH$_2$CH$_3$, *J* = 14.00 Hz), 3.29 (4H, ArCHax*Heq*Ar, *J* = 14.00 Hz), 2.061.95 (sextet, 4H, ArOCH$_2$CH_2CH$_3$, *J* = 14.00 Hz), 1.25 (t, 6H, ArOCH$_2$CH$_2$CH_3, 3*J* = 14.00 Hz).

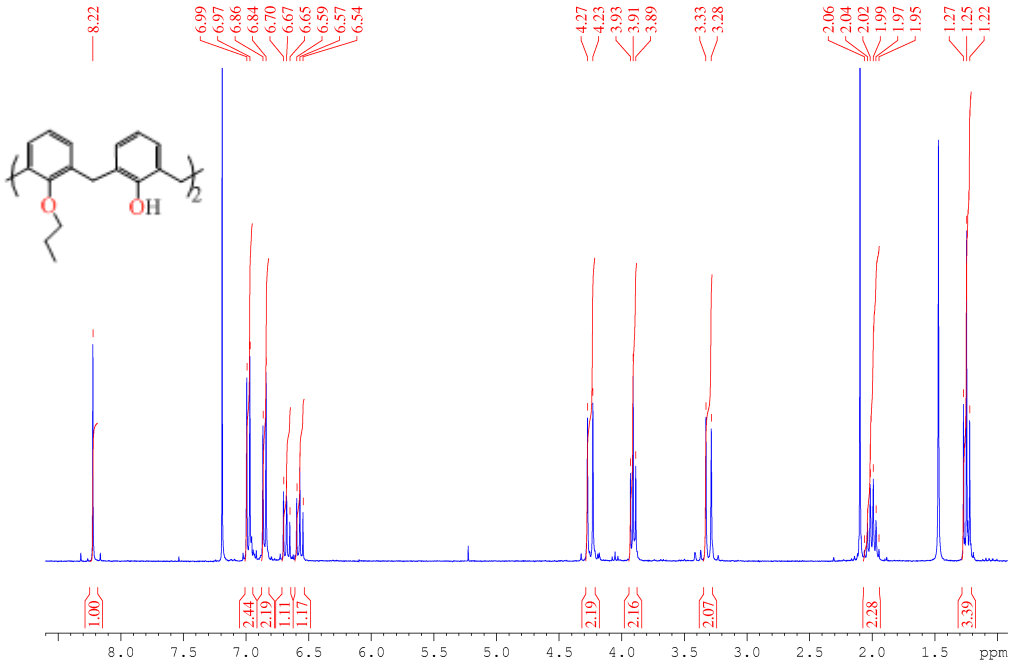

Figure 3-13: HNMR spectrum of 25,27-dipropoxy-26,28-dihydroxycalix[4]arene (4) in $CDCl_3$.

Step 3: Synthesis of 5,17-diformyl-25,27-dipropoxy-26,28-dihydroxycalix[4]arene **(5)**.

A 250 mL round-bottom flask charged with a solution of **(4)** (2.9 g) in anhydrous chloroform (75 mL) under an atmosphere of nitrogen was cooled to -20 °C. Tin (IV) chloride (6.7 mL) was added in one portion via syringe, followed by 1,1-dichloromethyl methyl ether (1.4 mL). The mixture was then stirred at -20 °C for 30 minutes. The solution was then allowed to reach room temperature and stirred for

another three hours. After the reaction was complete, it was quenched with water (40 mL). Following transferral to a separating funnel, the organic phase was washed with brine (2×40 mL). The product was dried over magnesium sulfate and filtered under vacuum. Purification of the residue with methanol gave a purple solid (3.0 g). HNMR analysis revealed the solid to be **(5)** (Figure 3-14). ^{1}H NMR (300MHz, $CDCl_3$): δ 9.72 (s, 2H, O*H*), 9.21 (s, 2H, C*H*O), 7.57 (s, 4H, *m*-HOAr*H*COH), 6.91 (d, 4H, *m*-PrOAr*H*, *J* = 7.56 Hz), 6.74 (t, 2H, *p*-PrOAr*H*, *J* = 7.56 Hz), 4.24 (d, 4H, ArC*Hax*HeqAr, *J* = 14.32 Hz), 3.95 (t, 4H, ArOCH_2CH$_2$CH$_3$, *J* = 14.32 Hz), 3.44 (d, 4H, ArCHax*Heq*Ar, *J* = 14.32 Hz), 2.081.96 (sextet, 4H, ArOCH$_2$CH_2CH$_3$, *J* = 14.32 Hz), 1.27 (t, 6H, ArOCH$_2$CH$_2$CH_3, *J* = 14.32 Hz).

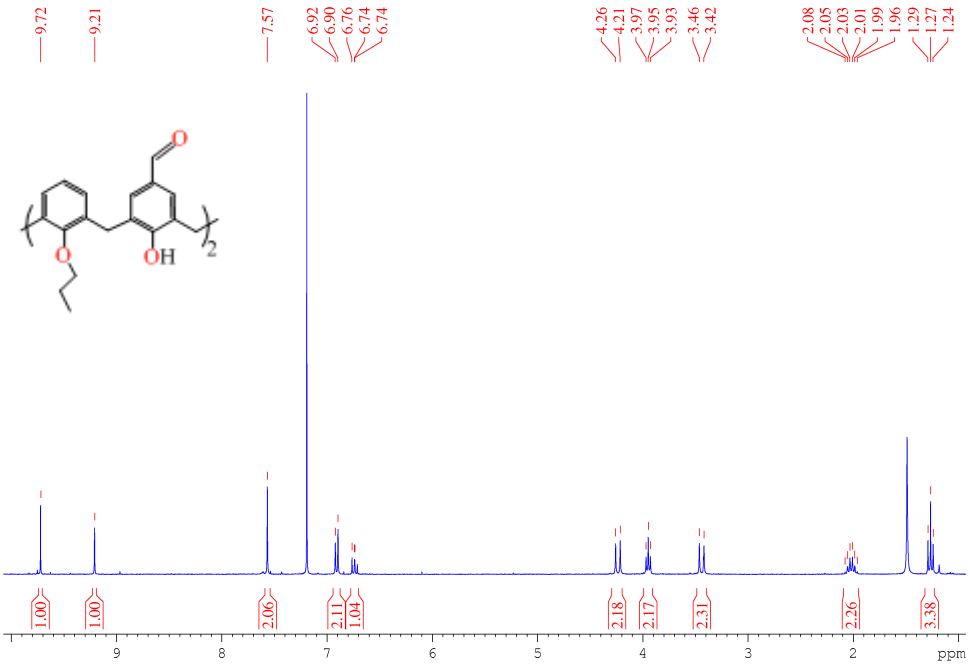

Figure 3-14: HNMR spectrum of 5,17-diformyl-25,27-dipropoxy-26,28-dihydroxycalix[4]arene (5) in $CDCl_3$.

Step 4: Synthesis of 5,17-dimethoxy-25,27-dipropoxy-26,28-dihydroxycalix[4]arene **(6).**

A 250 mL round-bottom flask charged with a solution of **(5)** (3.22 g) and methanol (80 mL) was stirred under an atmosphere of nitrogen. P-toluene sulfonic acid

(0.074 g) was added to the mixture and stirred for 5 minutes. Trimethyl orthoformate (12.5 mL) was added via syringe and the reaction mixture was heated under reflux overnight under stirring. The resulting mixture was then allowed to cool to room temperature. 40 mL of $NaHCO_3$ was then added to the mixture and stirred for 15 minutes. The solution was extracted with dichloromethane (3×30 mL) and washed with of water (2×30 mL) and brine (2×40 mL). Finally, the solvent was removed and the mixture was filtered *in vacuo* to afford a white powder (3.2 g). The powder was confirmed by HNMR to be the structure of **(6)**. ^{1}H NMR (250 MHz, $CDCl_3$): δ 8.36 (s, 2H, O*H*), 7.05 (s, 4H, m-HOAr*H*$(OCH_3)_2$), 6.88 (d, 4H, *m*-PrOAr*H*, *J* = 7.36 Hz), 6.68 (t, 2H, *p*-PrOAr*H*, *J* = 7.36 Hz), 5.21 (s, 2H, *p*-HOAr*H*$(OCH_3)_2$) 4.24 (d, 4H, ArC*Hax*HeqAr, *J* = 12.80 Hz), 3.90 (t, 4H, ArOC$H_2$$CH_2CH_3$, *J* = 11.20 Hz), 3.33 (d, 4H, ArCHax*Heq*Ar, *J* = 12.80 Hz), 2.071.93 (sextet, 4H, $ArOCH_2CH_2CH_3$, *J* = 11.20 Hz), 1.25 (t, 6H, $ArOCH_2CH_2CH_3$, *J* = 11.20 Hz).

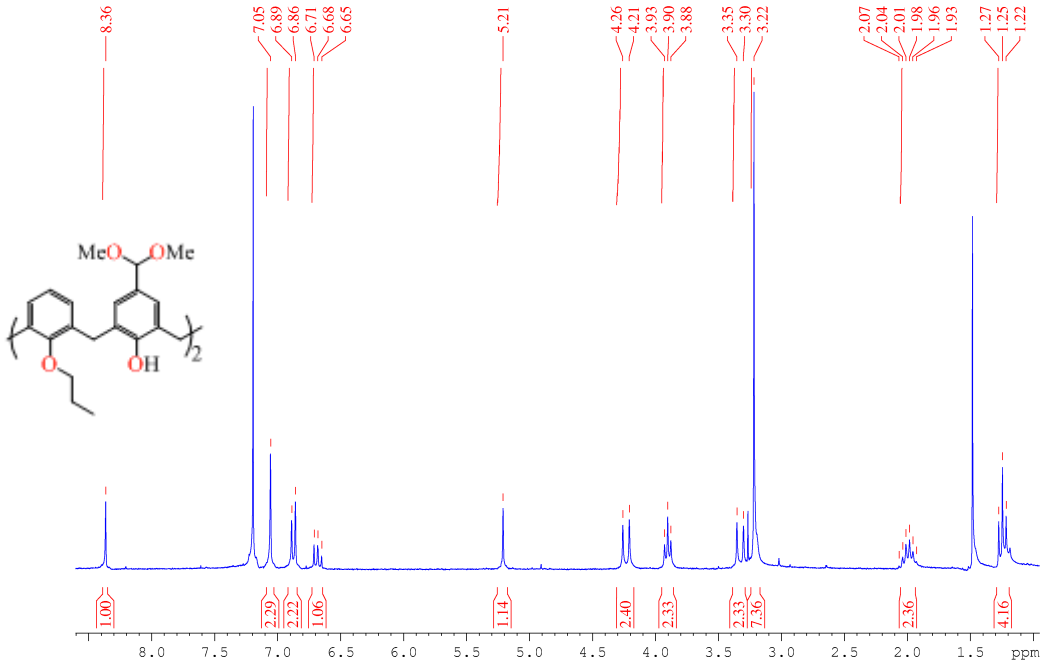

Figure 3-15: HNMR spectrum of 5,17-dimethoxy-25,27-dipropoxy-26,28-dihydroxycalix[4]arene (6) in $CDCl_3$.

Step 5: Synthesis of 5,17-diformyl-25,26,27,28-tetrapropoxycalix[4]arene **(7)**.

Sodium hydride (0.71 g) was washed with hexane (2×15 mL) in a round-bottom flask. Dimethylformamide (40 mL) was added to the solution and stirred for 20 minutes while cooling to 0 °C. **(6)** (1.95 g) is then added slowly over 10 minutes. The solution is stirred for another 30 minutes and let to warm to room temperature. n-propyl iodide (1.45 mL) is then added via syringe and the reaction mixture is further stirred overnight at room temperature. The solution is cooled again to 0 °C and quenched with 1M HCl (30 mL) (added very slowly and stirred for 30 minutes). The solution was then extracted with (3×40 mL) of dichloromethane and subsequently the organic phase was washed with 1M HCl (50 mL) and sodium thiosulphate (2×30 mL). The product was then washed with water (3×40 mL) and brine (2×40 mL) followed by drying with magnesium sulphate. The resulting solid was collected by suction filtration *in vacuo* to afford a pale yellow solid (1.5 g). HNMR revealed the structure to be the desired structure of **(7) (**Figure 3-16**)**. ^{1}H NMR (250 MHz, $CDCl_3$): δ 9.39 (s, 2H, C*H*O), 6.93 (s, 4H, *m*-Ar*H*CHO), 6.716.62 (m, 6H, *p*-Ar*H*), 4.40 (d, 4H, ArC*Hax*HeqAr, *J* = 13.6 Hz), 3.853.78 (m, 8H, ArOCH_2CH$_2$CH$_3$), 3.16 (d, 4H, ArCHax*Heq*Ar, *J* = 13.6 Hz), 1.921.77 (m, 8H, ArOCH$_2$CH_2CH$_3$), 0.990.87 (m, 12H, ArOCH$_2$CH$_2$CH_3).

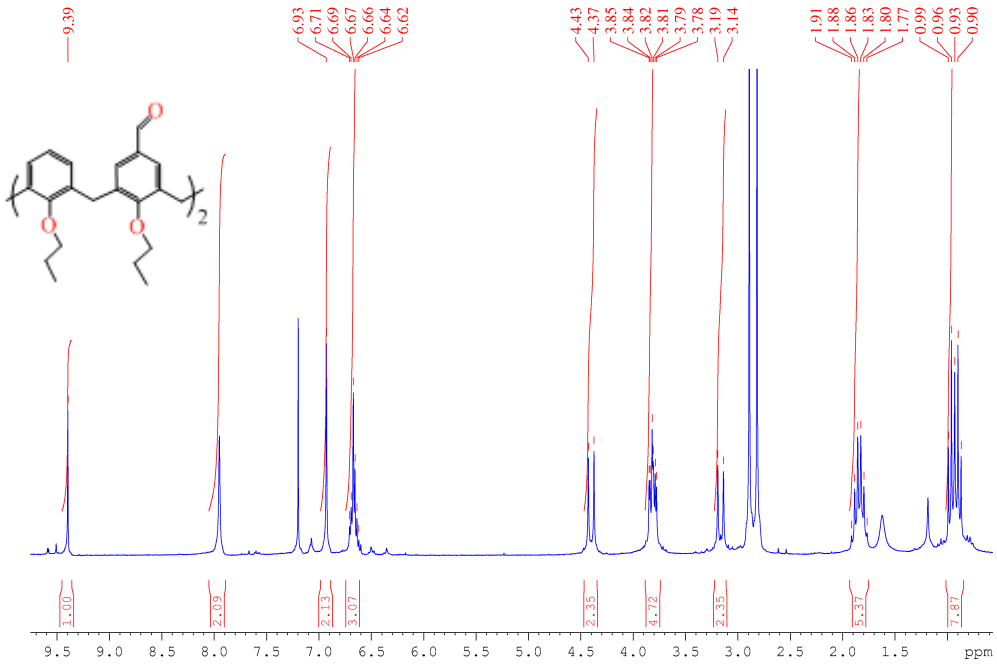

Figure 3-16: HNMR spectrum of 5,17-diformyl-25,26,27,28-tetrapropoxycalix[4]arene (7) in $CDCl_3$.

Step 6: Synthesis of 25,26,27,28-tetrapropoxycalix[4]arene-5,17-dicarboxylic acid (H_2caldc) **(8)**.

In the final step, a 250 mL round-bottom flask charged with a solution of **(7)** (0.623 g), acetone and chloroform (40 mL) was cooled to 0 °C and stirred for 30 minutes. Sulfamic acid (0.560 g) was added to the mixture and stirred for another 30 minutes. Sodium chlorite (0.522 g) dissolved in 2 mL of water was then added in one portion and the reaction mixture was warmed to room temperature. The organic phase was removed under reduced pressure. The resulting mixture was extracted from water and HCl with ethyl acetate (4×50 mL). The combined organics were then washed with water (3×40 mL) and brine (2×40 mL). The organic phase was dried over magnesium sulphate followed by filtration to afford a pale yellow powder. HNMR analysis revealed the solid to be the desired title compound **(8)** (Figure 3-17). ^{1}H NMR (250 MHz, $CDCl_3$): δ 12.89 (s, 2H, COO*H*), 7.11 (d, 4H, *m*-Ar*H*, *J* = 7.4 Hz),

6.96 (t, 2H, *p*-Ar*H*, *J* = 7.4 Hz), 6.69 (s, 4H, *m*-Ar*H*COOH), 4.35 (d, 4H, ArC*Hax*HeqAr, *J* = 13.6 Hz), 3.92 (t, 4H, ArOCH_2CH$_2$CH$_3$, *J* = 8.5 Hz), 3.59 (t, 4H, HOOCArOCH_2CH$_2$CH$_3$, *J* = 6.5 Hz), 3.08 (d, 4H, ArCHax*Heq*Ar, *J* = 13.6 Hz), 1.80 (m, 8H, ArOCH$_2$CH_2CH$_3$), 1.03 (t, 6H, ArOCH$_2$CH$_2$CH_3, *J* = 7.4 Hz), 0.79 (t, 6H, HOOCArOCH$_2$CH$_2$CH_3, *J* = 7.4 Hz).

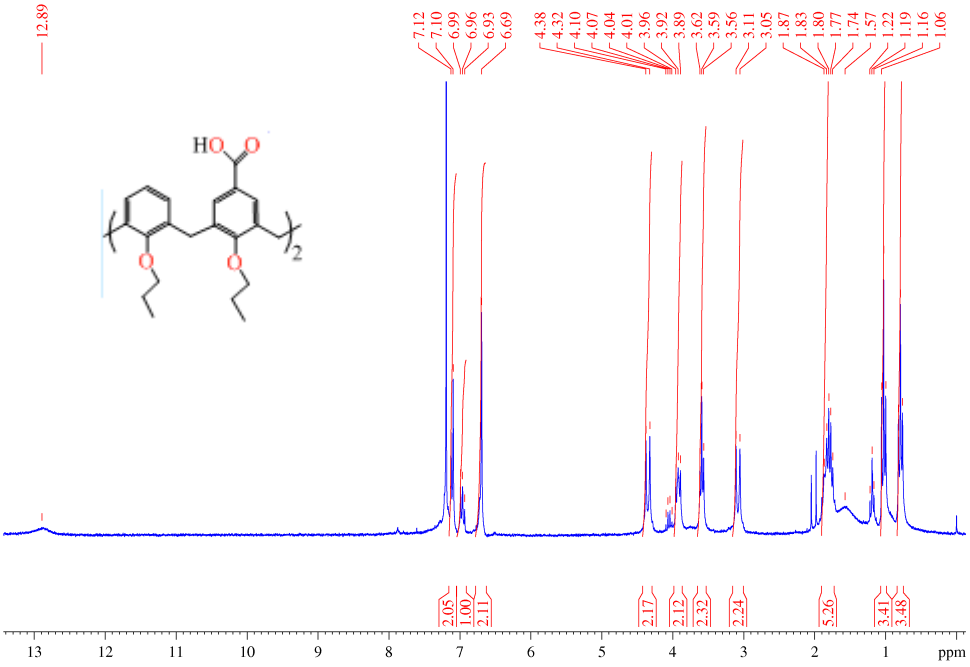

Figure 3-17: HNMR spectrum of 25,26,27,28-tetrapropoxycalix[4]arene-5,17-dicarboxylic acid (H_2caldc) (8) in $CDCl_3$.

3.5 MOFs with calixarene-based linkers

The synthesised linker, H_2caldc was used to prepare a number of MOFs at the University of Bath in the group of Dr. Andrew Burrows. The MOFs were prepared from the reaction of the metal (II) salts (Cu, Co and Cd) with H_2caldc in DMF under solvothermal conditions. It is worth mentioning that the small-scale production of the H_2caldc is due to the complexity of the reactions that makes it difficult and costly to scale up. Therefore, extended MOFs based on the synthesized linkers were also prepared in small scales. Details about the synthesis of the MOFs can be found in our

work (Bew *et al.* (2012)). The crystallographic information (CIF) files were used for further simulation studies in Edinburgh. In the remainder of this chapter, details of geometrical characterisation and building units of these MOFs along with molecular simulation studies of adsorption and diffusion of methane and hydrogen are discussed. All water and solvent molecules were removed from the MOFs prior to characterisation and simulations.

3.5.1 Building units and geometric characterisation

Characterisation of MOFs is of great importance as it provides useful information for example to understand better the adsorption behaviour in MOFs. Here, the pore size distribution (PSD), the surface area and pore volume measurements are reported.

The PSDs for the Cu-, Co-, and Cd-MOF are shown in Figure 3-18 and were obtained by the method described by Gelb and Gubbins (1998) which determines the diameter of the largest sphere that can fit in the cavities without overlapping with framework atoms. To understand better the complex pore shape of these structures, a probe molecule with an arbitrary diameter of 2.75 Å was inserted randomly in the pore space and tested for overlap with the framework atoms as described by Sarkisov and Harrison (2011). Figure 3-19 shows the vdW representation of successful insertions for all three structures illustrating the accessible pore space.

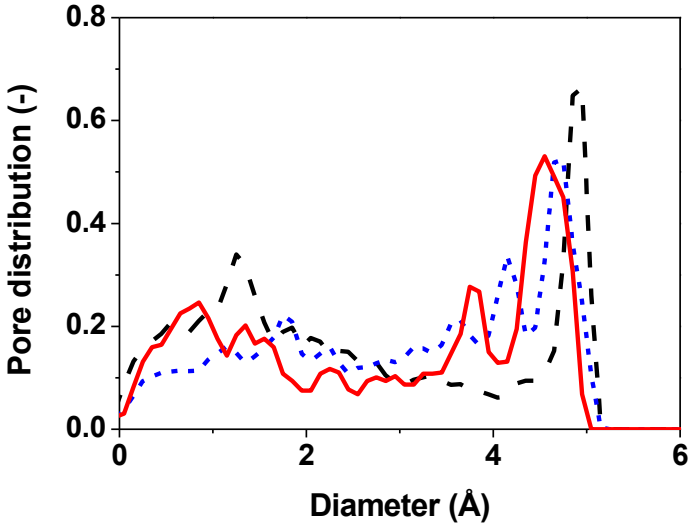

Figure 3-18: Pore size distribution for Cu-MOF (dashed black line), Cd-MOF (dotted blue line) and Co-MOF (solid red line).

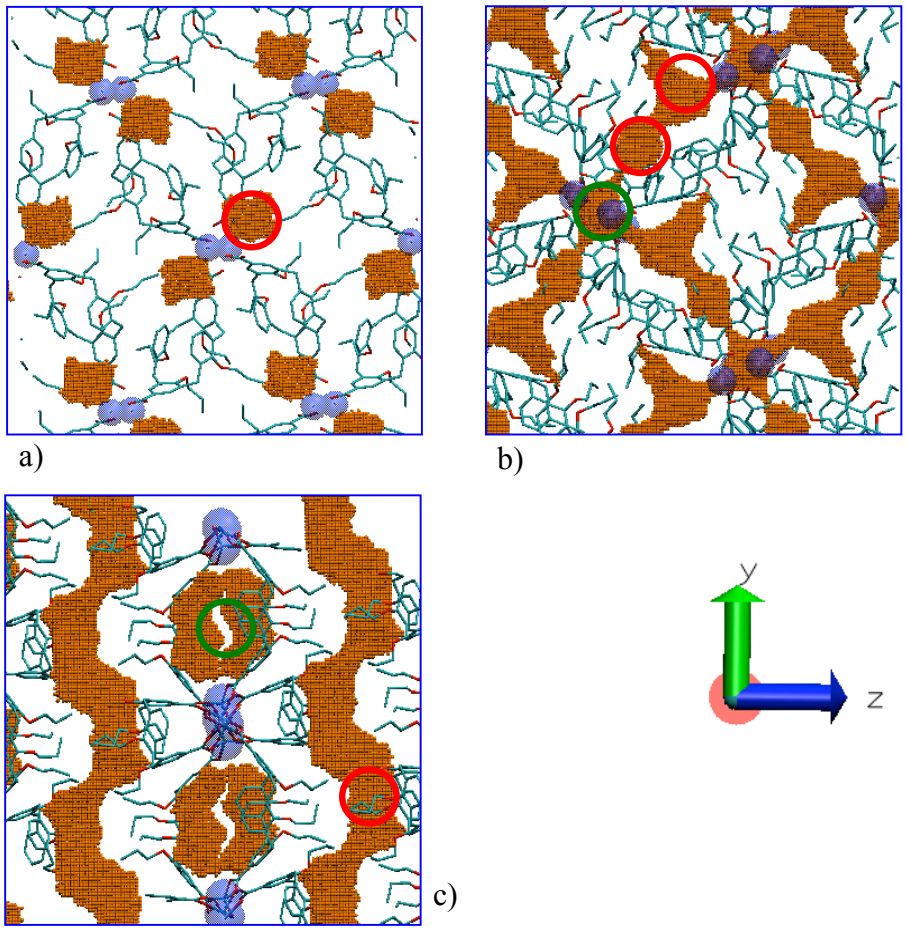

Figure 3-19: Schematic view of the pore space for a) Cu-MOF, b) Cd-MOF and c) Co-MOF calculated with a probe size of 2.75 Å. The orange aperture shows the available pore space in the vdW representation. Metal clusters are shown in transparent blue spacefill representation. Pore diameters obtained from the pore size distribution are marked with green and red circles for large and small pores, respectively.

The structure of the Cu-MOF consists of paddle wheel $Cu_2(O_2)_4$ metal clusters linked by the calix-dicarboxylates into three-dimensional network of sheets. The pore size distribution for this structure revealed pores with a diameter close to 4.9 Å. This peak corresponds to the area between linkers of adjacent metal clusters as marked in Figure 3-19a. The space between the linkers is fairly jammed due to the presence of propyl groups. The Cd-MOF contains square $Cd_2(O_2)_8$ metal clusters connected to H_2caldc linkers forming chains of three-dimensional sheets. Three peaks can be identified for Cd-MOF in the PSD. The largest at 4.8 Å corresponds to the void

between repeating metal clusters along the *x* axis (see the green circle in Figure 3-19b). The other two peaks correspond to the empty space between the caldc linkers as illustrated by the red circles in Figure 3-19b. The Co-MOF has $Co_4(OH)_2(O_2)_6$ units, that are linked together by single cobalt centres into chains with the propyl groups of each caldc protruding in the centre of the sheets. The space encountered between metal clusters along the *y* axis (green circle) and the channel-like pores (red circle) form the two pores in Co-MOF as shown in Figure 3-18 and Figure 3-19c.

Table 3-2 shows a comparison between the surface areas and geometric void fractions for the MOFs studied. The accessible surface area is a geometric surface area mapped out with the centre of a probe rolled across the surface of the framework atoms. Nitrogen and hydrogen probes were used in this study with sizes of 3.68 Å and 2.95 Å respectively. The accessible surface area measured with the nitrogen-sized probe molecule in general compares well with experimental BET surface areas (Brunauer *et al.* (1938)) for activated samples and therefore can provide an indication about the quality of the sample and the activation procedure (Düren *et al.* (2009), Düren *et al.* (2007)).

The void fraction is the empty space of a structure divided by the total volume. To calculate the free volume, a 0 Å sized probe is randomly inserted in the unit cell and tested for overlap with the framework atoms. The pore volume is then calculated by multiplying the void fraction (ratio of successful insertions to the total number of insertions) by the unit cell volume.

Table 3-2: Geometric characterisation and unit cell dimensions of calix-based MOFs studied.

	Cd-MOF		*Co-MOF*		*Cu-MOF*	
	N_2	H_2	N_2	H_2	N_2	H_2
Accessible surface area (m^2/g)	410	913	441	792	190	393
Geometric void fraction	0.46		0.43		0.38	
Unit cell dimensions ($Å^3$)	15.6×24.9×25.3		13.8×16.0×22.3		9.5×26.3×17.6	

The simulated accessible surface area and void fraction data for these MOFs are relatively modest with larger values for the Cd- and Co-MOFs. It is noteworthy to mention that the data shown in Table 3-2 are calculated from perfect crystal structures of MOFs. This means that all solvent molecules were removed prior to these calculations. The experimental surface area values obtained for all three structures were also insignificant as after the activation treatment, the MOFs were shown to have poor crystallinity. Moreover, powder X-ray diffraction and thermogravimetric analysis data obtained from our experimental collaborators at the University of Bath suggest that upon removal of solvent DMF molecules, the structures show some degree of framework collapse and therefore loss of porosity is observed (Bew *et al.* (2012)).

3.5.2 Single component adsorption isotherms

To examine computationally the guest sorption capabilities of these three MOFs containing bowls of H_2caldc as linkers, molecular simulations of methane and hydrogen adsorption were performed for all three structures. All solvent molecules were removed before carrying out the simulations assuming perfectly activated frameworks. Figure 3-20 shows simulated adsorption isotherms for methane at 300 K for all three calix-based MOFs. Although the shape of the isotherms is similar, the amount of methane adsorbed in Cd-MOF and Co-MOF is higher than that in the Cu-

MOF throughout the whole pressure range. The adsorption isotherm for the Cu-MOF has a less steep slope and reaches the adsorption plateau at 5 bar. This difference in adsorption can be attributed to the presence of multiple adsorption sites in the Cd- and Co-MOFs.

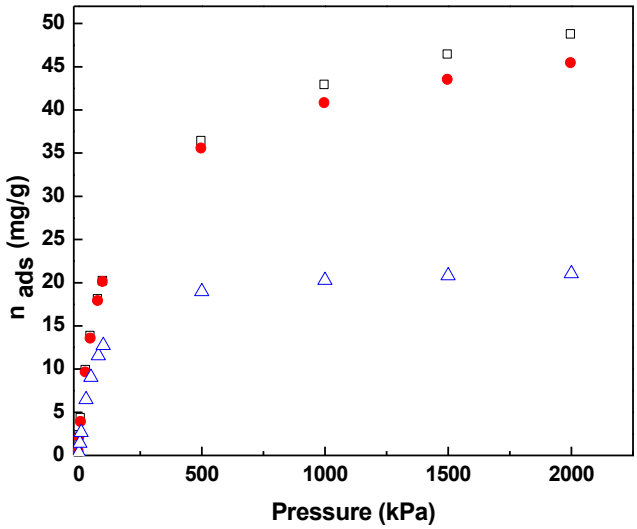

Figure 3-20: Pure component adsorption isotherms for methane at 300 K. Cd-MOF (open squares), Co-MOF (closed circles) and Cu-MOF (open triangles).

In order to examine the reasons for the significantly different adsorption properties of these rather similar MOFs, the snapshots for methane at 20 bar are given in Figure 3-21 for all three frameworks. In most MOFs, preferential adsorption occurs around the metal clusters. Similarly, in the case of the Cu-MOF, the preferential adsorption position for methane is close to the paddle-wheel metal units. The arrangement of the propyl groups does not allow methane molecules to fully occupy the region between the linkers as is also shown in Figure 3-19. As most of the adsorption takes place near this region (Figure 3-21a), the void between metal clusters becomes quickly saturated. In contrast, in the Cd-MOF and the Co-MOF several favourable adsorption sites can be identified. In the Cd-MOF, at lower pressures, methane molecules sit in two preferential regions in the space between the metal clusters and the neighbouring calix bowls as shown by the blue circle in Figure 3-21b. The third site gets occupied at higher methane loadings and corresponds to the space between the linker tails

where there is less propyl group entanglement as shown by dashed red circles in Figure 3-21b. These three sites correspond well with the three types of pores found in Figure 3-18 and Figure 3-19. Similar adsorption sites were observed for the case of the Co-MOF. In the Co-MOF, at lower pressure, the region between the calix linkers and close to the metal cluster is the most favourable site (see blue circle in Figure 3-21c). The second area corresponds to the void between the sheets where propyl group are protruding towards the centre as marked with the dashed red circle. It is important to note that the metal sites in all structures were shielded by the organic ligands and surrounding oxygens and therefore were not exposed in the pore space average distance of 5-7 Å between methane and adsorption sites near metal clusters.

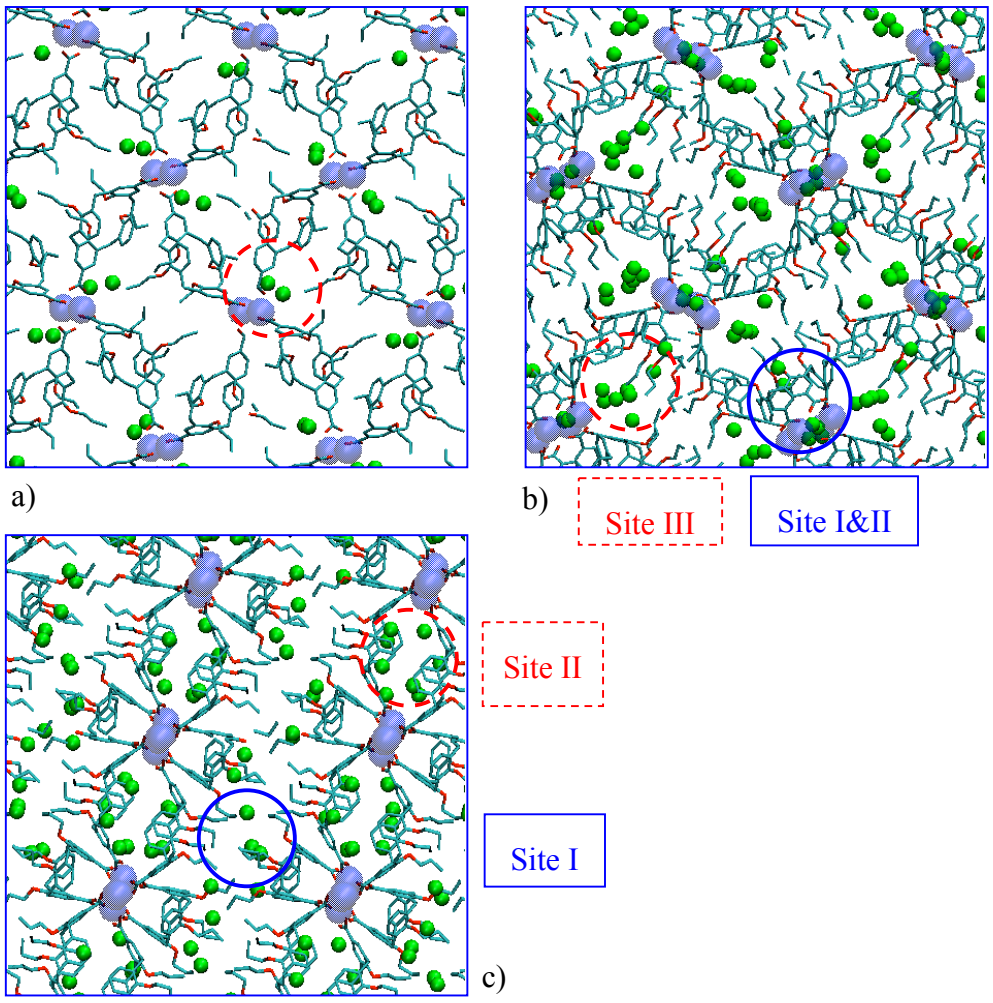

Figure 3-21: Snapshots for methane adsorbed in a) Cu-MOF (3), b) Cd-MOF (2) and c) Co-MOF (1) at 20 bar and 300 K. The green methane molecules are shown in CPK representation; metal clusters are shown in transparent blue spheres. Note that in all three cases, the calix[4]arene bowls are inaccessible to methane.

The adsorption isotherms for hydrogen at 77 K for three structures are shown in Figure 3-22. Similar to the trend observed for methane adsorption, the amount of hydrogen adsorbed is higher in the Cd-MOF followed by the Co- and Cu-MOF. The slope of the curve in the low-pressure region is less sharp for the Cu-MOF and the isotherm reaches its plateau at lower loadings.

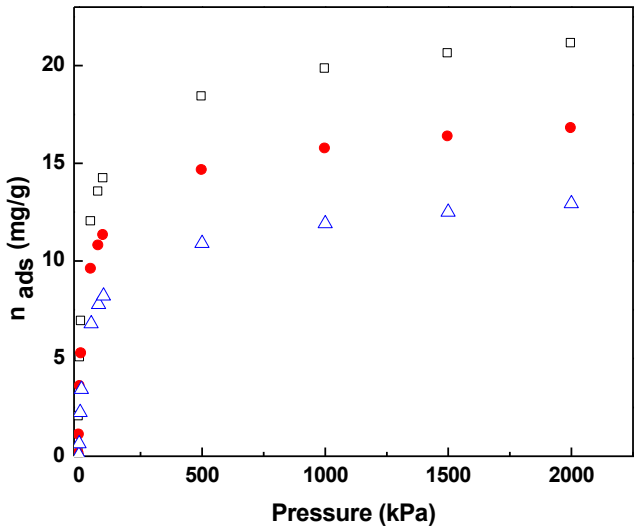

Figure 3-22: Pure component adsorption isotherms for hydrogen at 77 K. Cd-MOF (open squares), Co-MOF (closed circles) and Cu-MOF (open triangles).

Figure 3-23 shows snapshots of hydrogen molecules in all three frameworks at 77 K and 20 bar. Although the number of hydrogen molecules packed together is higher than methane due to their smaller size, the adsorption sites for hydrogen are similar to those seen for methane. However, interestingly, an additional adsorption site is observed in the Cd-MOF. As illustrated in Figure 3-23b in the case of the Cd-MOF framework, the bowl structure of the calix[4]arene linker provides extra site for hydrogen molecules in addition to the ones observed for methane (Figure 3-21). This is in agreement with the structural data that shows only the Cd-MOF exhibits an open conformation of the caldc bowl.

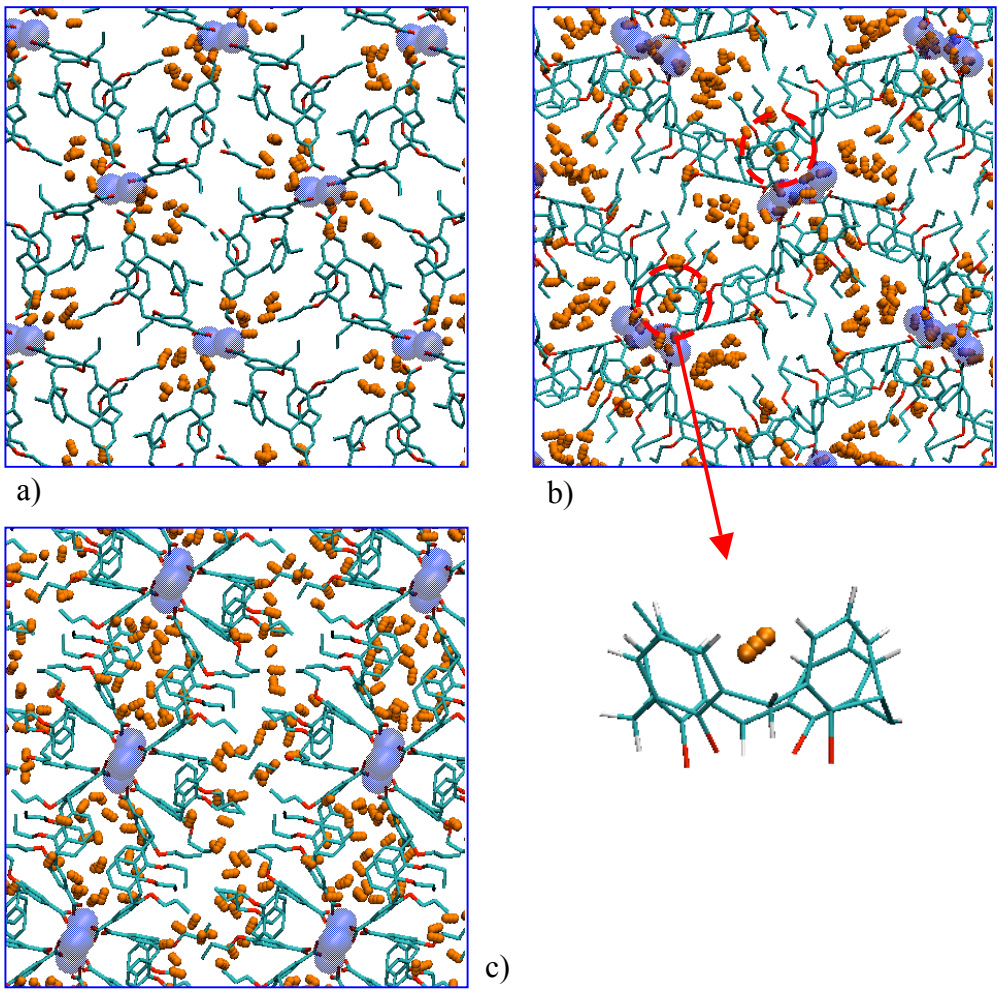

Figure 3-23: Snapshots for hydrogen adsorbed in a) Cu-MOF, b) Cd-MOF and c) Co-MOF at 20 bar and 77 K. Hydrogen is represented by orange spheres, metal clusters are shown in transparent blue spheres. Note that only in the Cd-MOF the calix[4]arene bowl is accessible to hydrogen as illustrated by the dashed red circles.

3.5.3 Mixture adsorption simulations

For the methane and hydrogen adsorption in a gas mixture, not only the total amount adsorbed is important but also the selectivity of one component over the other. To further investigate how well these MOFs perform in separating methane and hydrogen, molecular simulation of equimolar mixtures were carried out over the entire pressure range at 300 K.

For binary mixtures, the equilibrium selectivity is defined as:

$$S_{CH4/H2} = \frac{x_{CH_4} / x_{H_2}}{y_{CH_4} / y_{H_2}} \qquad \textbf{3-2}$$

where x_i denotes the mole fractions of the component i in the adsorbed phase and y_i the mole fraction in the gas phase. Values greater than unity mean that methane is more strongly adsorbed than hydrogen. Figure 3-24 compares the selectivity of methane over hydrogen for the MOFs studied with other MOFs in the literature. The simulation results show that all three structures demonstrate better methane selectivities varying between 110 to 150 at 1 bar and between 40 to 50 at 20 bar. These values are higher than simulated selectivities observed in other MOFs reported in the literature ranging from ~5 to 30 (Yang and Zhong (2006), Gallo and Glossman-Mitnik (2009)). These other MOFs contained simple and large pores, thus at the studied pressure range they are not yet saturated. Therefore, the packing effects are insignificant and resulting in rather low selectivities. As shown in Figure 3-24, the selectivities observed in the calix MOFs are in the same order of magnitude of what is observed in a MOF called Zn(tbip) (tbip = 5-*tert*-butylisophthalate) where the selectivity varies between 125 to 180 (Liu and Johnson (2009)). This high selectivity was determined to be mainly due to narrow pore size of Zn(tbip) cavities. The MOFs studied in this thesis have also comparable pore sizes to the diameter of methane molecules that leads to higher selectivity values. This means that hydrogen adsorption is significantly affected by the presence of methane (the more strongly adsorbing molecule). At high pressures, hydrogen exhibits more substantial pore fillings and packing effects become significant for hydrogen, leading to a decrease in methane selectivity with further increasing pressure.

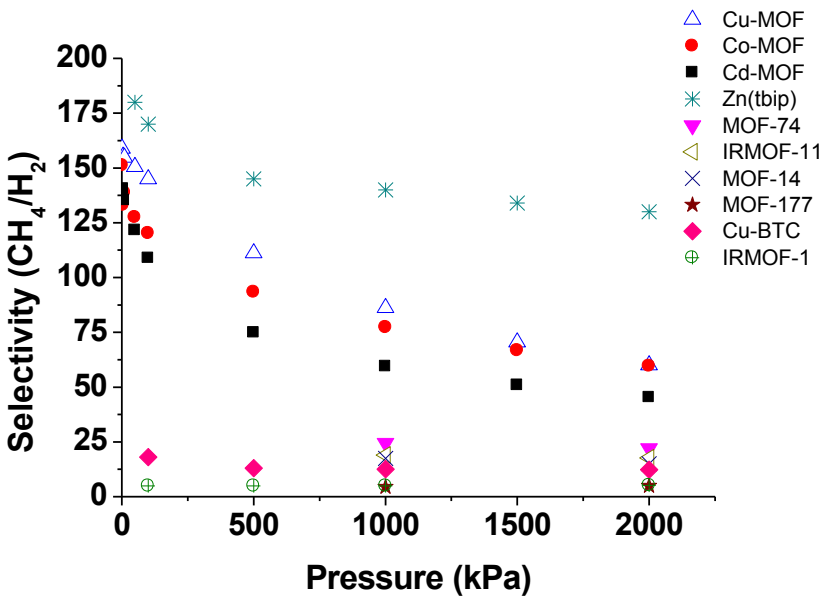

Figure 3-24: Adsorption selectivity for CH_4 over H_2 at 300 K for an equimolar mixture of methane and hydrogen (Yang and Zhong (2006), Gallo and Glossman-Mitnik (2009), Liu and Johnson (2009)).

To calculate various diffusivities as a function of the concentration of methane and hydrogen, and to understand better the dynamics of the molecules in these three MOFs, molecular dynamics simulations in the canonical ensemble were performed. The technical details of such calculations have been discussed in chapter 2. The MD simulations used a time step of 0.5 fs and were performed using the Nosé-Hoover thermostat and velocity-Verlet algorithm to calculate molecules trajectories. Self-diffusivities for methane and hydrogen were calculated from the slope of the MSD curves of the molecules after equilibrium (see the Einstein equation 2-16) and are presented in Figure 3-26 as a function of concentration. Figure 3-25 shows an example of MSD curves as a function of time used to calculate self-diffusion at long times for the loading of 10 molec/uc for both methane and hydrogen.

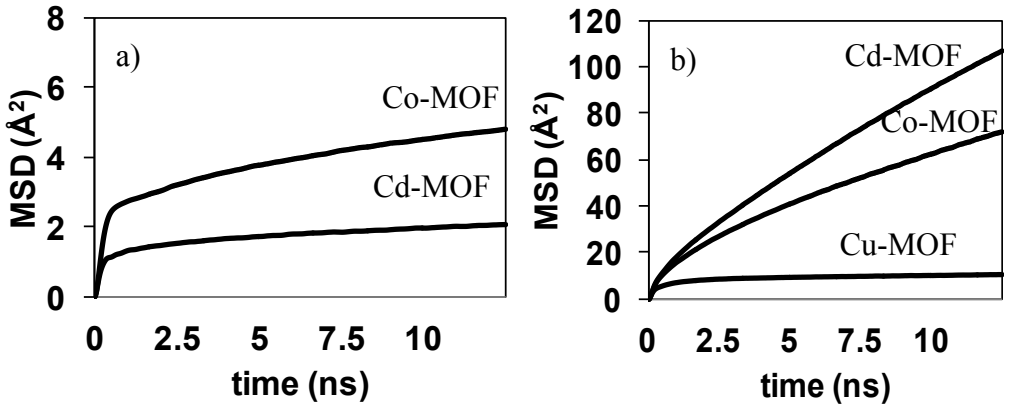

Figure 3-25: Simulated MSD curves vs. time for a) methane and b) hydrogen at 10 molec/uc.

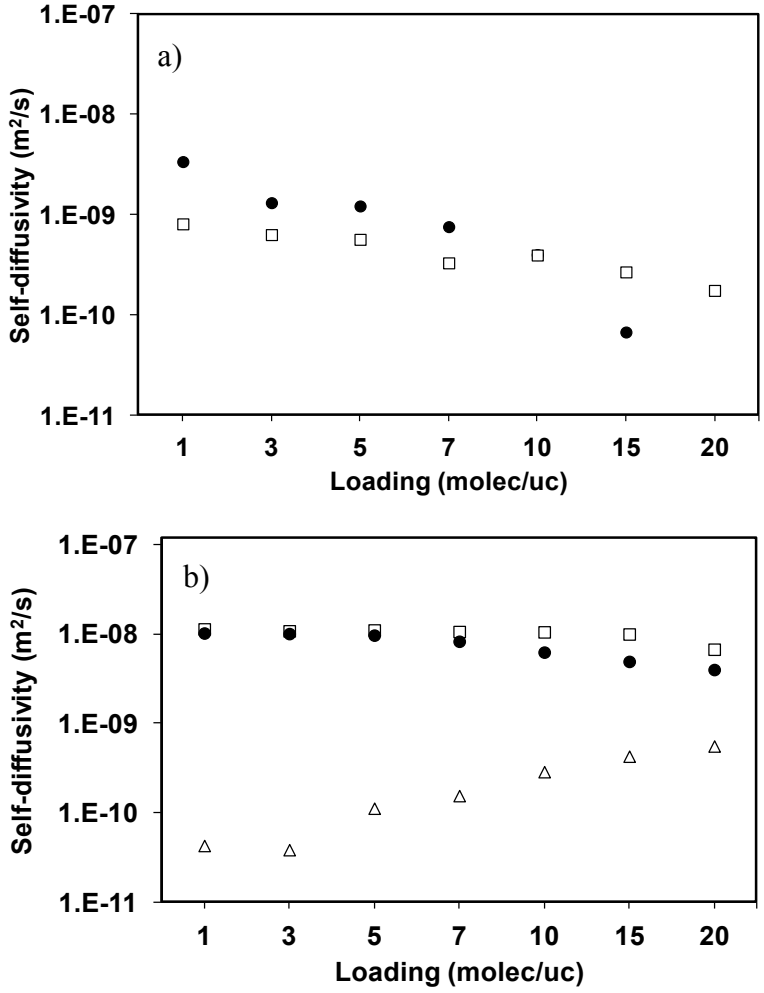

Figure 3-26: Self-diffusion coefficients obtained from molecular dynamics simulations for a) methane and b) hydrogen at different loadings and 300 K. Cd-MOF (open squares), Co-MOF (closed circles) and Cu-MOF (open triangles).

Examination of trajectories for methane molecules in Cu-MOF showed that the pore space is too small for the methane molecules to exhibit diffusional behaviour (as the space between propyl entanglements is not accessible to methane), hence the dynamics of these molecules are mostly vibrational. Therefore, the MSD curves resembles the ones obtained for TBC4 structures and do not change linearly with time. This suggests that methane molecules are localised in the Cu-MOF pores and their motion is influenced significantly by the pore's tightly confined environment. In contrast, multiple inter-connecting pores in the Cd- and Co-MOFs (see Figure 3-19) give rise to molecular motion. However, because of the relatively small pore volume of these MOFs, the saturation capacity is reached at lower loadings when compared to those of MOFs with larger pores. Therefore, the diffusion coefficients are rather small. For example in a MOF with large pores and windows like IRMOF-1, even at high loadings of 100 molec/uc of methane, the diffusivities are much larger with a range of ~ 10^{-7} to 10^{-8} m^2/s (Skoulidas and Sholl (2005)). In the three MOFs studied here, at higher loadings, steric hindrance effects cause a further lowering of the molecules motion and self-diffusivities drop to 10^{-10} to 10^{-11} m^2/s as shown in Figure 3-26a. In the case of hydrogen, the magnitude of the self-diffusivities is larger than methane. This was expected as the smaller hydrogens have more room in the pore cavities to move around freely. The concentration dependence of self-diffusivity shows a moderate decrease in the case of the Cd-MOF. This decrease is more prominent for the Co-MOF. This concentration dependence in self-diffusivity is common in porous materials, as the guest-guest interactions become a dominant factor at higher loadings and lower mobility of guests are observed. In the Cu-MOF, the movement of hydrogen molecules is again strongly affected by the pore confinement and therefore the self-diffusivity values are very low compared to the ones for the Cd- and Co-MOFs. To further analyse if adsorbates interact with the metal sites in all three MOFs, radial distribution function of hydrogen and methane centre of mass with all MOFs metal atoms were also calculated and are shown in Figure 3-27. It can be seen that the first peaks for hydrogen and methane occurs at distances larger than 4 and 5 Å respectively. In consistence with GCMC simulation results, this further proves that the adsorbates are positioned slightly apart from the shielded metal sites due to the presence of surrounding oxygen atoms.

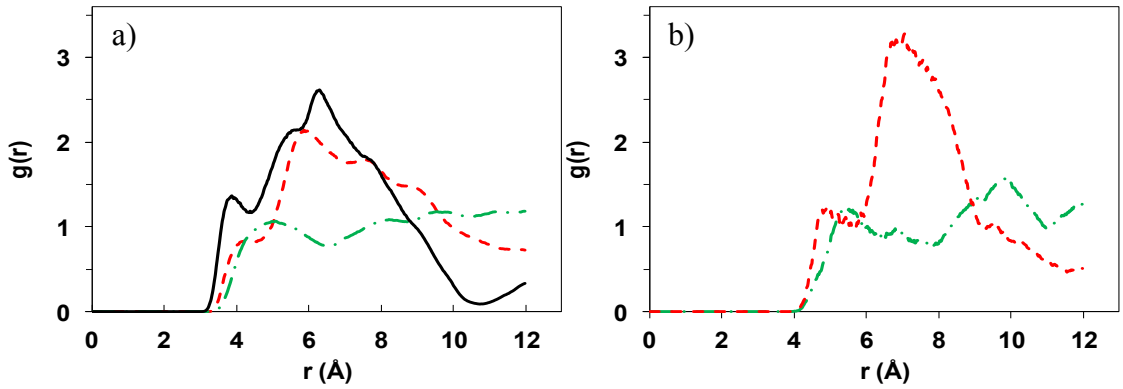

Figure 3-27: Radial distribution functions for a) H_2 and b) CH_4 in Cu-MOF (black solid), Co-MOF(green dotted-dashed) and Cd-MOF (red dashed) at 10 molec/uc and 300K.

3.6 Conclusions

In this Chapter, molecular simulation of adsorption and diffusion were employed to study *tert*-butylcalix[4]arene (TBC4) compounds. It was shown that TBC4 cages are capable of forming host-guest systems with molecular recognition behaviour with preferential adsorption towards methane over hydrogen. A close examination of MSD and VACF revealed vibrational mobility of both methane and hydrogen in the TBC4 cages and showed stronger interaction energies for methane.

Using the combination of synthesis, molecular simulations and experimental approaches, MOFs with TBC4-based linkers were produced. The synthesis of the calix-based linkers was carried out in a six-step procedure to form an upper-rim functionalised calixarene-dicarboxylate before being used in the MOF synthesis. A unique characteristic of the produced MOFs lies in the two types of porosity associated with both linker and the structural framework. Molecular simulation of adsorption and diffusion showed high selectivity values of preferential methane adsorption over hydrogen. The high selectivity values were largely dictated by the pore size selectivity as the energetic effects favours methane. This suggests that the characteristics of these MOFs can lead to general design strategies for synthesising news MOF adsorbents with desired methane selective properties. Remarkably, it was shown that the TBC4 bowl in the Cd-MOF is accessible to only smaller hydrogen

molecules (Figure 3-28). This, in principle, could also be further exploited for selective adsorptive separations. Despite the fact that it has not been possible to activate the MOFs studied without some degrees of structure collapsing, the simulations suggested that these three MOFs, display interesting gas adsorption behaviour and selectivity.

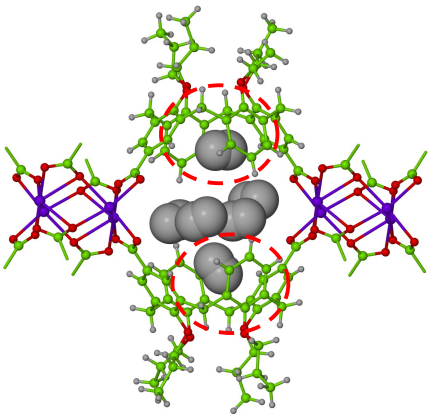

Figure 3-28: Snapshot of hydrogen adsorption (grey spheres) in Cd-MOF, showing adsorption into the calix[4]arene bowl (dashed red circles).

Further simulations with various calix-based linkers and different functionalisations on upper- and lower-rims of TBC4 should be the subject of future study to better understand their effect on pore size, topology and ultimately their adsorptive behaviour. The simulation results should provide a platform for optimized design patterns for future experimental work to minimise trial-and-error scanning of these complex MOFs properties. In an industrial context, calix-based MOFs with better chemical stability should be considered by adding neutral bridging co-ligands in order to prevent the formation of structures with coordinated solvent linkers and using more rigid calixarene ligands. Simultaneous higher adsorption capacity and high selectivity as well as economically viable scale-up costs must also be assessed.

Chapter 4 Molecular Simulation Studies of Xylene Separation in Metal-Organic Frameworks

In this chapter, MOFs are assessed for the separation of xylene isomers using molecular simulations in MOFs with various pore sizes and shapes. First, it is explained why the separation of xylene isomers is of importance in petrochemical industries and then some of the existing industrial separation mechanisms are briefly reported. Next, the simulation details are given. The strong correlation between pore size in MOFs and their capability to select one isomer over the other is examined in the following sections. Section 4.3 examines low xylene selectivity in MOFs containing large pores. Section 4.4 investigates oX selectivity in MOFs with medium range pore sizes. Section 4.5 provides detailed analysis of competitive adsorption of xylene molecules in MOFs with smaller pores with a particular focus on MIL-125 and MIL-125-NH_2. Finally, the conclusions are given in Section 4.7.

4.1 Introduction

Xylenes are aromatic compounds with a single benzene ring and two methyl groups at the 1,2, 1,3 and 1,4 positions forming ortho-xylene (oX), meta-xylene (mX) and para-xylene (pX), respectively. Xylenes are important industrial raw chemicals and are produced in mixtures from primary distillation of petroleum. In order to use each xylene in its pure form and relevant application, it is necessary to separate them. The most valuable feedstock is pX which is oxidised to form terephthalic acid and is widely used in the polyester and clothing industry (Scheirs and Long (2005)). mX and oX are used to produce phthalic anhydride and isophthalic acid, respectively (Moreira *et al.* (2012)). The detection of individual xylene isomers is also of great importance in air monitoring (Yassaa *et al.* (2006)) and blood analysis (Hattori *et al.* (1998), Gu and Yan (2010)).

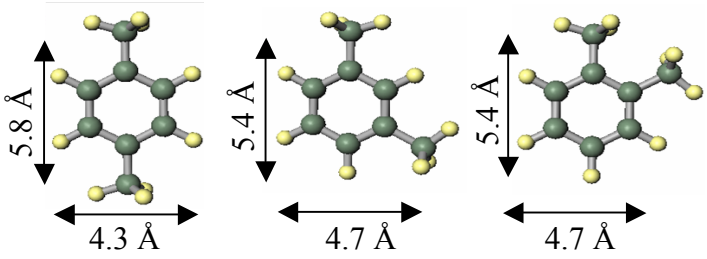

para-xylene	*meta*-xylene	*ortho*-xylene
bp: 138.5 °C	bp: 139.3 °C	bp: 144.5 °C
mp: 13.3 °C	mp: -47.9 °C	mp: -25.2 °C

Figure 4-1: Characteristics of xylene isomers. Xylenes show similar boiling points (bp) and different melting points (mp).

The separation of xylene isomers is challenging. Because xylenes are isomers and have similar physiochemical properties, it is very difficult and costly to separate them using classic methods such as distillation due to their close boiling points (see Figure 4-1). On the other hand, their crystallisation temperatures are sufficiently different that it can be used to separate xylene isomers on an industrial scale. In crystallisation, the process is operated at the triple point at which the xylene mixture

is simultaneously vaporised and crystallised due to the three-point equilibrium. This process is continued until the liquid phase is removed and pure crystals remain in the feed (Shiau *et al.* (2008), Weissermel and Arpe (2008)). This process was widely used to separate pX from mixed xylene streams until the 1970s with a 60-70 % pX recovery (Weissermel and Arpe (2008)).

In later years, more efficient separation methods using porous solids as adsorbents have emerged. Different modes of interaction between xylenes and the porous solids are the driving force to discriminate between xylene isomers. For example, the PAREX process developed by UOP is used to separate pX from the other isomers. In this method, a pX selective zeolite (i.e. MFI and Zeolite X and Y with Na^{+}, K^{-} and Ba^{2+} as extraframework cations) are used in a packed bed adsorption column in a simulated moving bed (SMB) to separate pX from the other isomers (Kurup *et al.* (2005)). The selective adsorption in zeolites of one isomer over another depends mainly on the nature and the number of extraframework cations (Lachet *et al.* (1999)) and molecular sieving effects (Guo *et al.* (2000)). This method yields better pX selectivity than crystallisation (95% pX recovery compared to 60-70%) and is more economical (Minceva and Rodrigues (2005)). Currently, about 60% of pX produced worldwide is based on adsorption technology (Bárcia *et al.* (2012)).

Porous MOFs have shown remarkable potential for various separation purposes due to versatile structures (Li *et al.* (2009)). Unlike zeolites, the pores in MOFs can be systematically built from numerous choices of metal clusters and organic linkers suitable for more efficient xylene separation. Given the great number of MOFs reported so far in the literature, it is advantageous to computationally narrow down the search to only the most promising structures. In what follows the performance of a number of MOFs for their selectivity towards a particular xylene isomer is examined by looking at interaction energies, packing and molecular sieving effects.

4.2 Simulation Details

The adsorption isotherms of xylene isomers were computed using grand canonical Monte Carlo (GCMC) simulations. These simulations were carried out in the Multipurpose-Simulation-Code, Music (Gupta *et al.* (2003)). Monte Carlo moves for xylenes included insertion, deletion, translation and rotation. In the case of binary mixtures, identity swap moves were also used for faster equilibration times. The simulations consisted of 150-200$\times 10^6$ equilibrium steps followed by an additional 100-150 $\times 10^6$ production steps.

The input fugacities for the GCMC simulations were calculated from the Peng-Robinson equation of state. The simulation cell consisted of eight (2×2×2) unit cells for all MOFs investigated except for MIL-53 where 32 unit cells were used for better statistics. The framework atoms of all MOFs studied were kept fixed at their crystallographic positions.

The Lennard-Jones potential was used to calculate the energy of interactions with a cut-off distance of 15 Å. The interaction parameters for the MOFs were taken from the Universal Force Field (UFF) by Rappe *et al.* (1992). The OPLS force field was used to model the xylene isomers (Jorgensen and Nguyen (1993)). In this model, all atoms are defined explicitly except for the CH_3 groups which were modelled as a single sphere. Lorenz-Berthelot mixing rules were applied for atom pair interactions. The Ewald summation method (Dufner *et al.* (1997)) was used to calculate the electrostatic interactions between the xylenes and the frameworks, while xylene-xylene interactions were estimated using the technique described by Wolf *et al.* (1999). Partial charges for the frameworks, derived from density functional theory (DFT) calculations were obtained from the literature (Farrusseng *et al.* (2009), Yazaydin *et al.* (2009)). Partial charges for MIL-125 and MIL-125-NH_2 were obtained from Guillaume Maurin's group at the University of Montpellier II in France.

4.3 MOFs with large pores (d > 9 Å)

In this section, MOFs with relatively large pores are studied for the separation of xylene isomers. Five large pore MOFs with pore diameters larger than 9 Å were chosen which are all illustrated in Figure 4-2. CPO-27 has one-dimensional hexagonal pores. In contrast, CuBTC has a cubic structure containing three different pores. Three members of isoreticular MOF family (i.e. IRMOF-1, IRMOF-3 and IRMOF-7) were also studied. These frameworks have rather similar pore sizes and topologies with different organic linkers which enables understanding subtle effects of linkers on the xylene separation characteristics of these MOFs. Framework topologies, pore sizes and linkers of all MOFs studied in this section are summarised in Figure 4-2.

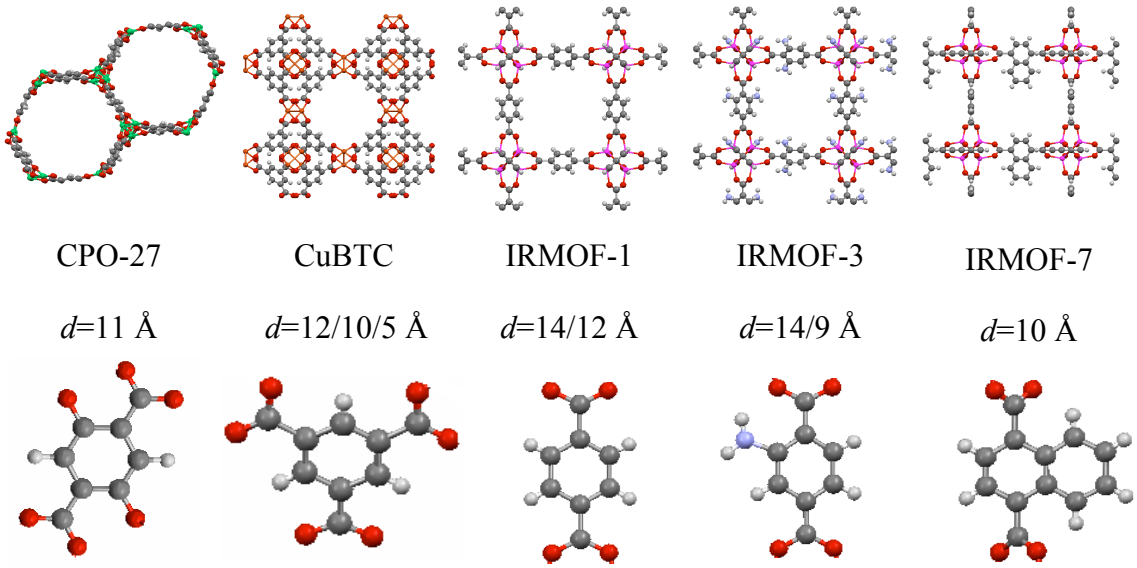

Figure 4-2: MOFs containing large pores studied in this work. Pore diameters and corresponding organic linkers are shown under each framework.

4.3.1 CPO-27(Ni) and CuBTC

The CPO-27(Ni) structure comprises helical chains of nickel octahedral linked together by the 2,5-dihydroxyterephthalate linkers. This combination forms one-dimensional hexagonal channels with a diameter of 11 Å. Complete desolvation of CPO-27 leads to formation of open metal sites pointing toward the channels. In order to investigate the adsorption strength of different xylenes in the large pores of CPO-

27, pure component and mixture adsorption simulations were carried at 300 K. The adsorption isotherms for pure component xylenes are shown in Figure 4-3.

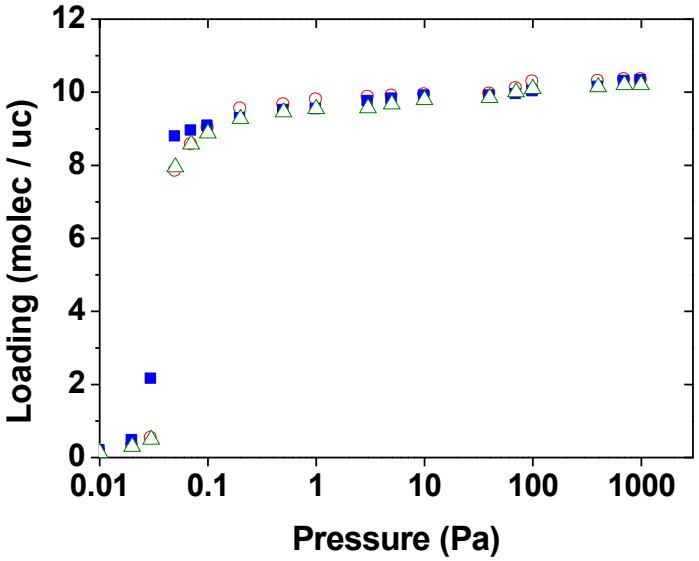

Figure 4-3: Pure component adsorption isotherms for xylene isomers at 300 K for CPO-27(Ni). pX (open circles), oX (closed squares) and mX (open triangles).

As shown in the isotherms, in CPO-27, more oX is adsorbed at low loadings but the saturation capacity is similar for all xylenes. At low pressures unsaturated open metal sites in CPO-27 may affect the adsorption that can be better predicted using force fields derived from DFT calculations (Chen *et al.* (2012)). These sites become quickly saturated as the amount adsorbed is increased where generic force fields are useful for predicting adsorption. To examine how CPO-27 performs for selective adsorption, equimolar binary simulations were carried out at 300 K and different loadings which are shown in Figure 4-4. The results show overall low selectivities for this framework. The pX/mX mixture has an average selectivity of 1.03 meaning that neither isomer is adsorbed preferentially. In the case of oX/pX and oX/mX mixtures, oX is adsorbed preferentially with average low selectivities of ~1.4-1.5. This low selectivity does not change with the loading indicating that packing effects do not play an important role in large pores of CPO-27.

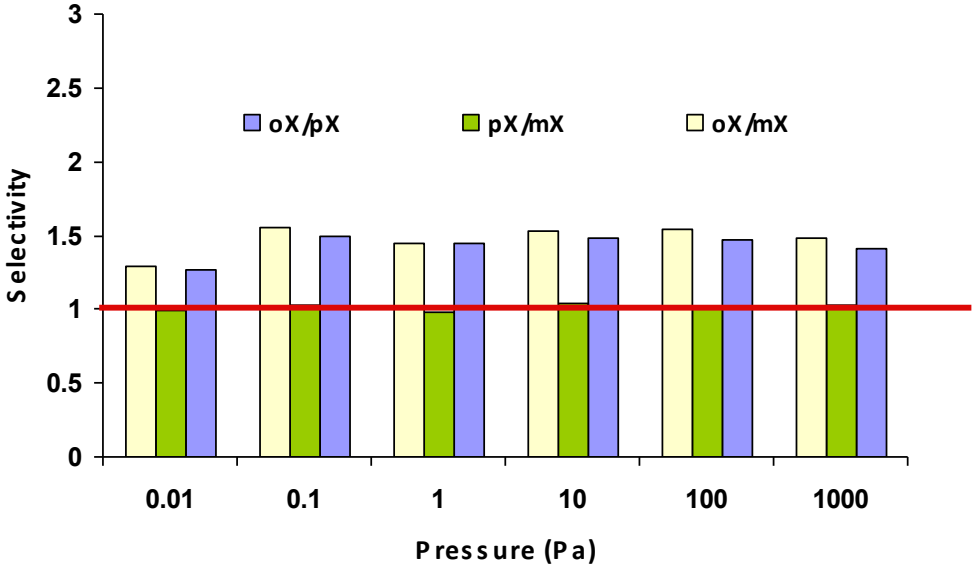

Figure 4-4: oX/pX , pX/mX and oX/mX equimolar mixture selectivities in CPO-27(Ni) at different pressures and 300 K.

In general, the adsorption snapshot presented in Figure 4-5 shows a low degree of order in the pores for xylenes for a mixture of oX/pX. This indicates that the large channels in CPO-27 do not impose a great deal of confinement on xylene molecules. Thus, the xylene isomers still leave some free space in the channels meaning that reorganization can occur relatively easily within the channels and no isomer is strongly favored over the other.

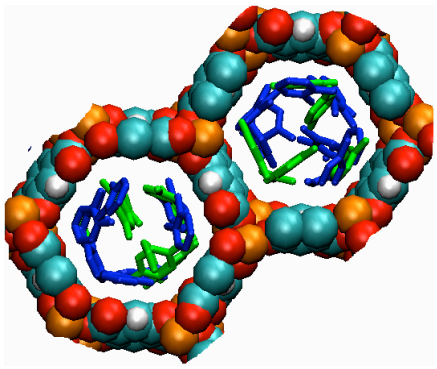

Figure 4-5: Mixture snapshot for oX (blue) / pX (green) at 1 kPa and 300 K in CPO-27(Ni). The hydrogen atoms on the xylene molecules are removed for clarity.

CuBTC ($Cu_3(BTC)_2$ with BTC = benzene-1,3,5-tricarboxylate) has a three-dimensional cubic structure with three types of cages with sizes of 5 , 10 and 12 Å. The large cages are connected to tetrahedral shaped pockets through triangular windows of 3.5 Å.

Predicted pure component isotherms for CuBTC for all xylene isomers at 300 K are shown in Figure 4-6. The amount of xylenes adsorbed is very similar throughout the entire isotherm with mX adsorbed least at lower loadings. Of all xylenes, the adsorbed amount for oX is higher than mX by only ~ 1.5 molec/uc at higher loadings.

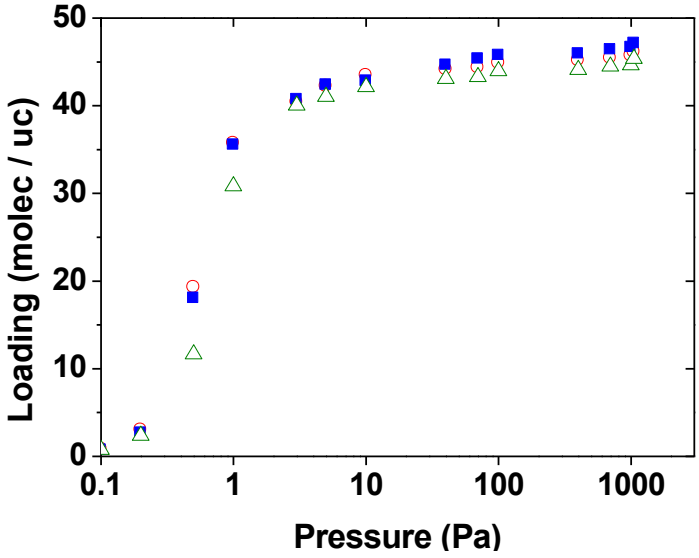

Figure 4-6: Pure component adsorption isotherms for xylene isomers at 300 K for CuBTC. pX (open circles), oX (closed squares) and mX (open triangles).

Equimolar mixture simulations were also carried out at various loadings (1, 10, 100 and 1000 Pa). Figure 4-7 shows that the selectivity is almost negligible at different loadings for the pX/oX mixture. The selectivity is slightly greater than unity for the pX/mX mixture and oX is slightly preferred in the oX/mX mixture with the average low selectivities of 1.3 and 1.2 for the pressure range studied. This rather constant

low selectivity with the degree of pore filling points to the fact that, similar to CPO-27, molecular packing does not play an important role.

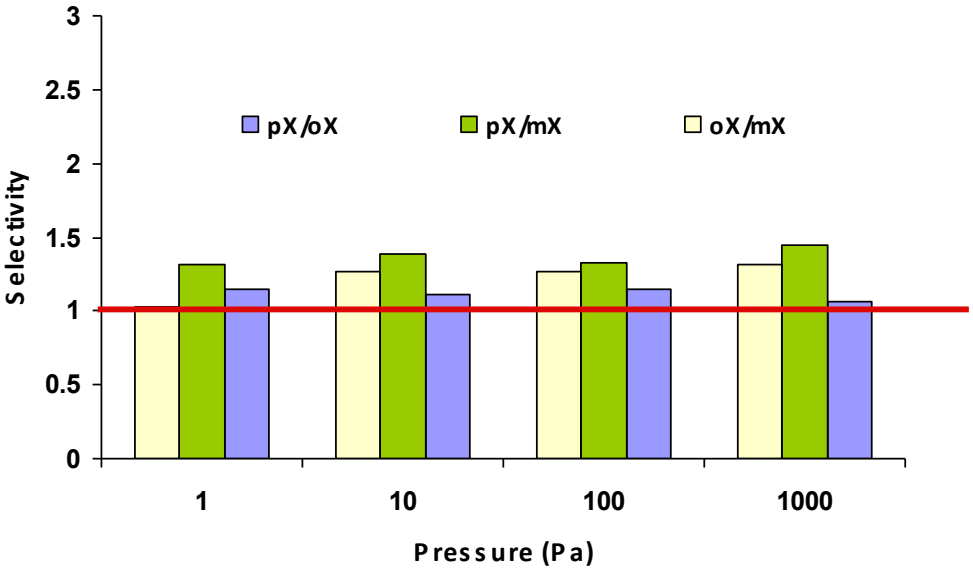

Figure 4-7: pX/oX , pX/mX and oX/mX equimolar mixture selectivities in CuBTC at different pressures and 300 K.

The density distribution of a pX/oX mixture giving the centre of mass locations of xylene molecules from thousands of configurations is shown in Figure 4-8. These locations show that the xylene molecules are adsorbed in a rather disordered fashion in the large cages with no strong preference for a particular isomer. The snapshot at high loading also shows that the smallest pores in Cu-BTC are not accessible to xylene isomers as marked with the red circle in Figure 4-8.

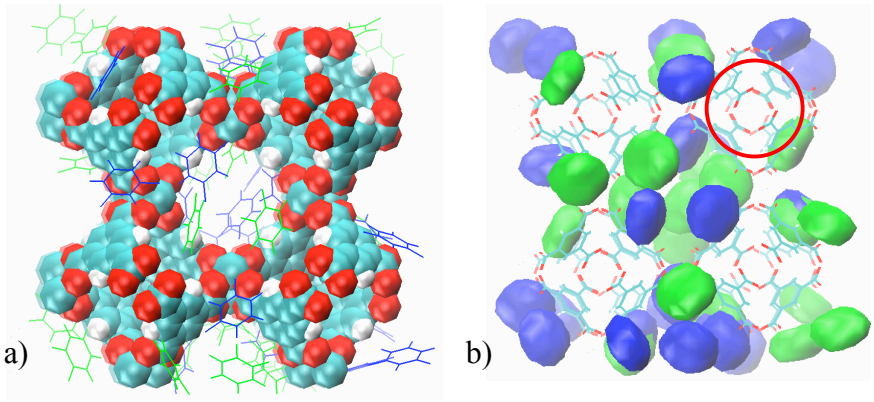

Figure 4-8: a) Snapshot and b) density distribution for a mixture of oX/pX at high loading and 300 K. pX isomers are shown in blue and oX in green. The small pores in Cu-BTC (marked by the red circle) are not accessible to xylene molecules.

4.3.2 IRMOF1, IRMOF-3 and IRMOF-7

IRMOFs comprise 3D periodic networks with cubic topologies formed by primary (metal cluster) and secondary (organic linker) building units. IRMOF-1 consists of Zn_4O metal clusters interconnected by six 1,4-benzenedicarboxylate (BDC) linkers. Other members of the IRMOF family are formed by substitution of the organic linker with different BDC derivatives or functionalisation of hydrogens or carbons of the linker. These manipulations result in changes in the pore size and shape of IRMOFs cubic lattice. For example, IRMOF-3 has the same Zn_4O clusters but the BDC linker is substituted with aminobenzenedicarboxylate (ABDC). Similar to IRMOF-1, the alternating orientation of these linkers inside and outside of the pores results in the formation to two peaks for their pore size distribution (Figure 4-9). In the case of IRMOF-7 the BDC linker is substituted with naphthalenedicarboxylate (NDC) resulting in only one pore type as they are orienting in the same way. In this section, these three MOFs (i.e. IRMOF-1, IRMOF-3 and IRMOF-7) are examined for their xylene selectivity behaviour. As these structures share rather similar pore topology, these MOFs allow investigating the influence of different organic linkers on preferential adsorption towards a specific isomer. The pore size distribution of the these MOFs are shown in Figure 4-9 and are calculated by the method described by Gelb and Gubbins (1998).

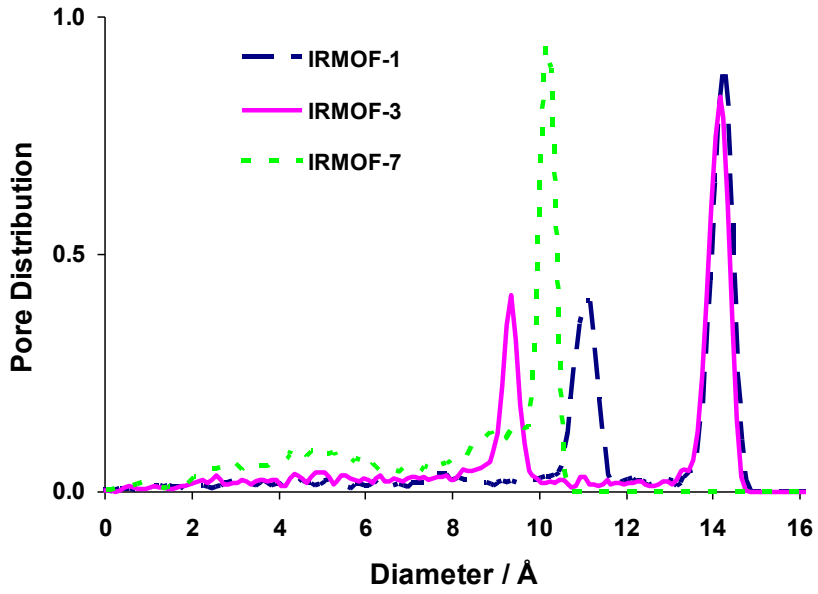

Figure 4-9: Pore size distribution calculated for IRMOF-1, IRMOF-3 and IRMOF-7 calculated by the method described by Gelb and Gubbins (1998).

In order to understand better the pore and window shape of these MOFs, a probe molecule with a diameter of 4 Å was inserted randomly in the pore space and tested for overlap with the framework atoms as described by Sarkisov and Harrison (2011). Figure 4-10 shows the vdW representation of successful insertions for IRMOF-1, IRMOF-3 and IRMOF-7 illustrating the accessible pore space. As can be seen, IRMOF-1 and IRMOF-3 contain large square windows (red dashed marks) connecting cubic pores. The diameter of the largest sphere that can percolate through IRMOF-1 and IRMOF-3 is 7 and 6 Å, respectively. In IRMOF-7 framework, the available pore space is restricted by the protruding NDC linker making the framework windows narrower with a rectangular shape and only spheres with a diameter up to 4 Å can percolate through the structure (see the dashed blue rectangle in Figure 4-10).

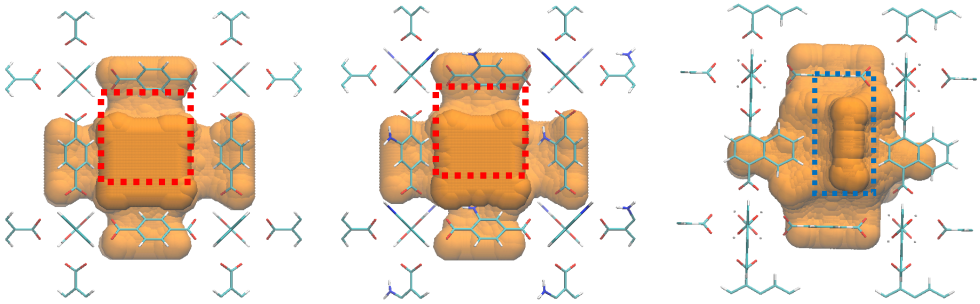

Figure 4-10: Schematic view of the available pore space in IRMOF-1 (left) , IRMOF-3 (middle) and IRMOF-7 (right) calculated with a probe size of 4 Å by a method described by Sarkisov and Harrison (2011). The rectangular windows in IRMOF-1 and IRMOF-3 are marked in red, while the one in IRMOF-7 is marked in blue.

4.3.2.1 Pure component adsorption isotherms

Simulated pure component adsorption isotherms of xylene isomers in IRMOF-1, IRMOF-3 and IRMOF-7 are shown in Figure 4-11. In IRMOF-1, xylenes start to adsorb at ~ 10 Pa. In IRMOF-3, the adsorption occurs at lower pressures at around 4 Pa which is due to the smaller pore size and therefore stronger interaction of the xylene molecules with the amino functionalised linkers. In comparison to IRMOF-3, in IRMOF-7, xylenes start filling the pores at lower pressures of slightly above 1 Pa. This is due to stronger adsorption strength with IRMOF-7's NDC linkers and its smaller pore size.

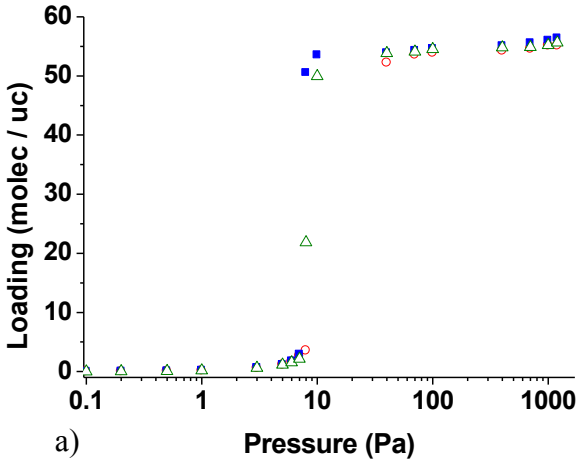

a)

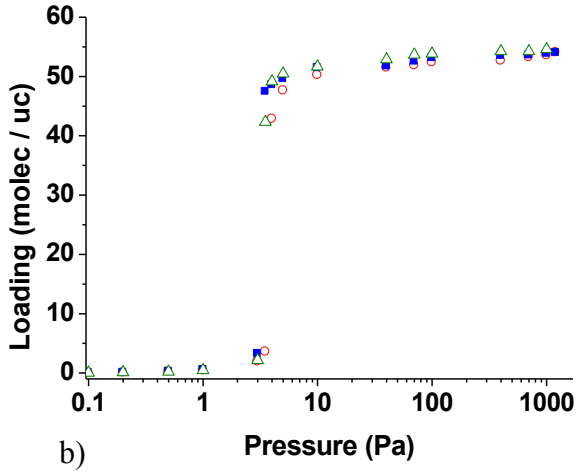

b)

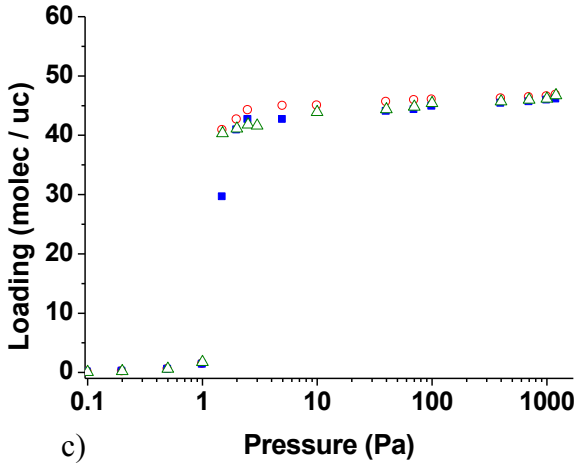

c)

Figure 4-11: Single component adsorption isotherms for xylene isomers in a) IRMOF-1, b) IRMOF-3 and c) IRMOF-7. pX (open circles), oX (closed squares) and mX (open triangles).

As it can be seen from the isotherms, the amount adsorbed for all xylene isomers are rather similar throughout the entire isotherms for these three MOFs. In IRMOF-1 and IRMOF-3, oX fills the pores first but the isotherms level off at higher pressures. Only in IRMOF-7 marginally stronger affinity for pX was observed in the pressure range of 2-100 Pa but again at high loadings the amount adsorbed is very similar. These results indicate that the order of preferential adsorption is not related to better packing arrangements of a specific xylene at high pore filling.

4.3.2.2 Mixture adsorption simulations

Figure 4-12, compares the selectivities for equimolar mixtures of pX/mX and pX/oX at different loadings for the IRMOFs studied. In IRMOF-1, almost no preference was observed for the pX/mX binary mixture at different loadings. The lack of preference towards either xylenes in IRMOF-1 is in agreement with four component (EB, pX, mX and oX) vapor-phase breakthrough experiments reported by Gu *et al.* (2009) where xylene isomers were eluted at the same time at 250 °C and pre-column pressure of 120 kPa. At very low pressure in the Henry region (1 Pa), where the molecules are adsorbed close to the framework and xylene-framework interactions dominate, the selectivity is nearly 1 for all mixtures meaning that all xylene isomers interact with the framework in a similar way. At higher loadings adsorbate-adsorbate interactions play a more important role in selective adsorption but again the large pores are unable to induce significant confinement effects. For this reason, packing effects are insignificant and the selectivity remains close to 1 even at high loadings.

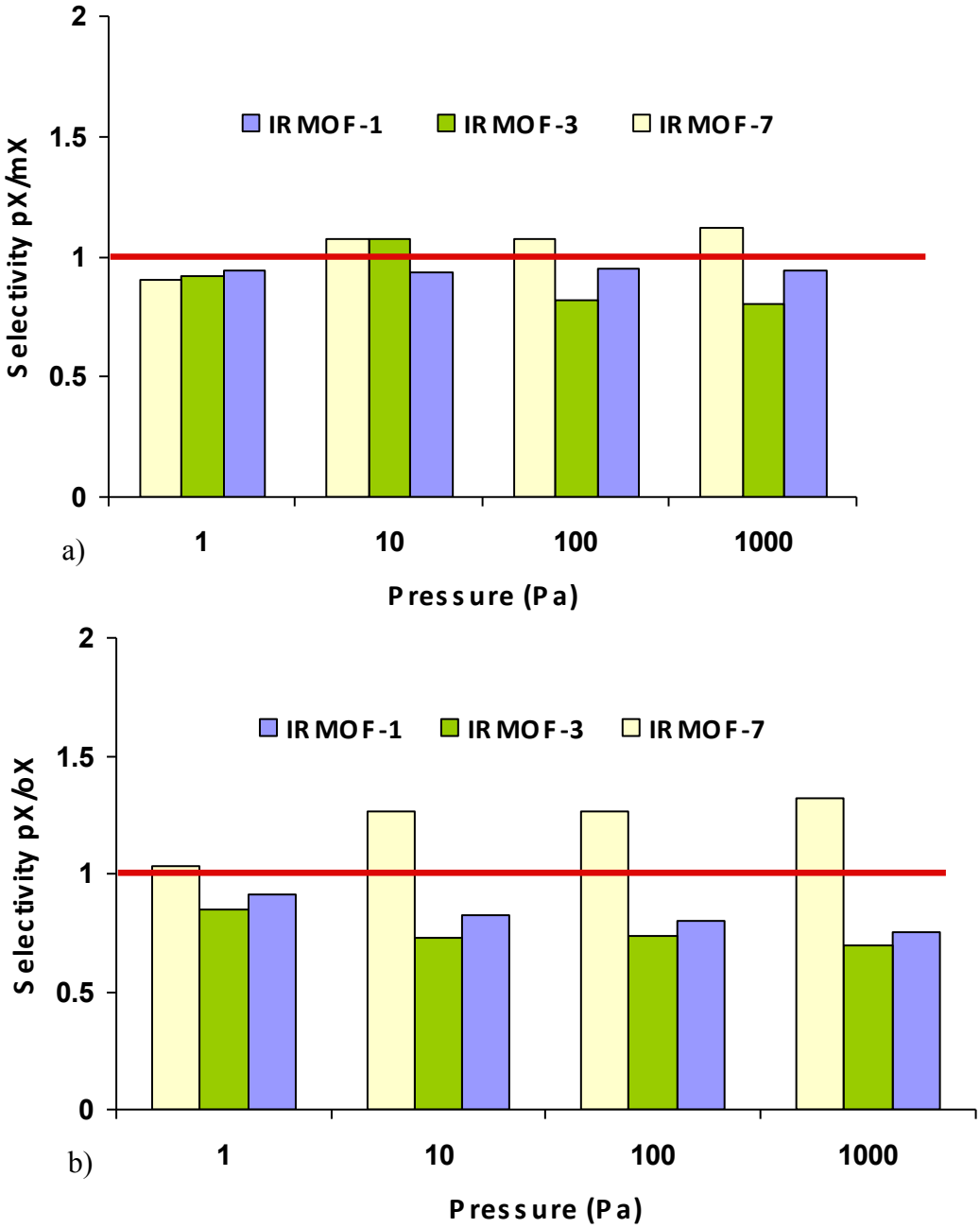

Figure 4-12: a) pX/mX and b) pX/oX equimolar selectivities in IRMOF-1, IRMOF-3 and IRMOF-7 at different pressures and 300 K.

IRMOF-3 is a bit more oX selective with average selectivities of 0.75 for the separation of pX/oX mixture at different pressures. This rather larger preference for oX seems to arise from higher interaction energies between oX-oX molecules compared to the ones of pX-pX. This is illustrated in Figure 4-13 where the interaction energies are broken down into xylene-framework and xylene-xylene for a

mixture of pX/oX. The energy difference between oX-oX and pX-pX is higher than the ones seen for xylene / IRMOF-1 hence the oX preference is slightly higher. The interaction energies are higher for the functionalized IRMOFs, IRMOF-3 and IRMOF-7, but both pX and oX interact similarly with the different IRMOF frameworks with energy differences of 0.5-1 kJ/mol. However, the adsorbate-adsorbate interaction energies become a dominant factor in favour of oX with a 4-5 kJ/mol difference between the two isomers in IRMOF-1 and IRMOF-3.

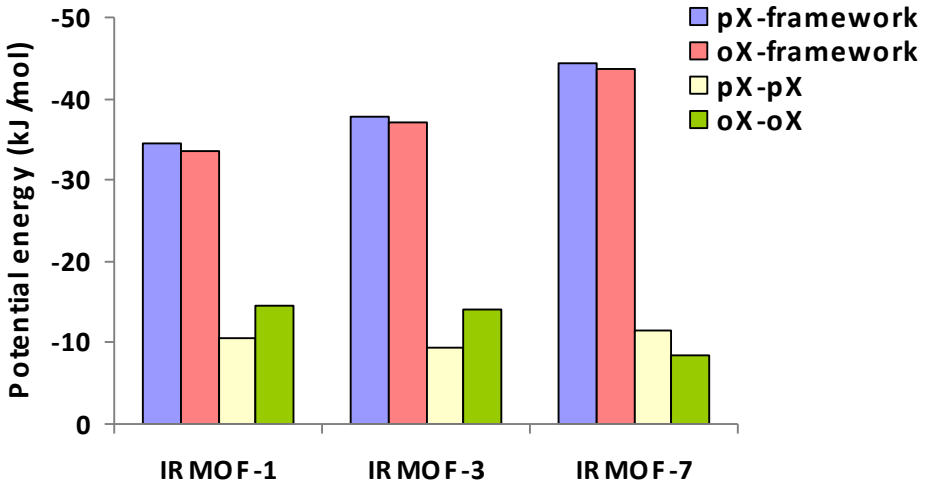

Figure 4-13: adsorbate-adsorbate and adsorbate-framework potential energy interactions for IRMOF-1, IRMOF-3 an dIRMOF-7 for an equimolar mixture of pX/oX at 1 kPa and 300 K.

In contrast to IRMOF-1 and IRMOF-3, IRMOF-7 demonstrates better pX selectivity in pX/oX mixture although the selectivity for a mixture of pX/mX is almost negligible. Even though little difference in adsorption capacity of pure component xylene isotherms was observed, in the case of pX/oX mixtures, IRMOF-7 shows a preferable adsorption for pX over the other isomers as shown in Figure 4-12. The interaction energy for pX-pX is 3 kJ/mol higher than that of oX-oX (see Figure 4-13). pX-framework interactions are higher by less than 1 kJ/mol that arises from the Coulombic interactions with the framework atoms. Simulation snapshot for a mixture of pX/oX reveal that pX molecules are sitting in the positions corresponding to high energetic interactions allowing better vdW interactions with each other and the framework. As shown in Figure 4-14 these positions are located in the narrow rectangular shaped windows of IRMOF-7 created by the naphthalene rings (see

Figure 4-10). This window is less attractive for oX and to some extent for mX as they have larger waist diameters.

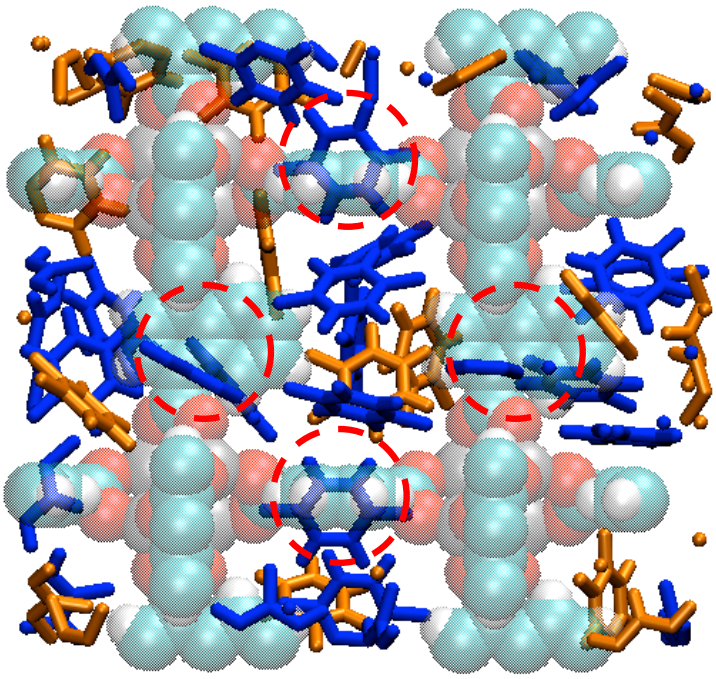

Figure 4-14: Snapshot of a 50/50 mixture of pX (blue) and oX (orange) in IRMOF-7 at 1 kPa and 300 K. The framework is shown in vdW representation. The preferred locations of pX in the windows are marked by dashed circles.

To obtain more details about the interaction between the frameworks and the xylenes molecules, the influence of electrostatic interactions on selectivity was also studied by switching off the fluid / framework Coulombic interactions. Repetition of the simulations at 1 kPa and 300 K showed a general decrease in selectivity towards oX in IRMOF-1 and IRMOF-3 and in the case of IRMOF-7 towards pX for all mixtures studied. This decrease is more prominent for the functionalised IRMOF-3 and IRMOF-7 and no significant effect was observed for IRMOF-1. In IRMOF-1 the selectivity for pX/mX and pX/oX decreased by an average of only 4 % whereas in the case of IRMOF-3 and IRMOF-7, 17 % and 14 % reductions were seen respectively.

The results so far demonstrate that although the functionalised IRMOFs studied exhibit a mild preference towards a specific xylene isomer depending on their linker the large pores in these MOFs are again too large to provide a sterically confined environment or exhibit molecular sieving properties. Therefore, xylene molecules occupy a large number of favourable positions in the frameworks resulting in low selectivity values.

4.4 o-xylene selective MOFs (6 Å < d < 8.5 Å)

MOFs with medium pore diameters (i.e 6 Å < d < 8.5 Å) were also examined for their xylene separation capability. Here, MIL-53 is discussed in detail. MIL-53 (Serre *et al.* (2002)) is a highly flexible framework and consists of one-dimensional diamond shaped channels with a diameter of 8.5 Å in its open conformation (Figure 4-15). The channels are formed by infinite chains of coordinated metals with terephthalate and OH groups i.e. $XO_4(OH)_2$ with X=Al, Cr, Fe, Ga. These channels are not interconnected.

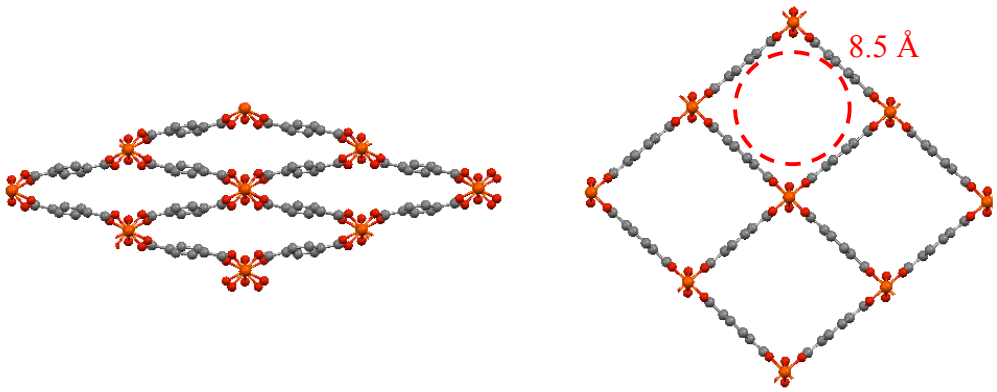

Figure 4-15: View of the MIL-53 channels at room temperature closed form (left) and the open form (right).

Here, only the Al open form of MIL-53 is studied and the framework is considered to have a perfect rigid lattice. This assumption is considered to be reasonable for the purpose of this screening study as the adsorption capacity and selectivity comparisons are discussed mainly at saturation loadings where MIL-53 exhibits its open structure. The single component adsorption isotherms for xylenes are shown in

Figure 4-16. The amount adsorbed of oX is higher throughout the entire isotherm and maximum amount adsorbed is 3.12 molec/uc while the maximum amount adsorbed for pX and mX is 3.06 and 3 molec/uc, respectively.

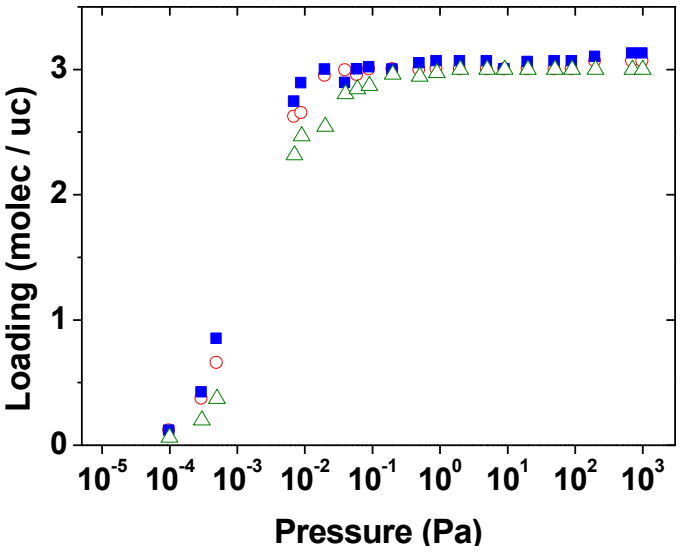

Figure 4-16: Pure component adsorption isotherms for xylene isomers in MIL-53(Al) at 300 K. pX (open circles), oX (closed squares) and mX (open triangles).

The simulation predictions agree well with the order of xylenes adsorbed (oX > pX and mX) in MIL-53 experimentally. These experiments were carried out in gas phase and batch liquid phase adsorption by Finsy *et al.* (2009) and Alaerts *et al.* (2008) at 383 and 300 K respectively. There is also a very good agreement between the saturation capacities obtained from simulations and the above gas phase experiments with maximum capacities of 3.3 (sim. 3.12), 2.95 (sim. 3.06) and 3.0 (sim. 3.0) molec/uc for oX, pX and mX, respectively (Finsy *et al.* (2009)).

It should be noted that in the gas phase experiments, the MIL-53 framework changes its phase from the closed form at low loading to the open form at high loading whereas in our simulations, only the open form of MIL-53 is studied and the framework atoms are fixed at their crystallographic positions. Therefore the effects of framework flexibility are not accounted for in the simulations. The framework

flexibility also provides an explanation why the simulated saturation values for oX are slightly underpredicted: Alaerts *et al.* (2008) observed experimentally that oX isomers distort MIL-53 to a greater extent than mX at saturation uptake. In agreement with the experimental findings, the xylene-framework interaction energies shown in Table 4-1 are larger for oX.

Table 4-1: Interaction energies for equimolar xylene mixtures of oX/mX and oX/pX at 1 kPa and 300 K in MIL-53.

	Potential energy (kJ/mol)			
	oX	mX	oX	pX
adsorbate-adsorbate	-9.95	-3.3	-8.06	-5.42
adsorbate-framework	-73.64	-71.93	-73.37	-72.59

In the competitive adsorption simulations, oX/mX showed the highest oX selectivity value of 3.6 at 1 kPa and 300 K. This selectivity value is much higher than those seen for MOFs with large pores shown in the previous section with average selectivities of 1-1.5. oX is also preferred in the oX/pX mixture with a selectivity of 1.63. The selectivity observed in favour of oX is not caused by shape-selective effects in the MIL-53 channels as oX has not the smallest dimensions of the xylene isomers (see Figure 4-1). The adsorption preference was found to be driven by both energetic and steric effects. From the energy values broken down into adsorbate-adsorbate and adsorbate-framework energies in Table 4-1, it can be seen that the oX-MIL-53 interactions are larger by 1-2 kJ/mol than the mX- and pX-MIL53 interactions. Similar to larger MOFs presented in the previous section, but more prominent, the difference in the adsorbate-adsorbate interactions between oX and mX becomes more evident. oX-oX interactions are larger by 6.5 kJ/mol compared to mX-mX interactions in the mixture. This higher interaction energy shows that oX molecules are able to interact more strongly with each other thus enhancing the selectivity.

The snapshots presented in Figure 4-17: show that at maximum loading two conformations can be found for oX. In the first conformation, oX molecules are stacked together in two rows parallel to the channel with a slight angle with the pore

walls. In the other conformation, both methyl groups in oX are facing towards the framework's carboxylate linker and can interact with it. In contrast to this in pX the molecules are arranged in such a way that their methyl groups are facing the metal clusters. mX are located parallel to the walls with no perpendicular conformations. This also explains the experimental observation that mX has lower interaction with the framework and does not distort the framework as much as oX. The distance between xylene molecules was calculated to be smaller for oXs (7.5±0.72 Å) than for mX (8.76±0.7 Å) and pX (8.9±0.8 Å). This indicates that oX molecules can pack more efficiently within the highly confined channels of MIL-53. Furthermore, the packing effects also explain the increase in oX selectivity in the oX/pX mixture from 1.17 at 0.001 Pa to 1.64 at 1000 Pa as the channel confinement plays a beneficial role for the adsorption entropy by allowing oX to adopt a larger number of favourable configurations in the adsorbed phase.

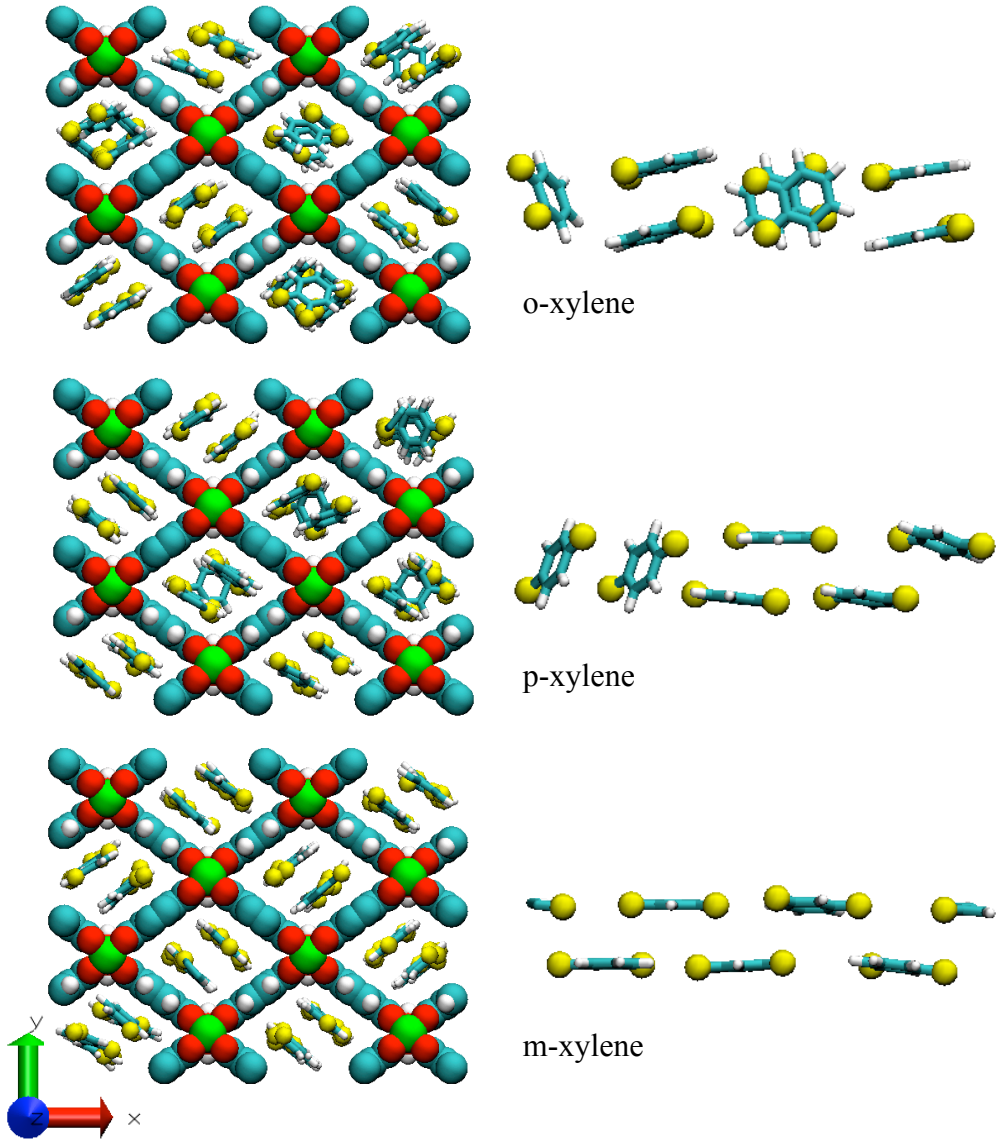

Figure 4-17: Single component adsorption snapshots at high loading and 300 K in MIL-53 for oX, pX and mX.

In order to investigate the influence of Coulombic interactions on the selectivity, mixture simulations were repeated, once with the xylene-xylene and once with the xylene-framework Coulombic interactions switched off. Allowing the Coulombic interaction between only the framework and xylenes but not between the xylene molecules led to an increase in selectivity for oX/pX from 1.64 to 1.92 and more considerably for the oX/mX mixture from 3.6 to 6.2. This indicates that the

electrostatic interactions hinder the oX molecules to get closer to each other leading to a lower selectivity value. On the other hand, neglecting the electrostatic interaction between the framework and xylenes but not between the xylene molecules, results in a minor decrease in the selectivity (i.e. from 3.6 to 3.45 for the oX/mX mixture and from 1.64 to 1.58 for oX/pX mixture). This suggests that Coulombic interactions with the framework slightly favours oX. Although the contribution from the electrostatic interaction is much lower compared with the vdW interactions, the Coulombic interaction energy for oX (-1.12 kJ/mol) is approximately twice as large as for mX and pX. In both cases, the total amount adsorbed is increased when the electrostatic interactions are switched off. This increase is more pronounced for oX meaning that they can pack more efficiently inside MIL-53 channels.

A rather similar trend of oX affinity was observed for another MOF with diamond-shaped one-dimensional channels: MIL-47 (Barthelet *et al.* (2002)). With a pore diameter of 7.5 Å, the channels in MIL-47 are about 1 Å smaller than in MIL-53. This structure was studied in great detail both experimentally and computationally by Alaerts *et al.* (2008), Finsy *et al.* (2009) and Castillo *et al.* (2009), Ghysels *et al.* (2012) respectively. It was found that oX molecules can stack better together in the more sterically confining channels of MIL-47 resulting in high oX selectivities at high loading. The reader is referred to the above references for more details.

4.5 p-xylene selective MOFs (4.2 Å < d < 5.5 Å)

From the screening process, a number of MOFs with a pore size range of 4.2 Å – 5.5 Å emerged as potential candidates for pX selectivity. These MOFs show pX selectivity as their channels are accessible to para-xylene but not to oX or mX depending on the pore topology. In this section, the most promising pX selective MOFs namely MIL-68, MIL-125 and cobalt oxalate MOF are discussed in detail.

4.5.1 MIL-68

MIL-68 (V) (Barthelet *et al.* (2004)) is built from infinite chains of vanadium octahedral metal clusters connected to each other through 1,4-benzenedicarboxlyate (terephthalate) ligands. This network forms two distinct, one-dimensional hexagonal and triangular channels with 13.5 Å and 4.7 Å diameters respectively as shown in Figure 4-18.

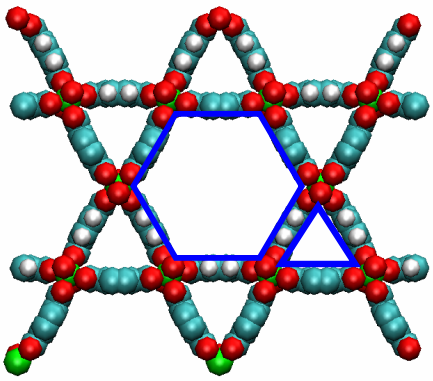

Figure 4-18: The structure of MIL-68 (V) showing large hexagonal and small triangular channels.

Simulated adsorption isotherms of pure xylene isomers in MIL-68 are shown in Figure 4-19. The adsorption of all three xylenes is rather similar up to 10 Pa as the adsorption occurs mainly in the large pores. At higher pressures, pX adsorbs more strongly; and near saturation, mX adsorption shows the same uptake as pX while the amount adsorbed of oX at high loadings is approximately 2 molec/uc.

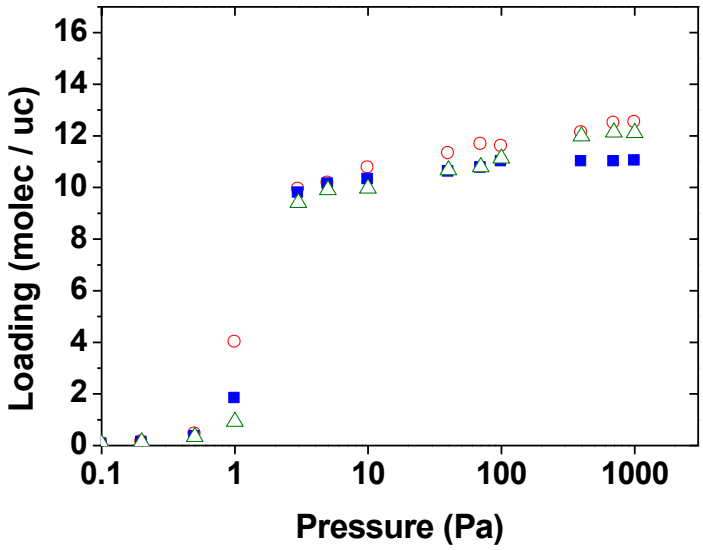

Figure 4-19: Pure component adsorption isotherms of pX (open circles), oX (closed squares) and mX (open triangles) in MIL-68 at 300 K.

The analysis of the adsorption snapshots shown in Figure 4-20 for pure component xylenes at high loadings shows that while the large hexagonal pores are first filled, only pX and mX are adsorbed in the small triangular pores and oX is excluded due to its larger waist diameter. Figure 4-21 shows that pX and mX adsorbed differently in the small triangular pores: in the case of pX, the molecules are located parallel to the benzene rings of the small pore with the methyl groups positions alongside the 1-D channels as they have the smallest waist diameter. For mX, the 1,3-conformation of the methyl groups causes the molecules to rotate ~ 90 degrees and the methyl groups are positioned close to the benzene rings of the linkers with the rest of the molecule pointing towards the channel corner.

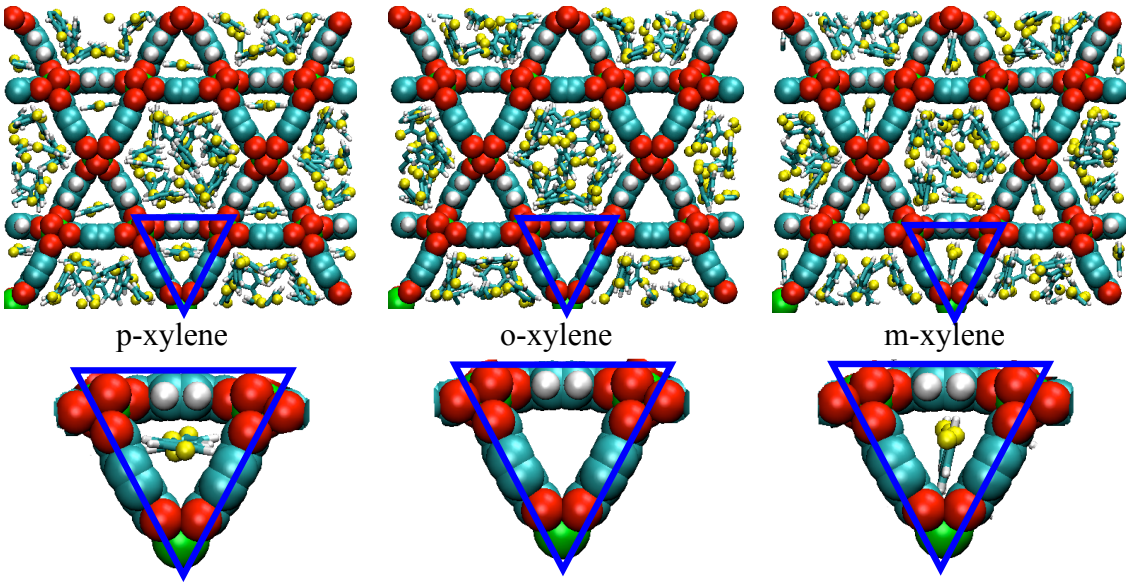

Figure 4-20: Snapshots of single component adsorption of pX (left), oX (middle) and mX (right) in MIL-68 at 300 K and 1 kPa. Methyl groups are shown in yellow. Note that o-xylene cannot access the smaller triangular channels.

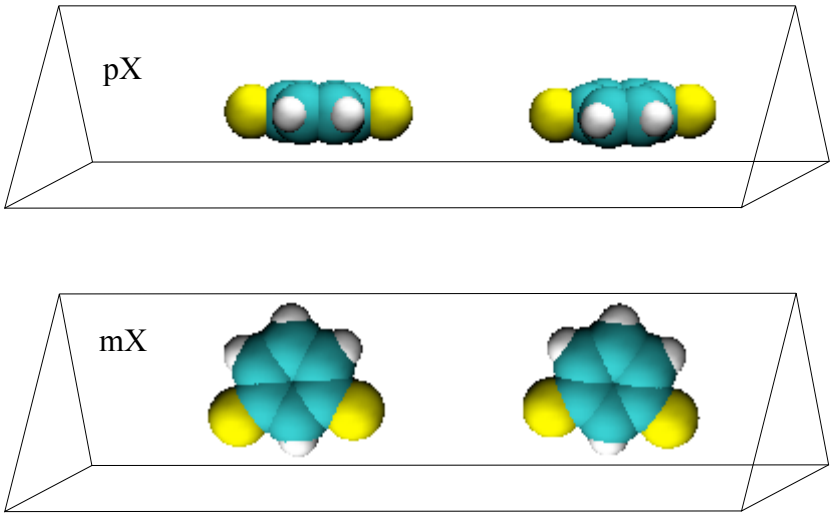

Figure 4-21: Side view of pX and mX arrangement in small triangular channels of MIL-68.

As shown above, only pX and mX fit inside the triangular channels while oX is excluded. However, one has to keep in mind that the LJ parameters in force fields such as UFF were not specifically developed for MOFs. In order to probe the sensitivity of the molecular sieving effect on slightly increased channel size, the hard sphere diameter of the LJ potential of the framework atoms was reduced by 10 %.

This also provides a crude way to assess the influence of framework flexibility due to slight rearrangement of the linkers upon adsorption (as opposed to the large breathing flexibility observed in MIL-53). The simulations repeated at high loading showed that even at high pressure and after further reduction of the hard sphere diameters of the framework atoms by 10%, no oX molecules were observed in the small channels.

The equimolar mixture simulations confirm the trend observed from the single component isotherms and show preferential adsorption of pX. The selectivities for pX/oX and pX/mX mixtures are ~1.1-1.2 in the Henry region (1 Pa) where xylenes are only adsorbed in the hexagonal channels. pX selectivity increases to ~ 1.4 at higher loading (1 kPa) as triangular pores get preferentially occupied by pX molecules. The selectivity values are relatively small as the contribution of the triangular small pores to the total amount adsorbed is very low compared to the larger hexagonal pores. Furthermore, as explained in the previous section the hexagonal pores in MIL-68 are too large to allow significant preferential adsorption of one xylene isomer over the other. This is important because experimental synthesis of MIL-68 is not always straightforward as it is difficult to fully activate the small triangular pores making them inaccessible to xylenes. Therefore, in these conditions, the contribution of only large pores to the adsorption process should be considered (Yang *et al.* (2012)).

4.5.2 MIL-125

MIL-125 comprises two different pores: larger octahedral pores and smaller tetrahedral pores that are connected through triangular windows (Figure 4-22a). These pores are formed from cyclic octamers of $TiO_5(OH)$ connected with terephthalate linkers (Dan-Hardi *et al.* (2009)). The large octahedral pores and the small tetrahedral pore have accessible diameters of 11.8 Å and 5.5 Å, respectively. Amino-functionalisation of the benzene linker yields MIL-125-NH_2 (Figure 4-22b and d). As shown in the pore size distribution in Figure 4-22c, due to the protrusion

of the amino groups in the pore space, both the small and the large pores in MIL-125-NH_2 are about 1 Å smaller than in MIL-125.

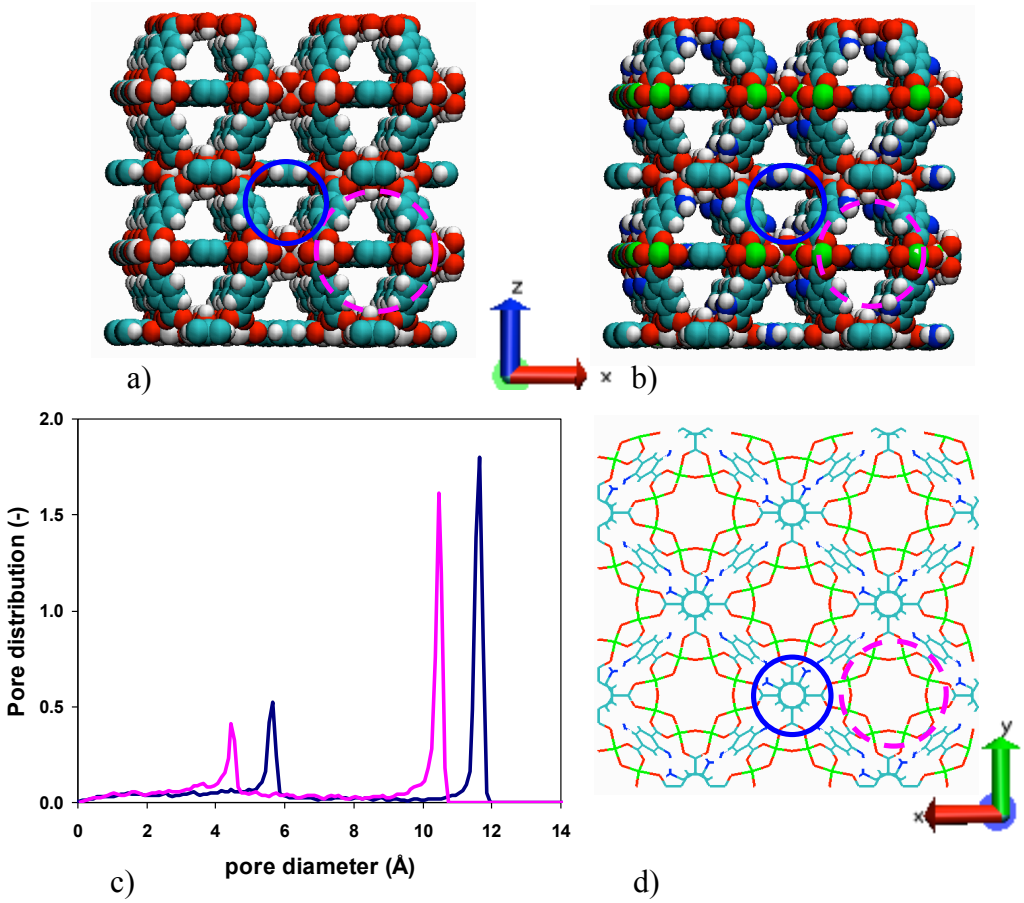

Figure 4-22: a) vdW representation of MIL-125 and its functionalised form b) MIL-125-NH_2. The large octahedral pores and the small tetrahedral pores are shown in dashed pink and solid blue respectively. c) Pore size distribution for MIL-125-NH_2 (pink) is about 1 Å smaller than in MIL-125 (blue). d) stick representation of MIL-125-NH_2.

4.5.2.1 Pure component adsorption isotherms

GCMC simulations of pure component adsorption of xylene isomers in both MIL-125 and its functionalised form were performed at 300 K. As shown in Figure 4-23a, in MIL-125, pX molecules adsorb more strongly at lower pressures followed by oX and mX whereas at higher pressures all three isomers show rather similar loadings.

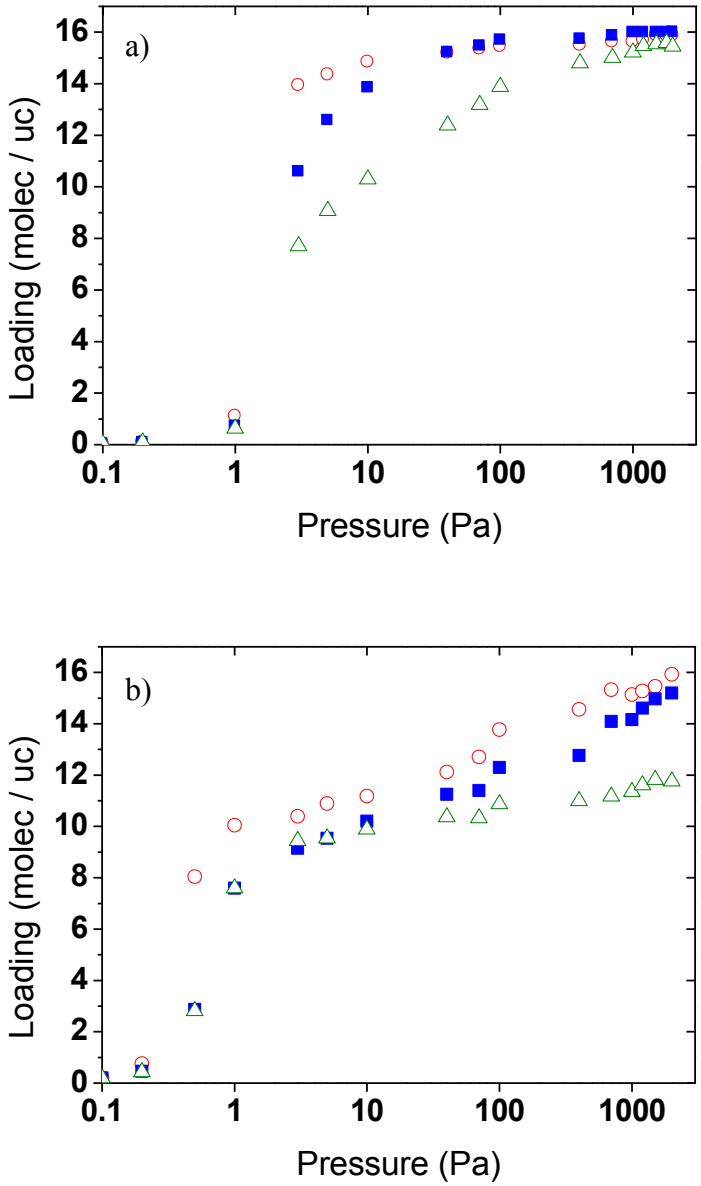

Figure 4-23: Pure component isotherms for pX (open circles), oX (closed squares) and mX (open triangles) in a) MIL-125 and b) MIL-125-NH_2 at 300 K.

To examine the impact of functionalisation, the calculations for the pure component adsorption isotherms were repeated for the amino-functionalised form of the structure, MIL-125-NH_2. At lower pressures the uptake of oX and to a much higher extent of mX are lower in MIL-125-NH_2. Figure 4-23b shows that, similar to MIL-125 but more prominent, pX adsorbs at lower pressure and shows a higher uptake throughout the whole isotherm compared to oX and mX. Interestingly, compared to

MIL-125, the maximum uptake of oX and specifically mX is much lower in MIL-125-NH_2 and these values are lower than those of pX. Compared to MIL-125, in the functionalised form all three isomers start filling the pores at lower pressures due to higher interaction energies between xylene molecules and the large octahedral pores. In order to understand better the role of the tetrahedral and the octahedral pores in adsorption, the breakdown of pure component xylene isomers for the small tetrahedral and the large octahedral pores is given in Figure 4-24.

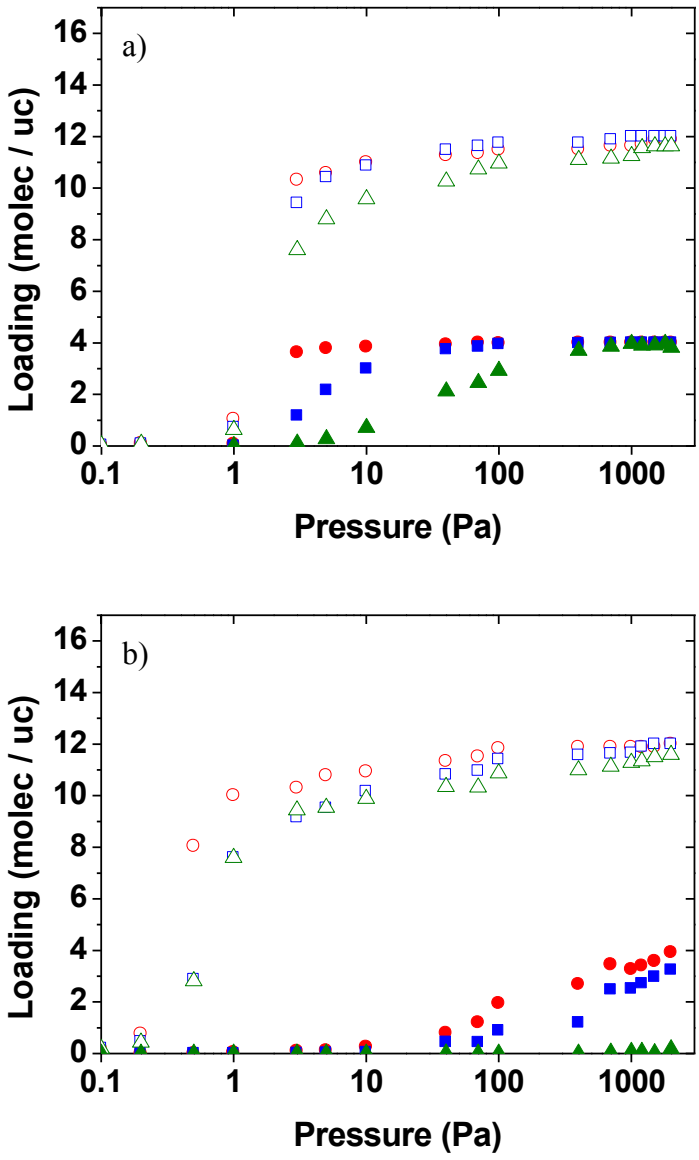

Figure 4-24: Pure component adsorption isotherms for pX (circles), oX (squares) and mX (triangles) at 300 K in a) MIL-125 and b) MIL-125-NH_2 split into adsorption in the large octahedral pores (open symbols) and small tetrahedral pores (closed symbols).

As it can be seen, in both structures, at lower pressures, only pX and to a lower extent oX enter the small tetrahedral pores. mX occupies the small pores only at high pressures in MIL-125 and in the case of MIL-125-NH_2 hardly any mX enters these pores. The values for the maximum loading shows that the adsorption capacity in the octahedral and tetrahedral pores does not differ significantly for the isomers in MIL-125 whereas in the amino functionalised structure pX adsorbs more strongly over the whole pressure range in both tetrahedral and octahedral cages particularly at low pressures.

In order to explain the difference in the amount adsorbed, representative simulation snapshots are given in Figure 4-25 to Figure 4-27 comparing pure component mX, oX and pX adsorption in MIL-125 and MIL-125-NH_2 at 1 kPa and 300 K. In agreement with the adsorption isotherms, the snapshot for mX clearly demonstrates that while mX molecules occupy the small pores (marked by the blue circle) in MIL-125 at higher loadings, they are completely excluded from the small tetrahedral pores of MIL-125-NH_2. Therefore, the saturation loading decreases from 15.5 molec/uc in MIL-125 to 12 molec/uc in MIL-125-NH_2.

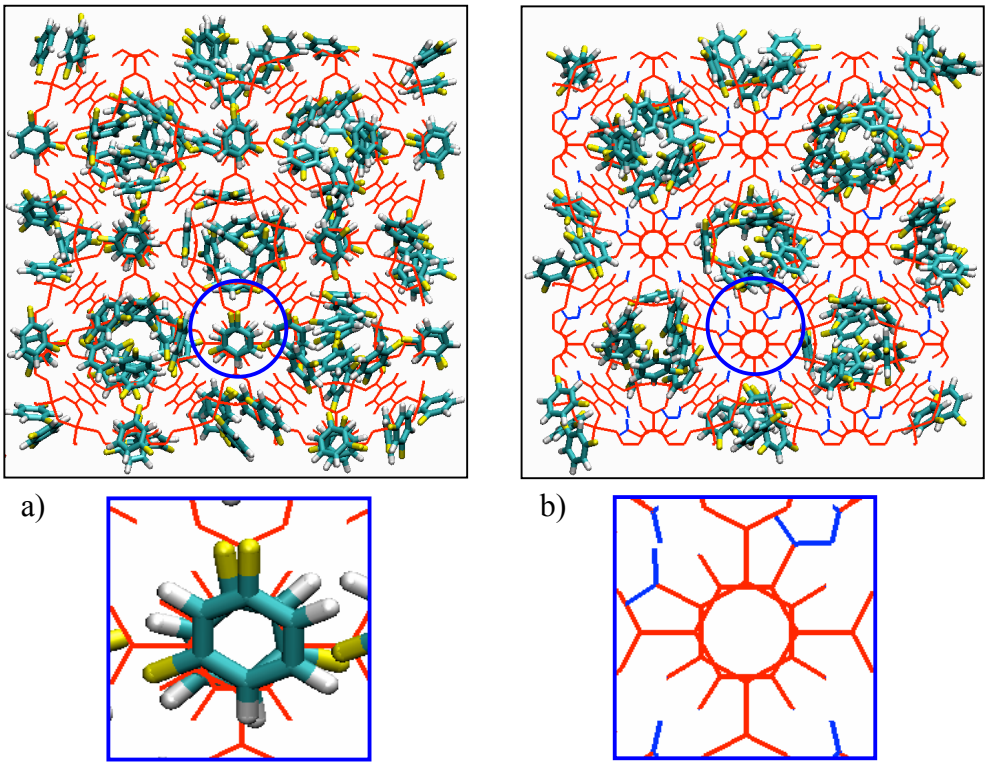

Figure 4-25: Snapshots of single component mX in a) MIL-125 and b) MIL-125-NH_2 at 1 kPa and 300 K. Methyl groups in xylenes are shown in yellow. Small tetrahedral pores are marked with blue circles. The boxes at the bottom are enlargements of the tetrahedral pores.

The snapshots for oX are shown in Figure 4-26. The proportion of oX molecules in the small pores decreases from ~24% to ~12% in the functionalised framework. Additionally, as illustrated by the pink circles the oX molecules are much less ordered in MIL-125-NH_2 and are also no longer adsorbed close to the octahedral pore walls at the windows towards the smaller, tetrahedral pores as was observed for MIL-125. The consequence of this becomes very clear when looking at the pure component adsorption isotherms where oX shows considerably less uptake in MIL-125-NH_2.

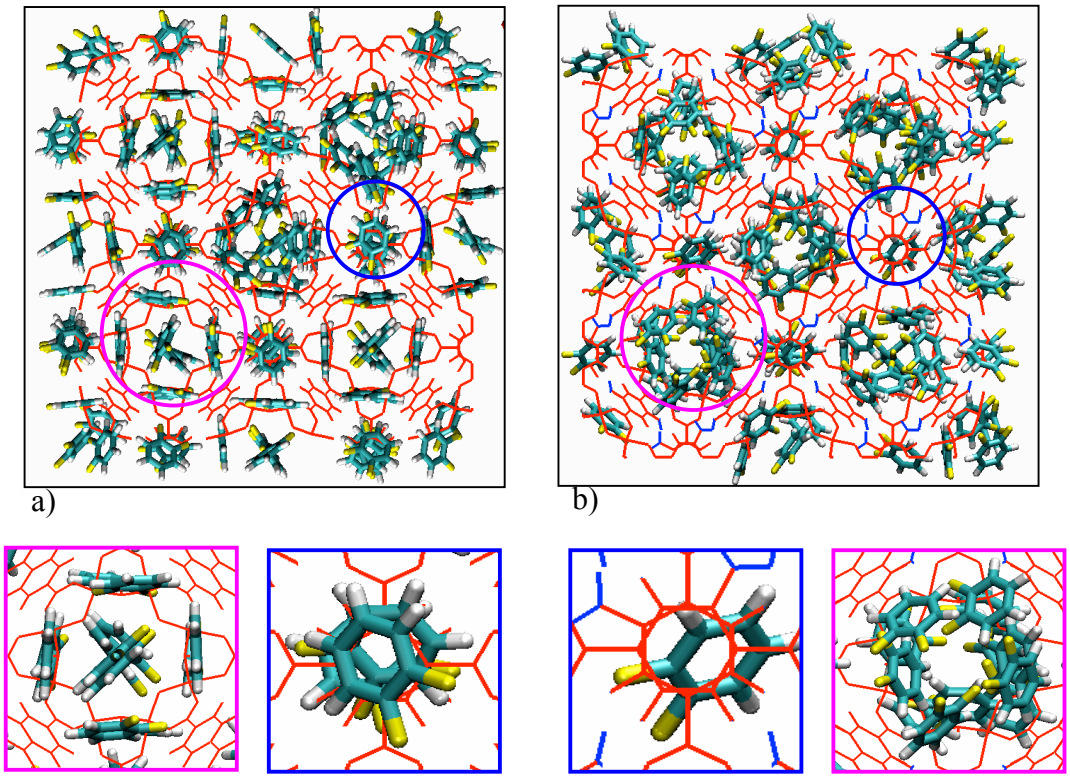

Figure 4-26: Snapshots of single component oX in a) MIL-125 and b) MIL-125-NH_2 at 1 kPa and 300 K. The large octahedral and small tetrahedral pores are marked by pink and blue circles, respectively. The boxes at the bottom show enlargements of the marked pores.

Unlike mX and to some extent oX, in the case of pX, the fraction of molecules occupying the small pore does not change significantly in the functionalised form as pX occupies the tetrahedral pores relatively more easily. Figure 4-27 shows that pX fits tightly in the tetrahedral pores due to its smaller kinetic diameter.

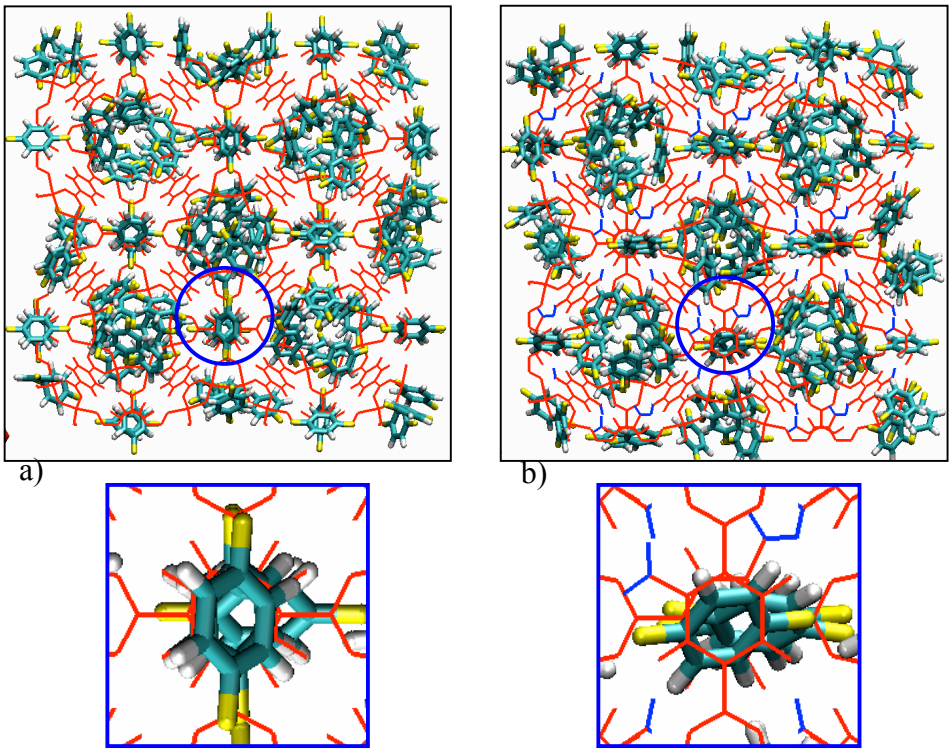

Figure 4-27: Snapshots of single component pX in a) MIL-125 and b) MIL-125-NH_2 at 1 kPa and 300 K. The small tetrahedral pores are marked with blue and the box at the bottom shows an enlargement of the snapshot in this area.

It is worth mentioning that the pore sizes reported earlier are calculated from the biggest spheres that could be inserted in the centre of the pore following the method described by Gelb and Gubbins (1998). However, in reality, the pore shape is more complex. The tetrahedral cages have a cruciform cross section as illustrated in Figure 4-28. This aperture allows for a better fit of pX molecules compared to oX; and mX molecules do not fit inside the pore as illustrated in Figure 4-28. This is why there is an energy penalty for oX to occupy the tetrahedral cages, which is even larger for mX leading to a near complete exclusion of mX from the small pores of MIL-125-NH_2.

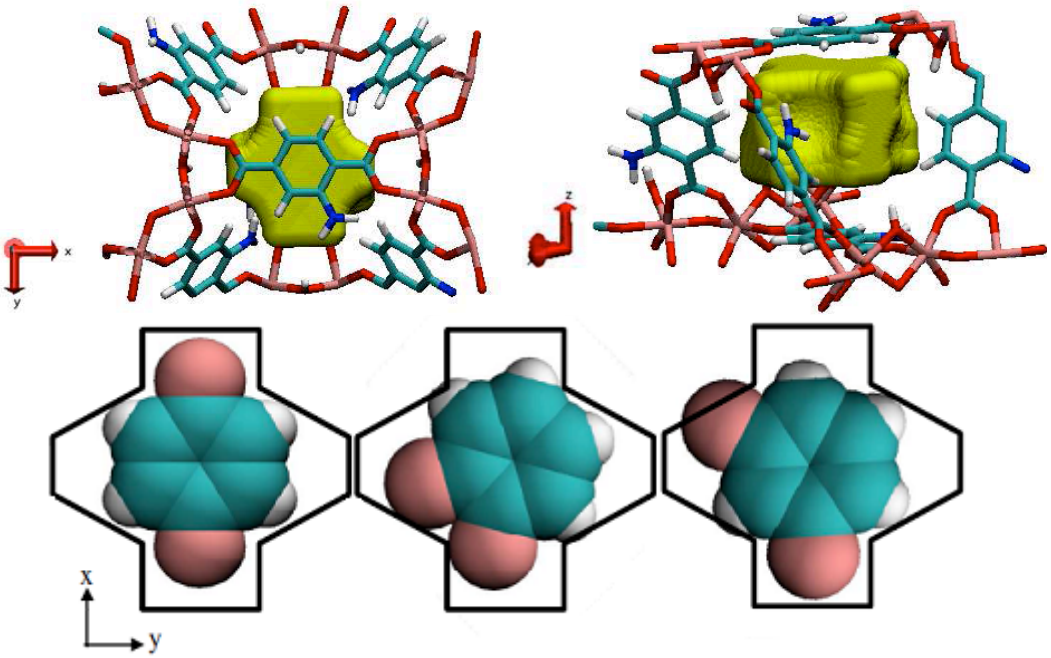

Figure 4-28: Illustration of the pore shape (yellow) in the small tetrahedral pores (top). Schematic illustration of how pX fits easily into the cross-shaped pore space while there is some overlap for oX. mX does not fit into the pore space at all.

4.5.2.2 Influence of the small tetrahedral pores on adsorption

In order to investigate the role of the large octahedral pores on the amount adsorbed and eliminate the effects of xylenes adsorbed in the small pores, the single component simulations in MIL-125 and MIL-125NH_2 were repeated with the small pores blocked. As shown in Figure 4-29a, in MIL-125, pX adsorbs slightly better at low loadings but at around 100 Pa and above, the difference in adsorption is not prominent. In the case of MIL-125-NH_2 (Figure 4-29b) the maximum amount adsorbed for pX decreases by 4 molec/uc from 16 to 12 molec/uc when the small pores no longer contribute to adsorption. The decrease of the maximum amount adsorbed for oX is less pronounced (decrease from 15 to 12 molec/uc) as the small pores are energetically not favourable for these molecules. In the case of mX, the maximum adsorption capacity shows no drop when the small pores are blocked and the saturation capacity remains at ~ 12 molec/uc. This was expected, as mX isomers do not fit into the small pores.

Remarkably, the results indicated that again pX molecules were preferentially adsorbed in the octahedral pores at lower loadings in both structures and even at saturation capacity in MIL-125-NH_2. This finding shows that the preference towards pX originates from both small and large pores and the level of pX preference becomes more significant in MIL-125-NH_2.

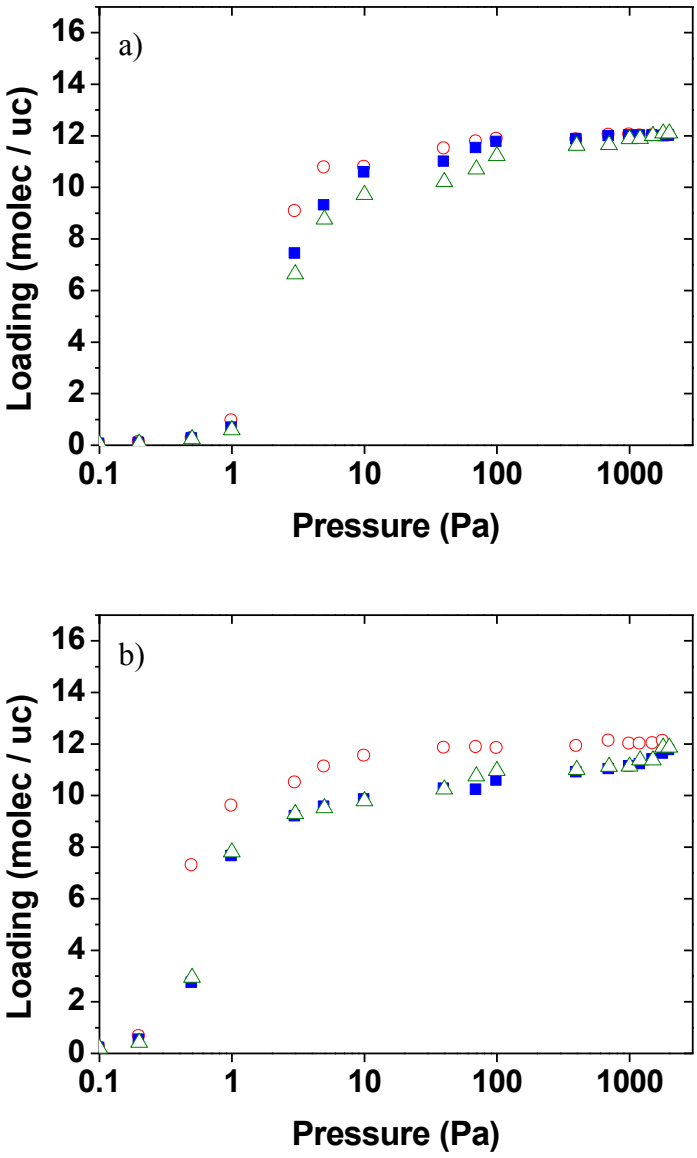

Figure 4-29: Pure component isotherms for pX (open circles), oX (closed squares) and mX (open triangles) in a) MIL-125 and b) MIL-125-NH_2 at 300 K with small pores blocked.

4.5.2.3 Adsorption of xylene mixtures

Figure 4-30 compares the simulated 50/50 binary mixtures isotherms of pX and oX in MIL-125 and MIL-125-NH_2 at 300 K broken down into the amount adsorbed in large and small pores. In both cases, pX is adsorbed preferentially over the entire pressure range. pX molecules have higher interaction energies with the large pore of the framework and are adsorbed first in both structures. The small pores in MIL-125 are 1 Å larger than those of the functionalised form and pX molecules start to fill them at lower pressures as shown by the hatched areas (Figure 4-30). Similar to the results obtained for the pure component isotherm, it is also apparent in the mixture simulations that the small pores in both structures are exclusively filled by pX molecules indicating that there is an energy penalty for both oX and mX to enter the small pores. The para-selectivity of MIL-125 can therefore be explained with the accessibility of the small pores and large pores combined. The small tetrahedral pores in MIL-125-NH_2 get filled with pX molecules at loadings above 10 Pa. Once more, higher interaction energies for pX causes them to pack more efficiently in the large pores of MIL-125-NH_2 resulting in an overall selectivity of 3.4 and 2.84 for pX/mX and pX/oX mixtures at 1 kPa and 300 K as shown in Figure 4-31. These simulation values for the selectivity correspond well with values determined from liquid phase breakthrough experiments which showed selectivities of 3 and 2.2 for pX/mX and pX/oX mixtures (Vermoortele *et al.* (2011)).

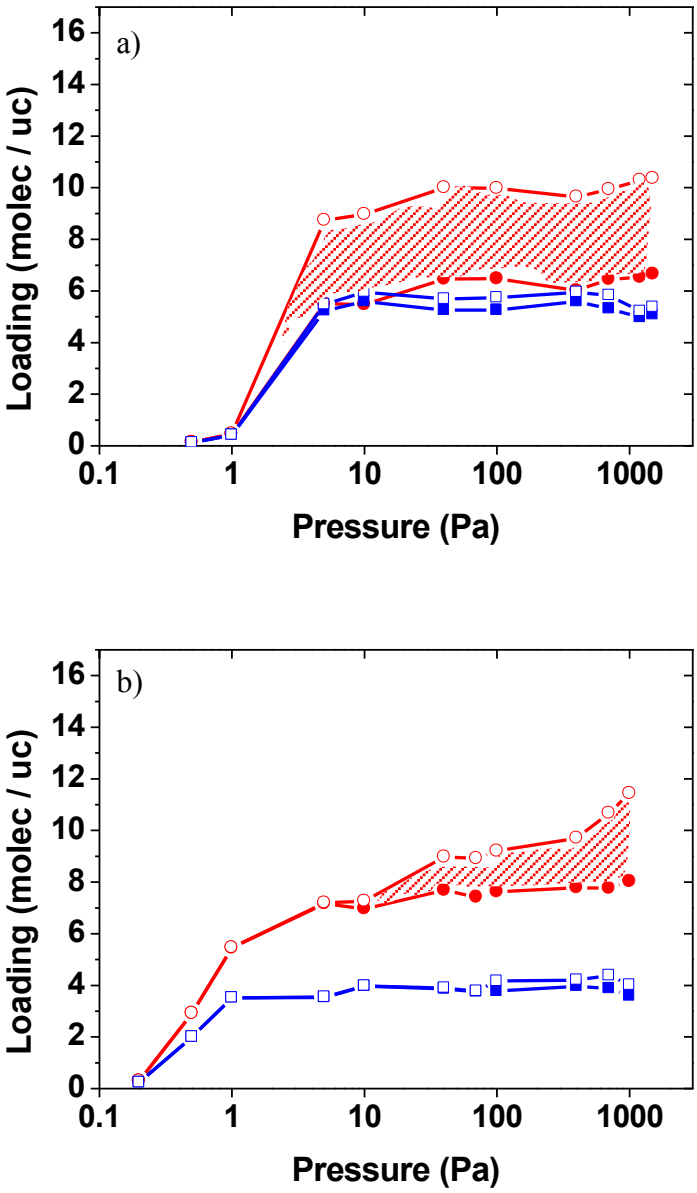

Figure 4-30: Isotherms of 50/50 mixture of pX and oX in a) MIL-125 and b) MIL-125-NH_2. pX (circles) and oX (squares). The open symbols show the total amount adsorbed and the closed ones shows the amount adsorbed in the large pores. The difference between open and closed symbols (hatched area) shows the number of molecules adsorbed in small tetrahedral pores.

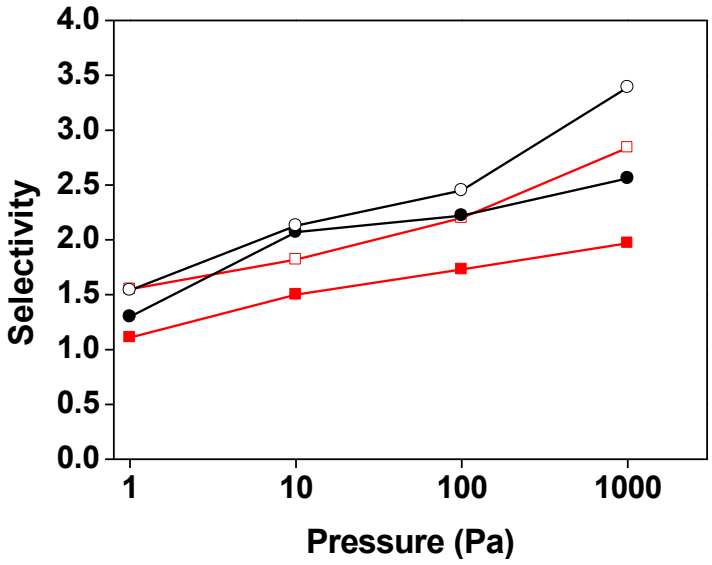

Figure 4-31: Selectivities for 50/50 mixtures of pX/mX (circle) and pX/oX (square) at different loadings for MIL-125 (closed symbols) and MIL-125-NH_2 (open symbols).

As shown in Figure 4-31, the extent of selectivity towards pX increases as the uptake increases in the mixture isotherms in both structures but to a greater extent for MIL-125-NH_2. This indicates that at low loadings (i.e. 1 Pa) where the adsorbate-framework interactions have a dominant impact on preferential adsorption, the selectivity is driven by the higher interactions of pX molecules in the large pores as shown in Figure 4-30b. At loading above 10 Pa, the exclusive presence of pX in the small pores boosts the selectivity specifically in MIL-125-NH_2. For example, at high loadings oX can hardly enter the small pore with only 0.4 molec/uc whereas these pores are preferentially filled with 3.4 molec/uc of pX in the competitive adsorption simulation. This is further illustrated by the blue circles in the snapshots taken from the equimolar mixture of pX and oX in Figure 4-32.

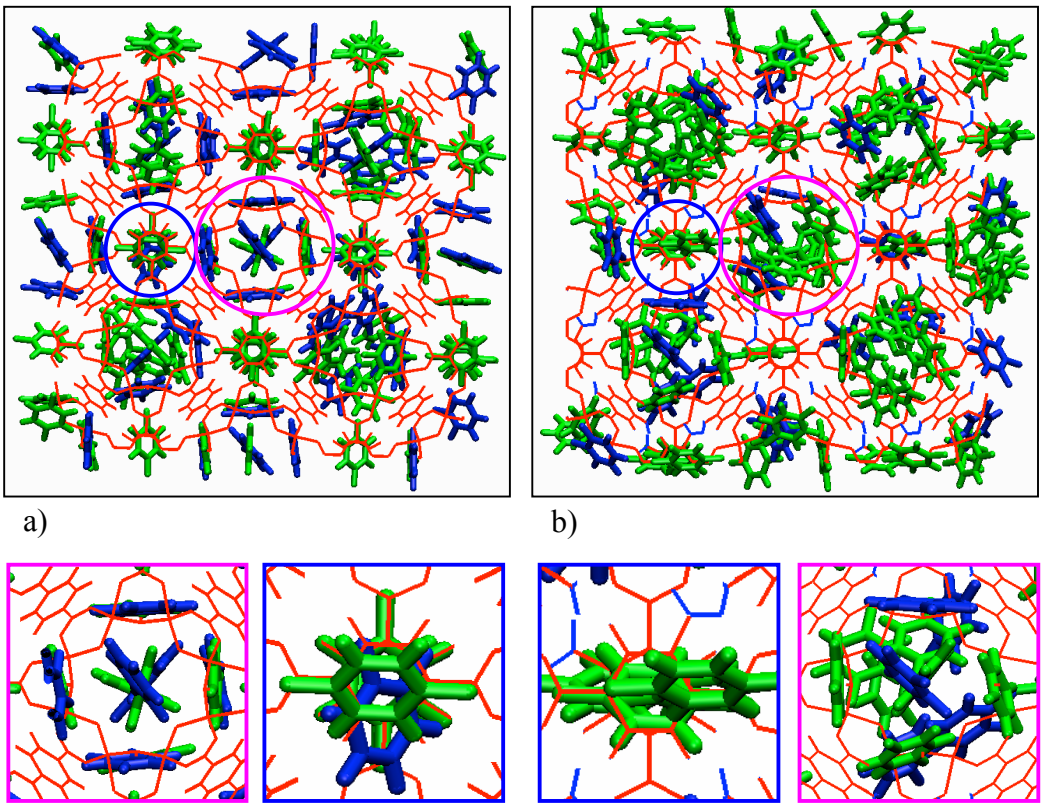

Figure 4-32: Snapshots of 50/50 mixture of pX (green) and oX (blue) in a) MIL-125 and b) MIL-125 -NH_2.

Again similar to the pure component oX adsorption, in MIL-125 oX is located in the four sides of the triangular windows between the small and large pores, but in the functionalised structure both oX and mX molecules are located in the centre of the large pore in a rather disordered way as illustrated in Figure 4-32. As discussed for the single component adsorption isotherms, the adsorption of xylene isomers is energetically less favourable in the tetrahedral pores than the large octahedral pores. This effect is more pronounced in MIL-125-NH_2. The comparison between adsorbate-adsorbate and adsorbate-framework interaction energies for equimolar xylene mixtures of pX-oX and pX-mX shows that not only the pX-pX interaction is larger than for the other isomers, but also it maximises its energy with both frameworks as shown in Table 4-2. This difference is more pronounced in MIL-125-NH_2.

Table 4-2: Interaction energies for equimolar xylene mixtures of pX/oX and pX/mX at 1 kPa and 300 K in MIL-125 and MIL-125-NH_2.

	Potential energy (kJ/mol)			
	pX	oX	pX	mX
MIL-125				
adsorbate-adsorbate	-9.28	-7.97	-10.92	-6.17
adsorbate-framework	-50.76	-46.38	-50.53	-43.76
MIL-125-NH_2				
adsorbate-adsorbate	-18.84	-12.1	-18.95	-11.65
adsorbate-framework	-51.75	-48.3	-51.7	-48.32

4.5.2.4 The importance of electrostatic interactions

One way to understand better the adsorbate-framework interactions is to look at electrostatic and vdW energies separately. To do this, the average potential energies of single xylene isomers were calculated using molecular dynamics simulations in the NVT ensemble at 300 K and the interaction energies were split into vdW and Coulombic interactions. It was found that the presence of the amino groups in MIL-125-NH_2 leads to an average increase of ~ 34 % in Coulombic interactions and ~ 5 % for van der Waals interactions for all xylene isomers as shown in Figure 4-33.

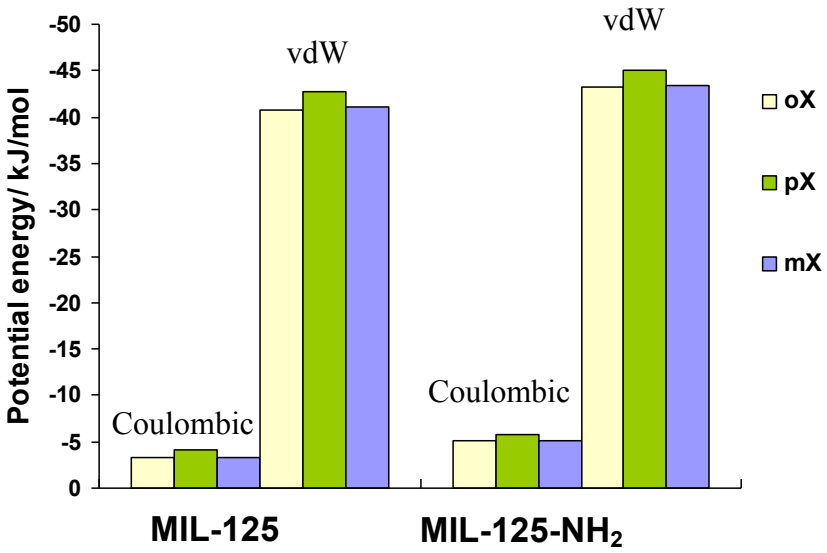

Figure 4-33: Potential energy comparison of xylene isomers in MIL-125 and MIL-125-NH_2 obtained by performing molecular dynamics of one molecule inside the pore.

Overall, pX shows higher vdW and electrostatic interactions with the framework in comparison to oX and mX. Although these calculations provide information regarding general change in the vdW and electrostatic interactions of xylenes in both structures, drawing firm conclusions in terms of electrostatic effects on adsorption requires more study. Thus, as described for other structures in previous sections, the adsorption simulations were repeated by neglecting all Coulombic interactions between adsorbates and framework. Figure 4-34 compares the pure component isotherms for xylenes with and without the Coulombic interactions between adsorbates and MIL-125-NH_2.

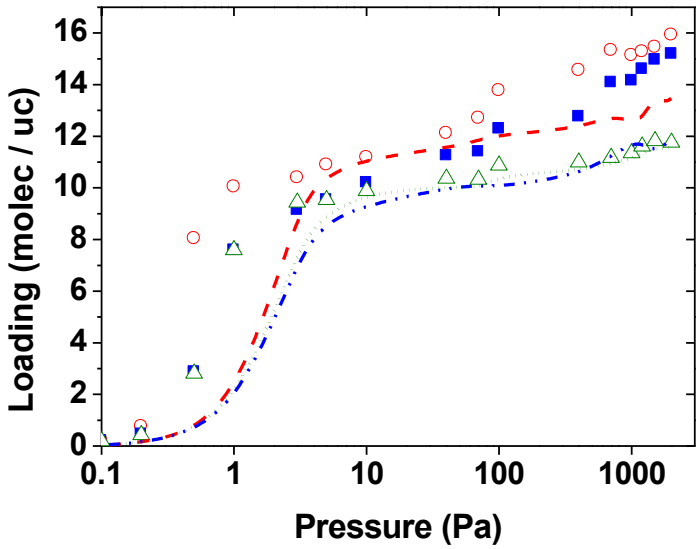

Figure 4-34: Comparison between the single component adsorption isotherms for pX (open circles), oX (closed squares) and mX (open triangles) in MIL-125-NH_2 at 300 K. Isotherms shown as lines represent isotherms where xylene-framework Coulombic interactions are neglected. pX (red dashed), oX (blue dotted dashed) and mX (green dotted).

At low pressure, weaker xylene-framework interactions result in the isotherms to shift towards the right meaning that the xylenes enter the octahedral pores at rather higher pressure. The effects of electrostatic interactions are more significant in the small tetrahedral pores. It can also be seen from Figure 4-34 that since mX molecules do not occupy the small pores, switching the electrostatic interactions off does not significantly affect its adsorption. However, in the case of pX, the lack of

electrostatic interactions lowers significantly the saturation uptake from 4 molec/uc when the Coulombic interactions are included to just 1 molec/uc when the electrostatic interactions are switched off. As the contribution of small pores to adsorption reduces significantly, mixture simulations also show that the pX/oX selectivity drops from 2.84 to 1.85 at 1 kPa and 300 K when the electrostatic interactions of xylenes and the framework atoms are neglected.

4.5.3 Cobalt oxalate MOF

To find out if the pore range found to be pX selective in the MOFs investigated so far is transferable to other MOFs, another framework named cobalt oxalate (Hao *et al.* (2010)) was tested for its xylene selectivity. This MOF comprises two types of channels. The large channel (A) consists of two cobalt clusters and two ligands (Figure 4-35a). Note that the hydroxyl groups on the middle of the wall divide the pore into two channels. Channel (B) is best viewed along the b-axis as presented in Figure 4-35(b). These channels have diameters of 4.3-4.5 and 5.1 Å respectively and are interconnected as shown with the orange aperture in Figure 4-35. For a mixture of pX/oX, this MOF shows selectivity of 5.5 the highest para-selectivtiy for any of the MOFs investigated so far.

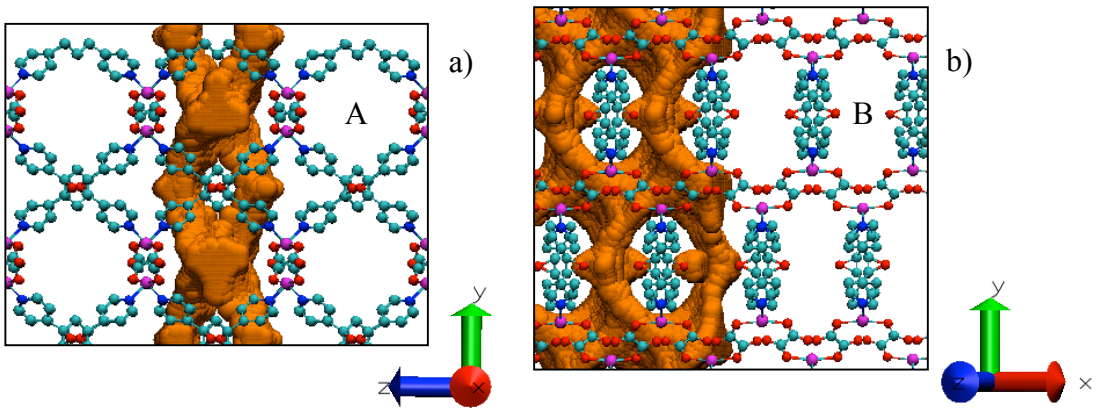

Figure 4-35: The structure of cobalt oxalate MOF when viewed (a) along the a-axis with channels A and (b) along the b-axis with channels B. Co: purple; O: red; N: blue and C: grey. The hydrogens are removed for clarity. Schematic view of the available pore space is shown in orange.

The snapshots at high pressure of the 50/50 pX/oX mixture (Figure 4-36) show that the p-xylene molecules adsorb inside the framework channels in an ordered pattern with pXs preferably adsorbed in both A and B channels. Two energetically favourable positions can be identified for pX molecules. The first location is the empty void in the A channels where pXs are positioned in the centre of the channels with their methyl groups pointing to the opposite linkers (red circle). The second accessible site exclusively occupied by pX molecules is the space between the two linkers where pXs are positioned parallel to each other with one methyl group facing channel A and the other in channel B (dashed green circle).

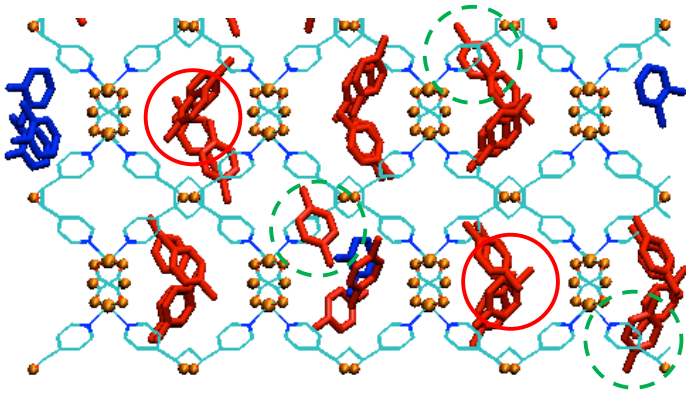

Figure 4-36: Snapshots of 50/50 mixture of pX (red) and oX (blue) in cobalt oxalate MOF. Preferential adsorption of pX in A and B channels are marked in red and dashed green circles, respectively.

It should be noted that these results were achieved without taking electrostatic interactions into account, which will change the results slightly. This MOF also shows a gating effect and it is unclear how this will affect the performance for the separation of xylene mixtures. Despite this, another promising MOF within the range of pX selective pore size MOFs is found that can be targeted by experimental synthesis to investigate its selective performance further.

4.6 MOFs with smaller pores (d < 4 Å)

MOFs comprising of pores with diameters less than ~ 4.0 Å were also tested for xylene isomers separation. These pores are too small to accommodate xylene molecules inside their pores and do not adsorb xylenes. As shown in Figure 4-37, the

three structures tested for xylene adsorption are Sc-BDC (Perles *et al.* (2005), Miller *et al.* (2005)), Cobalt(II)-Glutarate (Won *et al.* (2002)) and $Cu(INA)_2$ (Pichon *et al.* (2006)) with pore diameters of 3.1, 3.9 and 4 Å respectively.

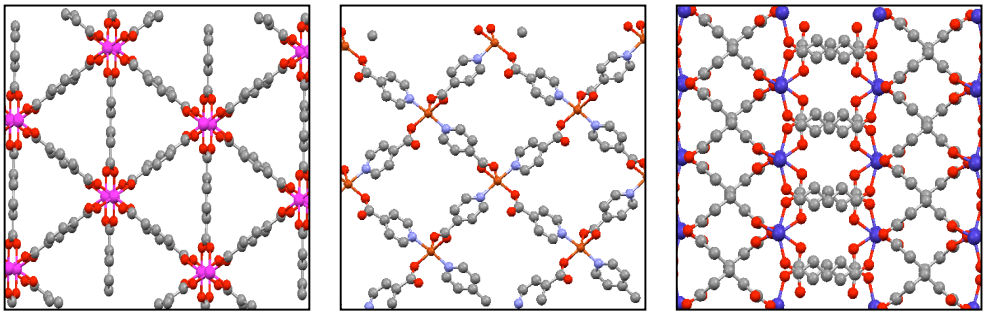

Figure 4-37: MOFs with smaller pore diameters. From left to right Sc-BDC (Perles *et al.* (2005), Miller *et al.* (2005)), Cobalt(II)-Glutarate (Won *et al.* (2002)), $Cu(INA)_2$ (Pichon *et al.* (2006)). Hydrogens are removed for clarity.

4.7 Conclusions

In this chapter, single component adsorption isotherms and mixture simulations were presented for xylene isomers in MOFs with various pore sizes and shapes. Simulations were performed in the vapour phase and compared with experimental data, where available. The results showed that computational screening approaches can help to narrow down the large number of existing porous MOFs to a few promising able to separate a particular xylene isomer. It was found that MOFs with pores larger than 9 Å show relatively low selectivity as their pores are unable to impose significant confinement effects (Figure 4-38). For this reason, depending on their pore/window shape and functional groups, these MOFs slightly favour a specific xylene isomer over the other as was illustrated for IRMOF-3 and IRMOF-7. The separation of xylenes in MOFs with smaller pores, from ~ 6 to 8.5 Å is more challenging as the competition between energetic and entropic effects decides which isomer is preferentially adsorbed. oX isomers were proven to benefit the most in this range of pore sizes as was shown for MIL-53 and MIL-47. In these structures, molecular packing plays an important role with pronounced preference for the ortho-isomer. MOFs with pore sizes between 4.2 and 5.5 Å exhibit a clear preference for pX isomers, as the lower waist diameter of pX allows for molecular sieving separation as was shown in the small pores of MIL-125-NH_2. These findings are very

important in an industrial context as the pore size criteria allows for a quick identification of promising MOFs which can then be investigated in more detail for practical applications such as PAREX process. Clearly, for an industrial adsorbent, characteristics such as stability and regenerability under process conditions must also be considered to compete with their zeolitic rivals.

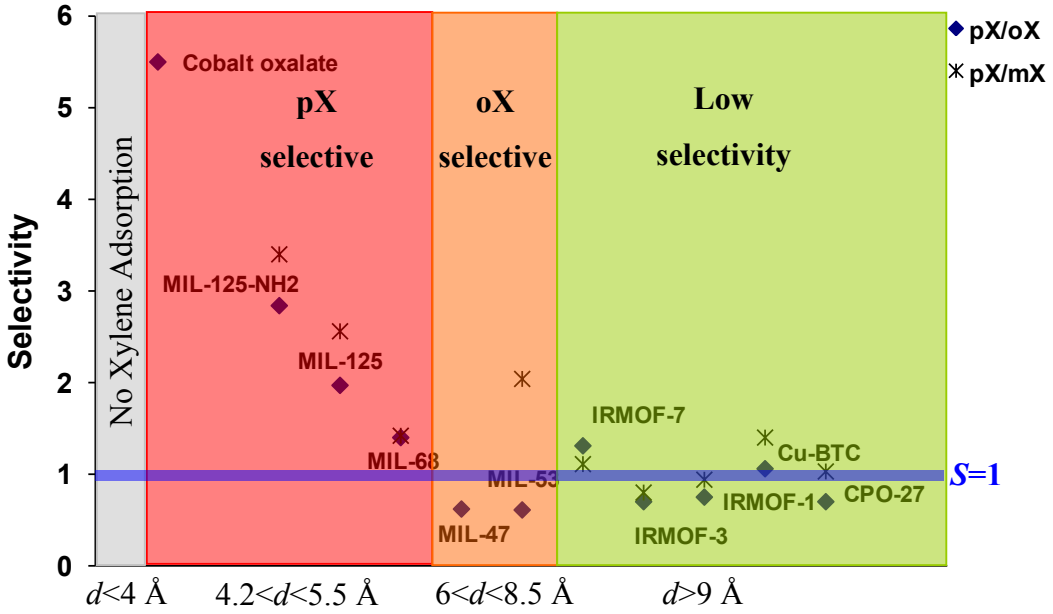

Figure 4-38: pX/oX (diamonds) and pX/mX (stars) equimolar mixture selectivities for the MOFs studied at 1 kPa and 300 K. The diameter (*d*) shows MOFs with corresponding range of pore diameters.

The reported simulation results can build a platform to help experimentalist synthesise new MOFs (i.e. by choosing the appropriate building blocks) for the separation of xylene isomers from the infinite number of possible structures. For further investigations, frameworks such as ZIFs containing large pores and narrow windows of the right size for pX selectivity should be studied to account for the rather low adsorption capacity of smaller MOFs while achieving high selectivity.

Chapter 5 Origin of Enantioselectivity in a Chiral Metal-Organic Framework

This chapter investigates the nature of enantioselectivity behaviour of the homochiral metal-organic framework [Ni_2(L-asp)$_2$(bipy)] for a number of chiral diol molecules and compares the results to experimental data available in the literature. Competitive adsorption for racemic mixtures and single component isotherms are studied using configurational biased grand canonical Monte Carlo simulations. The relationship between enantioselectivity and size and shape of the chiral diols is examined. In order to identify various guest-framework interactions, detailed geometric analysis such as radial distribution functions and histograms along with simulation snapshots are presented. In addition, the influence of framework size on enantioselectivity is investigated through simulation.

5.1 Introduction

Many natural and synthetic compounds are chiral, which means they can exist in left- or right-handed forms that are mirror images of each other. Chirality is important in the production of, for example, drugs as usually only one of the two possible forms of drug molecules is biologically active depending on the configuration of their stereocenteres. As the physical properties of chiral molecules are very similar, classical separation methods are not suited for enantioseparation and methods such as chromatography, crystallisation and stereosynthesis have been developed for this task during the past two decades (Hare and Gilav (1979), Hyun *et al.* (2003), Mikami and Matsukawa (1997), Rekoske (2001), Sheldon (1993)). In chromatography, different interactions between enantiomers with the chiral receptor are the driving force for enantioseparation but limited scalability and lack of diversity of the receptors are the main disadvantages of this method (Gübitz and Schmid (2001)).

Porous materials such as zeolites are commonly used for separation purposes, but among them only a handful exhibit chiral frameworks (Tang *et al.* (2008)). With the rising industrial demand and emergence of various enantiopure drugs, there has been growing interest in developing novel enantioseparative methods. As shown in

previous chapters, metal-organic frameworks (MOFs) are promising materials for separation purposes as the size and the shape of their pores are tuneable, thus providing access to a wide range of porous structures including chiral cavities for enantioselective separation purposes. Due to this versatility, the design of homochiral MOFs has received great attention as they have potential for chiral separation applications. In the literature, a number of chiral MOFs have been examined for asymmetric catalysis and enantioselectivity ranging from mesoporous isoreticular frameworks to microporous networks with thin films (Seo *et al.* (2000), Padmanaban *et al.* (2011), Bradshaw *et al.* (2004), Sun *et al.* (2007), Dybtsev *et al.* (2006), Liu *et al.* (2012), Ma *et al.* (2010)) but studies on the molecular level using simulations are still very scarce (Bao *et al.* (2009), Bao *et al.* (2010)). Recently, Bao *et al.* (2012) used molecular simulations to screen eight homochiral MOFs for 19 chiral compounds and concluded that enantioselectivity is highly correlated with a close match between the pore size and the size of the sorbate, although there is a small possibility of obtaining no enantioselectivity even when a close match exists between the two.

There are only a limited number of studies available in the literature that report not only the synthesis and structure of a chiral MOF but also the successful separation of more than one chiral mixture. The work by Vaidhyanathan *et al.* (2006) therefore emerged as an ideal case study as the homochiral MOF $[Ni_2(L\text{-asp})_2(bipy)]$ (**1**) exhibits a whole range of enantioselectivities for a total of nine different chiral diols considered.

This MOF allows to study the sensitivity of enantioseparation on subtle changes of pore size in detail and provides insight how the pore topology and therefore guest-framework recognition in the pore is influenced by the distribution/shape of these closely related chiral diols. Using molecular simulations, the significant role of packing effects at high loadings that could not be explained experimentally is also demonstrated.

5.2 Diols and MOF structures

In this thesis, five shorter chiral diols out of the nine in the experimental work by Vaidhyanathan *et al.* (2006) were studied: (S,R)-1,2-propanediol, (S,R)-1,2-butanediol, (S,R)-1,3-butanediol, (S,R)-1,2-pentanediol and, (S,R)-2,4-pentanediol (Figure 5-1). These diols were selected to keep the computational costs down while allowing to study the effect of chain length and the different positions of hydroxyl groups (i.e, 1,2- or 1,3-) on the carbon chains in detail.

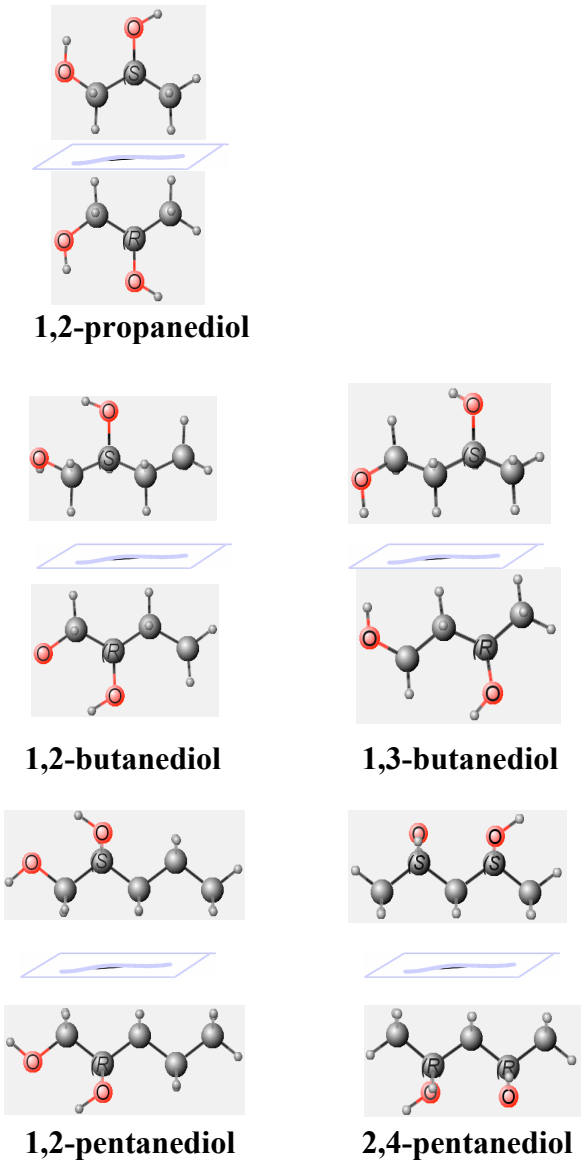

Figure 5-1: The structure of chiral diols studied. The chiral centres are shown with R and S. The oxygens in the hydroxyl groups are presented as red spheres.

The structure of $[Ni_2(L\text{-}asp)_2(bipy)]$ (**1**) (Figure 5-2a) consists of one-dimensional channels with an approximate diameter of 3.85 Å formed by Ni (L-aspartic acid) clusters connected by the length of 4,4'-bipyridine (bipy) ligands. This pillared structure creates pockets on each side of the channel creating a screw-like homochiral void as illustrated by the red circles in Figure 5-2b. The structure also contains protrusions in the upper rims of the bipy layers running along the *y*-axis (Figure 5-2c).

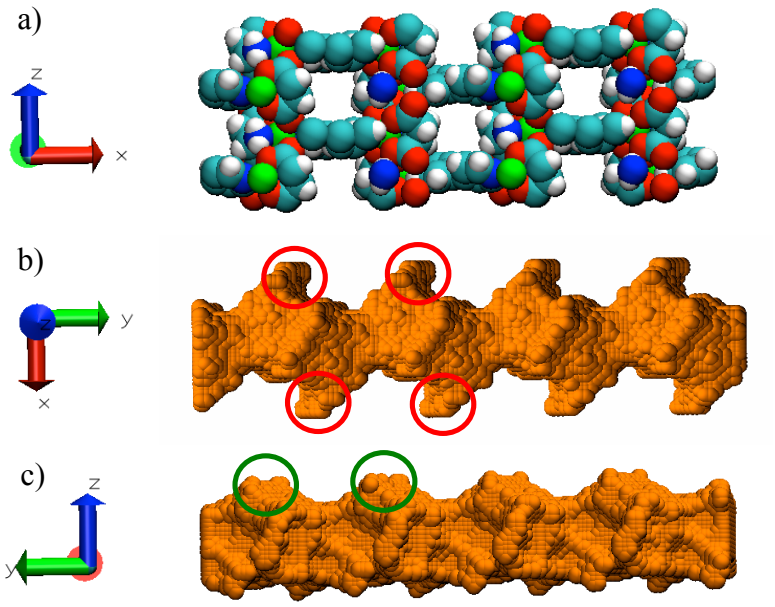

Figure 5-2: Schematic view of the channel in 1 determined by a method described by Sarkisov and Harrison (2011). a) front view of $[Ni_2(L\text{-}asp)_2(bipy)]$ framework. C cyan, O red, N blue, H white and Ni green. b) Illustration of the channel void with pockets highlighted by red circles and c) view along the *y* axis of the channel with protrusions highlighted by green circles.

5.3 Simulations and models

The adsorption isotherms and mixture simulations of the diols studied in **1** were obtained by performing grand canonical Monte Carlo (GCMC) simulations implemented in the RASPA simulation package (Dubbeldam *et al.* (2008)). The molecules were randomly translated and rotated with equal probability. To speed up configuration sampling, configurational biased (CB) insertions and deletions, regrowth and partial regrowth and in the case of binary mixtures the identity swap were used again with equal probability. The ratio of the CB moves to the traditional MC moves was 5:1 for single component simulations and 10:1 for mixture simulations ensuring that the acceptance ratio of each move was above ~ 0.1-0.2 % during the production cycles. Furthermore, each simulation was run at least five times with different random numbers to ensure proper sampling of the phase space. For single component isotherms, 1.2×10^5 equilibration and 1.3×10^5 production cycles were used for each point of the isotherm whereas for the mixtures 1×10^6 cycles were used of which the first half were used for equilibration and rest for sampling the averages. Here, a cycle is defined as one MC move per molecule. Partial pressures were used as the input for the GCMC simulations. All simulations were run at 278 K, the temperature used in the experiments by Vaidhyanathan *et al.* (2006)). The racemic mixture simulations were carried out at maximum loading to replicate the experimental liquid phase enantiomeric excess values where the pore channels are filled with adsorbate molecules. The simulation cell included 16 (2×4×2) unit cells with dimensions of 22.245 Å × 6.790 Å × 7.738 Å for each unit cell. The framework atoms were kept rigid at their crystallographic positions.

The standard 12-6 Lennard-Jones (LJ) potential, truncated and shifted at a cut-off distance of 15 Å, was used for all guest-guest and guest-framework interactions. The LJ parameters for the framework atoms were taken from the Universal Force Field (UFF) by Rappe *et al.* (1992), while the OPLS-AA (Jorgensen *et al.* (1996), Jorgensen (1986)) force field was used to model diols. Lorenz-Berthelot mixing rules were used to calculate mixed LJ parameters. Angle bending and dihedral torsion were taken into account to describe the intramolecular interactions of the diols. Fixed bond lengths were used to increase the efficiency of simulations. It has been shown

that replacing fixed bond lengths with stretching potentials has no substantial effect in Monte Carlo simulations of adsorption (Chen *et al.* (2001). LJ parameters along with bending and torsion parameters are listed in Table 5-1 to Table 5-3.

Table 5-1: Lennard-Jones and partial charges parameters used for 1 and diols.

Species	Site	σ (Å)	ε k_B^{-1} (K)	charge (e)	Reference
MOF	Ni	2.5	7.5	Table 5-4	(Rappe *et al.* (1992))
	O	3.1	30.2		
	N	3.2	34.7		
	C	3.4	52.8		
	H	2.5	22.1		
C_RCH3		3.5	33.2	-0.180	(Jorgensen *et al.* (1996))
C_RCH2OH		3.5	33.2	0.145	
C_R2CH2		3.5	33.2	-0.120	
C_R2CHOH		3.5	33.2	0.205	
H_RH		2.5	15.09	0.06	
O_H		3.1	85.5	-0.683	
H_O		0	0	0.418	

Table 5-2: Bond bending potential parameters for diols (Jorgensen *et al.* (1996)).

Site	Site	Site	K (kcal mol^{-1} rad^{-2})	Θ_{eq} (°)
C	C	C	58.35	112.7
C	C	OH	50.0	109.5
C	C	HC	37.50	110.7
C	OH	HO	55.0	108.5
HC	C	OH	35.0	109.5
HC	C	HC	33.0	107.8

Table 5-3: Torsion potential parameters for diols (Jorgensen *et al.* (1996)).

Site	Site	Site	Site	V_1 (kcal mol^{-1})	V_2 (kcal mol^{-1})	V_3 (kcal mol^{-1})	V_4 (kcal mol^{-1})
HC	C	C	HC	0	0	0.3	0
HC	C	C	C	0	0	0.3	0
C	C	C	C	1.3	-0.05	0.2	0
HC	C	OH	HO	0	0	0.3524	0
HC	C	C	OH	0	0	0.468	0
C	C	C	OH	1.711	-0.5	0.663	0
C	C	OH	HO	-0.356	-0.174	0.492	0

The Ewald summation technique was used for long range electrostatic interactions for both guest-guest and guest-framework interactions. The partial charges of the metal-organic framework **1** were determined from density functional theory (DFT) calculations on a representative cluster isolated from the MOF's unit cell crystallographic positions and the resulting uncoordinated atoms were terminated by hydrogen atoms as shown in Figure 5-3. DFT calculations were used with B3LYP level of theory and 6-31G* basis set. B3LYP is normally applied for MOFs as it provides good description of transition metals (Li *et al.* (2011)). The calculations were carried out with the Gaussian 09 package (Frisch *et al.* (2009)) using a grid in ChelpG method (Breneman and Wiberg (1990)). Table 5-4 shows the resulting partial charges that were used in the GCMC simulations.

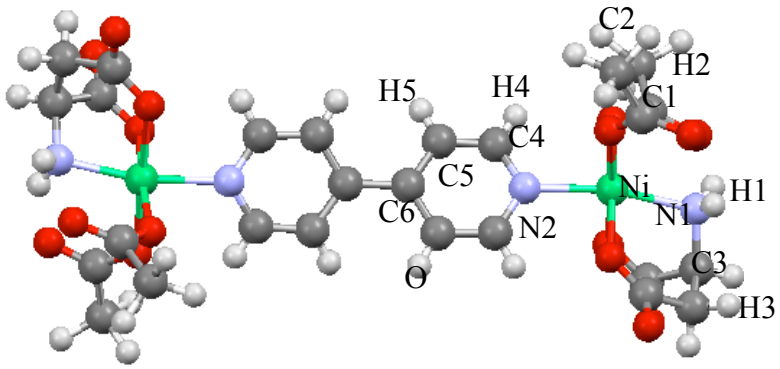

Figure 5-3: Representative cluster used for obtaining partial charges in $[Ni_2(L\text{-}asp)_2(bipy)]$ framework (1).

Table 5-4 : Atomic partial charges in 1 obtained from DFT calculations.

atom type	charge (e)	atom type	charge (e)
Ni	0.92	C3	0.2
O	-0.63	H3	0.03
N1	-0.44	C4	0.08
H1	0.32	H4	0.14
N2	-0.05	C5	-0.22
C1	0.79	H5	0.15
C2	-0.29	C6	0.16
H1	0.10		

5.4 Racemic mixture adsorption results

In order to validate the simulated enantiomeric excess trends with the ones obtained experimentally, GCMC simulations of racemic mixtures for the chiral diols in **1** were performed. The racemic mixture simulations were carried out at high loading and 278 K. These conditions were chosen to replicate the experimental enantiomeric excess (*ee*) values which were measured in liquid phase where the pore channels are nearly filled with adsorbate molecules. The enantiomeric excess is commonly used to determine the excess of one enantiomer over the other and is calculated from the binary mixture using:

$$ee = \frac{R - S}{R + S} \times 100 \qquad \textbf{5-1}$$

where R and S are the amount of right- and left-handed enantiomers adsorbed, respectively. In this definition any value of *ee* greater than zero represents preferential adsorption towards the R-form.

Table 5-5: The enantiomeric excess (*ee*) values for the diols adsorbed in 1 at 278 K. The experimental values are taken from Vaidhyanathan *et al.* (2006).

	ee	*ee* (exp.)
1,2-propanediol	7.1 ± 6.9	5.35
1,2-butanediol	14.4 ± 7.4	5.07
1,3-butanediol	34.3 ± 6.7	17.93
1,2-pentanediol	42.8 ± 5.8	13.9
2,4-pentanediol	21.2 ± 9.8	24.5

Table 5-5 summarises the *ee* values obtained from the simulations together with the experimental data by Vaidhyanathan *et al.* (2006). The simulation results are in fairly good agreement with the available experimental data (especially considering that no error bars are reported for the experimental data) demonstrating that the simulations are not only able to reproduce the general preference of this MOF synthesized with L-aspartate linkers to take up R-enantiomers preferentially but also to reproduce the more subtle trends. The degree of *ee* changes with hydrocarbon chain length and more interestingly with the relative position of hydroxyl groups on a fixed chain length. In the case of the shortest diol, 1,2-propanediol, very low enantioselectivity is observed. For the butanediols, the enantioselectivity in **1** is larger for a mixture of 1,3-butanediol enantiomers (*ee* = 34.3) than 1,2-butanediol (*ee* = 14.4) in agreement with experimental data. However, for the longer chain pentanediol molecules, the 1,3 and 1,2-conformations (i.e., hydroxyl groups on non-adjacent and adjacent carbons) do not follow the same descending *ee* trend seen in butanediol and experimentally, with larger *ee* values observed for 1,2-pentanediol (*ee* = 42.8) rather than 2,4-pentanediol (*ee* = 21.2). It is worth to mention that the simulations were carried out in a perfect enantiopure crystal of **1** with all solvent molecules removed. However, the samples of **1** used in experiments were only verified to be greater than 95 %

enantiopure. Lower enantiopurity proved to reduce *ee* values in experiments for all cases.

5.5 Single component adsorption results

In order to investigate if the enantioseparation behaviour observed in **1** is driven by energy differences between chiral enantiomers and the framework, Monte Carlo simulations of isolated enantiomers were performed in the simulation cell of **1.** Table 5-6 summarises the diol-framework potential energies for pair R- and S-enantiomers.

Table 5-6: The potential energies obtained from Monte Carlo simulations for one molecule in 1 at 278 K.

	R (kJ/mol)	S (kJ/mol)
1,2-propanediol	-99.8 ± 7.9	-86.5 ± 6.3
1,2-butanediol	-112.1 ± 0.5	-97.5 ± 9.1
1,3-butanediol	-108.8 ± 11.8	-110.7 ± 8.1
1,2-pentanediol	-120.3 ± 9.6	-96.0 ± 12.8
2,4-pentanediol	-123.8 ± 5.0	-129.7 ± 0.12

A general trend can be deduced from Table 5-6. Higher interaction energies with the framework are observed for R-enantiomers except for diols with 1,3-conformation (i.e. 1,3-butanediol and 2,4-pentanediol) where the S-enantiomer has slightly stronger interaction. However, considering reported error bars, there is only a small difference between the interaction energies of the enantiomers, in agreement with the quantum mechanical calculations carried out by Vaidhyanathan *et al.* (2006). However, experimental *ee* results show that the R-enantiomer is preferred in all cases with even higher *ee* values for 1,3-conformation diols. This implies that the adsorption mechanism and enantioselectivity is not necessarily energy driven and likely occurs by entropic effects at higher loadings (i.e. liquid phase). For this reason and in light of the good agreement of the obtained computational *ee* values with the experiments showing preference for R-enantiomers for all diols studied and to further examine the adsorption mechanism of diols enantiomers in **1** at different loadings, the pure component adsorption isotherms were computed using GCMC simulations

at 278 K and are illustrated in Figure 5-4. For all diols except 1,2-propanediol, the single component isotherms show a higher maximum uptake of the R-form than the S-form. For the butanediols, it can be seen from the Henry (i.e. low pressure) region of the pure component isotherms in Figure 5-4b and c, that the 1,3-form of butanediol is adsorbed more strongly in comparison to 1,2-butanediol enantiomers. The favourable nature of 1,3-conformation of diol functionalities at low loading was further confirmed by conducting additional mixture simulations of (S)-1,3- and (S)-1,2-butanediols, and (R)-1,3- and (R)-1,2-butanediols at 1 Pa which showed excess values of the 1,3-conformation over the 1,2-conformation of 49 % and 36 %, respectively.

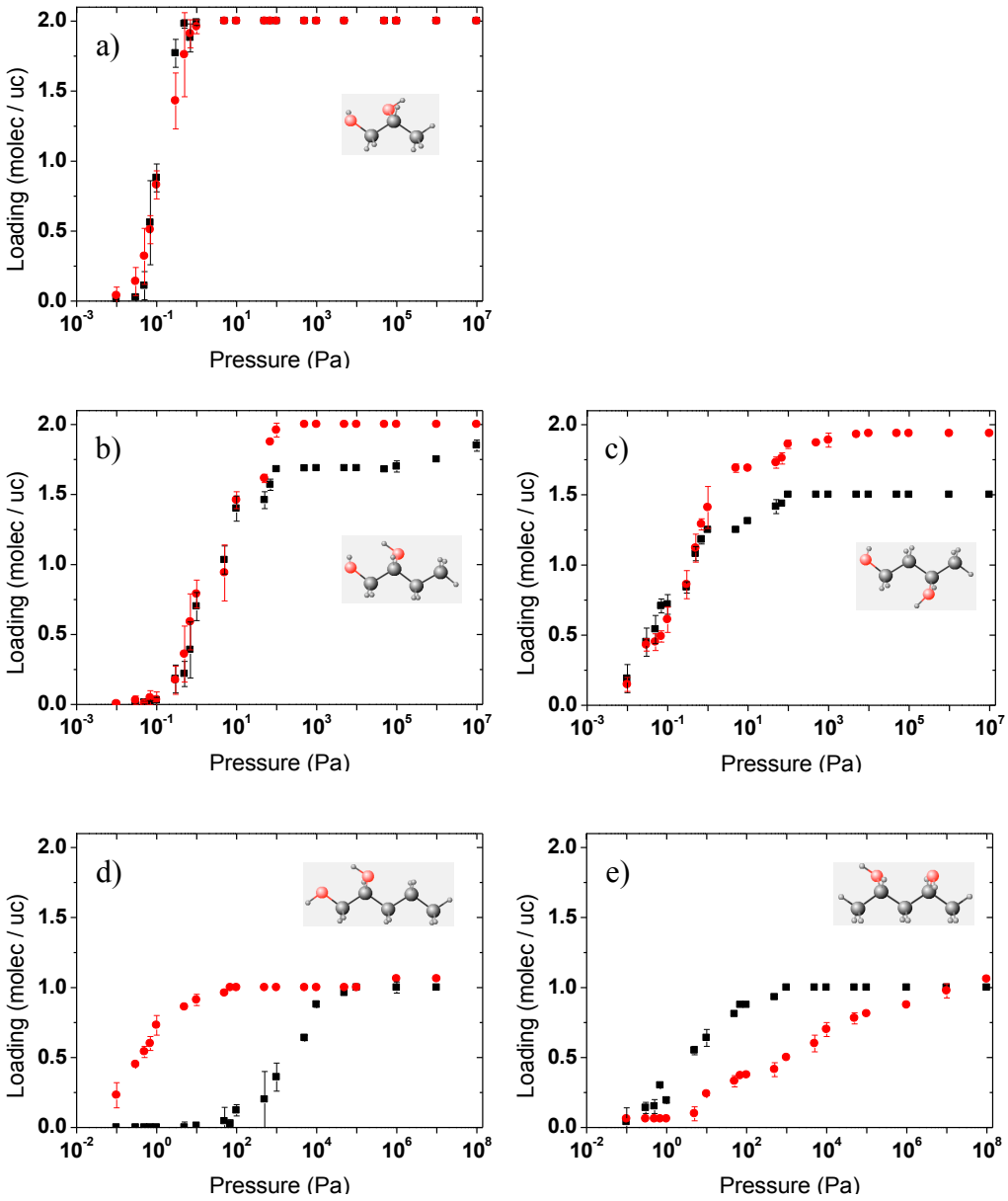

Figure 5-4 Single component adsorption isotherms in 1 at 278 K for a) 1,2-propanediol, b) 1,2-butanediol c) 1,3-butanediol, d) 1,2-pentanediol and e) 2,4-pentanediol (R: red circles and S: black squares). The insets show the respective diol molecule with the OH groups highlighted in red.

The adsorption isotherms of the two diols with 1,3-conformations, 1,3-butanediol and 2,4-pentanediol are illustrated in Figure 5-4c and Figure 5-4e, respectively. In agreement with higher interaction energies obtained for S-1,3-conformations in Table 5-6, for 1,3-butanediol the S-form adsorbs marginally stronger at low loadings

while at higher loadings the R-enantiomer adsorbs preferentially when the uptake exceeds ~1 molecule / uc. This means that the two enantiomers interact differently with the framework and with each other at various loadings. Figure 5-5 compares the average total diol-diol and diol-framework potential energies and shows higher interaction energies for (R)-1,3-butanediol at maximum loading. Similar but stronger affinity for the S-enantiomer at low loading is also observed for the other 1,3-conformation investigated, the longer chain diol 2,4-pentanediol (Figure 5-4e and Figure 5-5). The saturation loading for both (R)- and (S)-2,4-pentanediol is 1 molecule / uc. This saturation loading is almost half of the loading seen for shorter diols such as propanediols and butanediols.

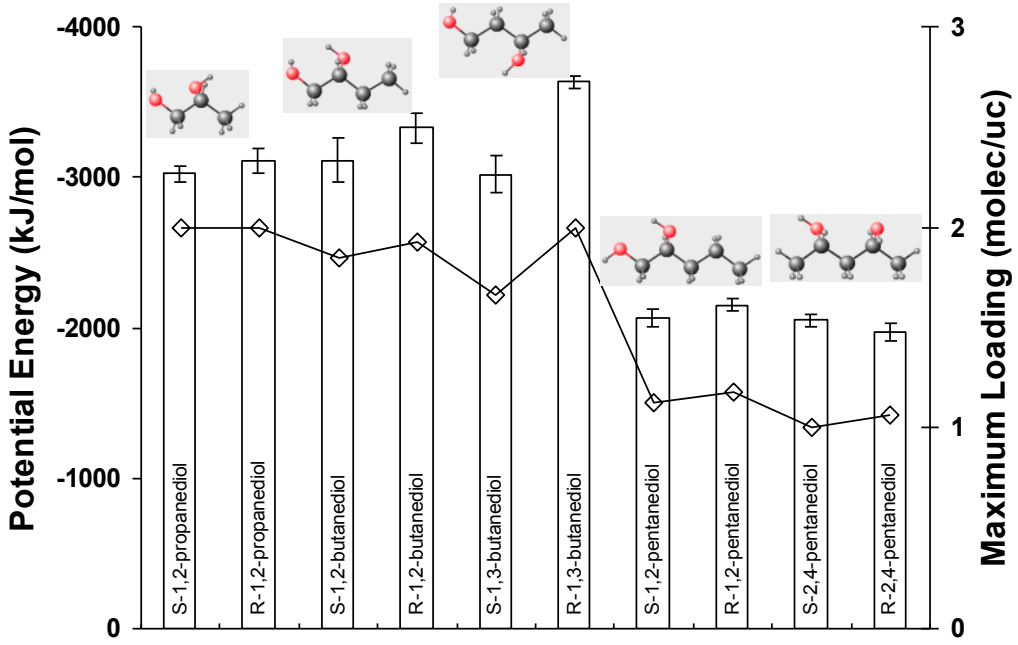

Figure 5-5: Average total potential energies for pure component diols at their maximum loading and 278 K. Potential energies and maximum uptake are shown with columns and diamonds, respectively.

In diols with 1,2-conformation, the extent of preference in **1** towards R-enantiomers reduces and again becomes dependent on the hydrocarbon chain length in shorter chain diols i.e. propanediol and butanediol. For example, in the case of the shortest diol, 1,2-propanediol, both enantiomers show rather similar uptake for the entire isotherm (Figure 5-4a). Thus, the concentration dependence of the preference and

hence the extent of enantioselectivity lowers as the two enantiomers are small enough to interact in a similar fashion with the framework and exhibit no significant packing effects as will be shown later. In 1,2-butanediol (Figure 5-4b), over the entire loading range, the R-enantiomer is preferentially adsorbed especially at higher loading up to 2 molecules / uc due to better packing and higher guest-guest and guest-framework interactions (see Figure 5-5). On the other hand, for the longest diol, 1,2-pentanediol (Figure 5-4d), although R is preferred in particular at lower loadings, the maximum uptake goes slightly above the loading of 1 molecule / uc leading to better R-enantioselectivity.

5.6 Structural Analysis of diols at high loadings

In order to study the adsorption mechanism and the nature of enantioselective discrimination in more detail, structural information such as pair atom distance histograms, radial distribution functions and simulation snapshots were compared for each pure component diol enantiomers at maximum loading and 278 K.

5.6.1 (S,R)-1,2-propanediol

As was shown in Table 5-5, the extent of *ee* is very low in both experiments and simulations for the smallest diol, 1,2-propanediol and both enantiomers approach the saturation plateau of 2 molecules / uc at 1 Pa in the pure component isotherms (see Figure 5-4a). Figure 5-6 shows the snapshots and detailed structural analysis for 1,2-propanediol. The histograms shown in Figure 5-6a are the average intramolecular oxygen-oxygen (O(H)-O(H)) distances of the hydroxyl groups calculated during the production run of simulations for enantiomers adsorbed in **1**. As it can be seen, both enantiomers exhibit two peaks which are more prominent for the R-form. These peaks correspond to the conformations where both OH groups are in the vicinity of pockets with CH_3 group in the channel centre, and where one OH stays close to the pocket leaving CH_3 group in the vicinity of the opposite pocket (Figure 5-6b). As discussed in chapter 3, the radial distribution function (RDF) is a powerful tool to study various configurations of adsorbate atoms with respect to other adsorbates and the adsorbent framework providing a spatial distribution of atoms. In Figure 5-6c, the

nickel atom in the RDF represents an atom inside the pockets, therefore providing a measure for the relative distance between the hydroxyl groups of the diols with the framework pockets. The CH_3-CH_3 RDF (Figure 5-6d) illustrates relative distances between the adsorbate molecules. The differences between enantiomers in both RDFs are negligible. The first peak in the OH-Ni RDF shows that the OH groups in R-enantiomers get marginally closer to the pockets while the number of OH groups close to the pocket in the S-form is higher. The peaks in the CH_3-CH_3 RDF are rather similar (The R-form CH_3 groups show slightly closer distance) meaning that 1,2-propanediol enantiomers sit in the framework channels with similar arrangements. Although the R-form exhibits more conformations in the channel, the small size of the molecules leads to poorer enantioseparation cancelling packing effects as shown in Figure 5-6b.

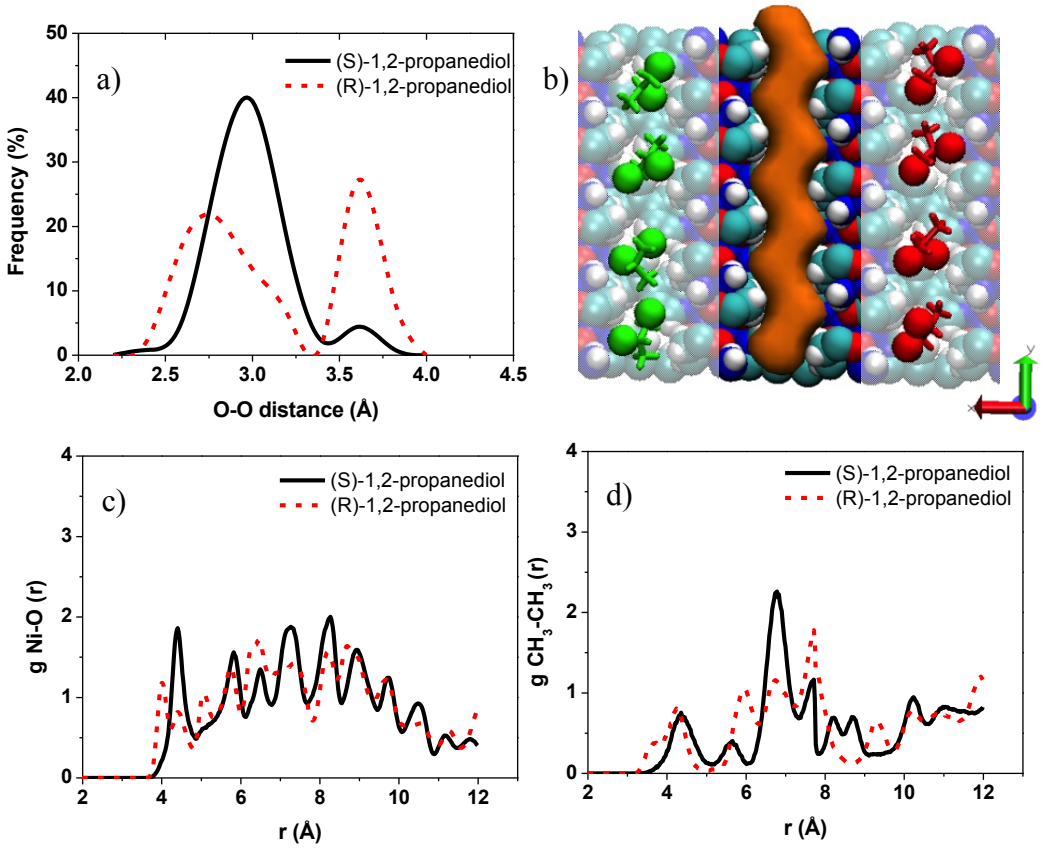

Figure 5-6 a) Histograms of intramolecular oxygen-oxygen (O(H)-O(H)) distance for 1,2-propanediol enantiomers. b) Pure component snapshots for 1,2-propanediol enantiomers: R (red), S (green). Hydroxyl groups are shown in spacefill representation. The pore space with pockets is shown in orange in the middle. c) nickel-oxygen radial distribution function, d) methyl-methyl radial distribution functions. All figures are obtained for 1,2-propanediol enantiomers adsorbed in 1 from pure component GCMC simulations at maximum loading and 278 K.

5.6.2 (S,R)-1,3-butanediol

Figure 5-7 shows the detailed analysis for 1,3-butanediol where high *ee* value of 34.3 was observed from the simulations. In (S)-1,3-butanediol, 86 % of the O(H)-O(H) distance lies between 3.9 to 5.1 Å, maximizing its interaction energy with the framework by positioning both OH groups in very close proximity to the channel pockets between the two neighbouring 4,4'-bipyridine ligands as shown in Figure 5-7b by the green circles. This range of O(H)-O(H) distance is 20 % higher than that seen for the R- form. This stretched O(H)-O(H) conformation also explains the higher uptake and higher guest-framework interaction energies for S-enantiomers at

lower loading in the isotherm (Figure 5-4c). However, this extended configuration becomes unfavourable for S-molecules at higher loadings as the bulky CH_3 groups sit in the centre of the channel making them pack less efficiently as no further molecule can be positioned in the immediate vicinity of the CH_3 group. Thus, a lower maximum uptake is observed for (S)-1,3-butanediol. In (R)-1,3-butanediol, although the adsorption sites are similar to the ones of the S-enantiomers, various configurations are formed as multiple distinct peaks show in the O(H)-O(H) histogram in Figure 5-7a. The first peak (3.1 Å) corresponds to OH groups positioned closely together with the middle OH group tilted towards the protrusions of the channel occupying the accessible cavity volume (see Figure 5-2). The opposite pocket is occupied by the CH_3 group as marked by the dashed red circle in Figure 5-7b. The larger peak (4.9 Å) corresponds to a conformation similar to the extended form of the S-enantiomer with both hydroxyl groups located in opposite pockets.

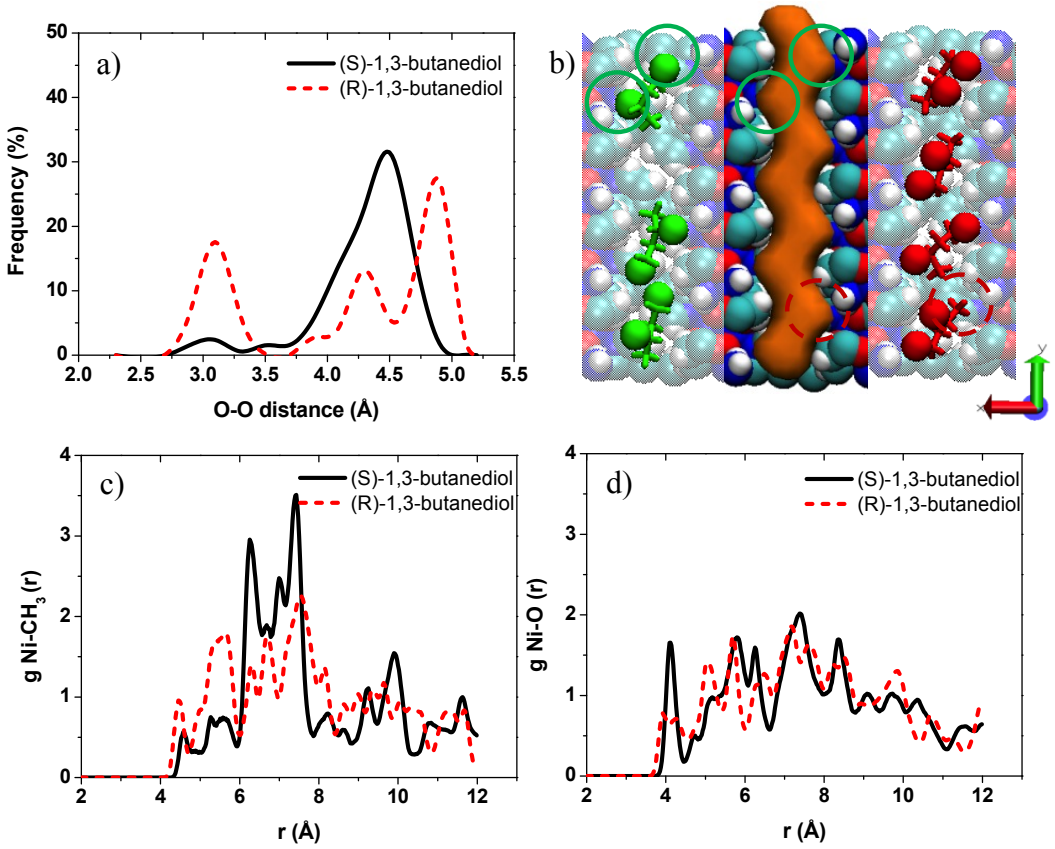

Figure 5-7 a) Histograms of intramolecular oxygen-oxygen (O(H)-O(H)) distance for 1,3-butanediol enantiomers. b) Pure component snapshots for 1,3-butanediol enantiomers: R (red), S (green). Hydroxyl and methyl groups in 1,3-butanediol molecules are marked with solid green and dashed-red circles, respectively. Hydroxyl groups are shown in spacefill representation. The pore space with pockets is shown in orange in the middle. c) Nickel-methyl radial distribution functions, d) nickel-oxygen radial distribution functions. All figures were obtained for 1,3-butanediol enantiomers adsorbed in 1 from pure component GCMC simulations at maximum loading and 278 K.

The first peak in Figure 5-7d is larger for the S-enantiomer. This shows the closer proximity of OH groups of the S-enantiomer to the pockets. It further demonstrates the favourable extended conformation with both hydroxyl groups in the pocket for the S-enantiomer as shown in Figure 5-7b. This configuration also favours the formation of hydrogen bonds between the alcohol groups and the carboxylate or amine group of the aspartic acid. The first two larger peaks detected in the CH_3-Ni

radial distribution function in Figure 5-7c also confirms the better packing mechanism of R-enantiomers where the bulky methyl groups are in closer proximity to the pockets than for the S-enantiomer. By adopting these configurations, R-molecules can pack more effectively in the framework's chiral environment at high loading compared to their S rivals as illustrated in Figure 5-7b. This is in agreement with the simulated *ee* values and the experimental data for mixtures in liquid phase where the framework channels are filled with guest molecules and R is preferentially adsorbed.

At low loadings, the simulation results match well with the molecular mechanics docking studies performed by Vaidhyanathan *et al.* (2006)) at low loadings. However, their simulations - in contrast to this work - were unable to explain the R-enantioselectivity of the diols observed in the liquid phase i.e. at higher loading. The reason for this is that they studied the guest-framework interaction of isolated molecules thus neglecting the entropic contribution and packing dependency of enantioselectivity at high loadings. The results obtained in this work clearly show that in order to explain the enantioselectivity observed experimentally in the liquid phase, the simulations need to be performed at high loadings to account for packing effects.

5.6.3 (S,R)-1,2-butanediol

The *ee* values for 1,2-butanediol are lower than 1,3-butanediol in both experiments and simulations (Table 5-5). As it can be seen from Figure 5-8a, the distribution of O(H)-O(H) distance exhibits two distinct peaks for (R)-1,2-butanediol which corresponds to the conformations where one OH-group remains close to the pocket with the other OH group oriented towards the protrusions along the channel (Figure 5-8b). The first peaks in the radial distribution function for CH_3-Ni show closer proximity of the methyl group in R-enantiomer to the pockets leaving more space for the adjacent molecule as illustrated in Figure 5-8c. On the other hand, for the S-enantiomer, although the adsorption sites are located between the two neighbouring 4,4'-bipyridine ligands, similar to those for R-enantiomer, the bulky methyl groups are oriented towards the centre of the channel. This orientation causes steric

hindrance for the immediate neighbouring molecule in the channel preventing methyl tails of adjacent molecules to face each other (see Figure 5-8b). This can be further demonstrated in the CH_3-CH_3 radial distribution function between 1,2-butanediol molecules in Figure 5-8d. The height of the first peak at (3.7 Å) is larger due to stronger correlations among adjacent neighbours for R-enantiomers. This means that they can fit more effectively in the inner pore space by positioning their methyl groups close to the pockets which in turn leads to better packing for (R)-1,2-butanediols.

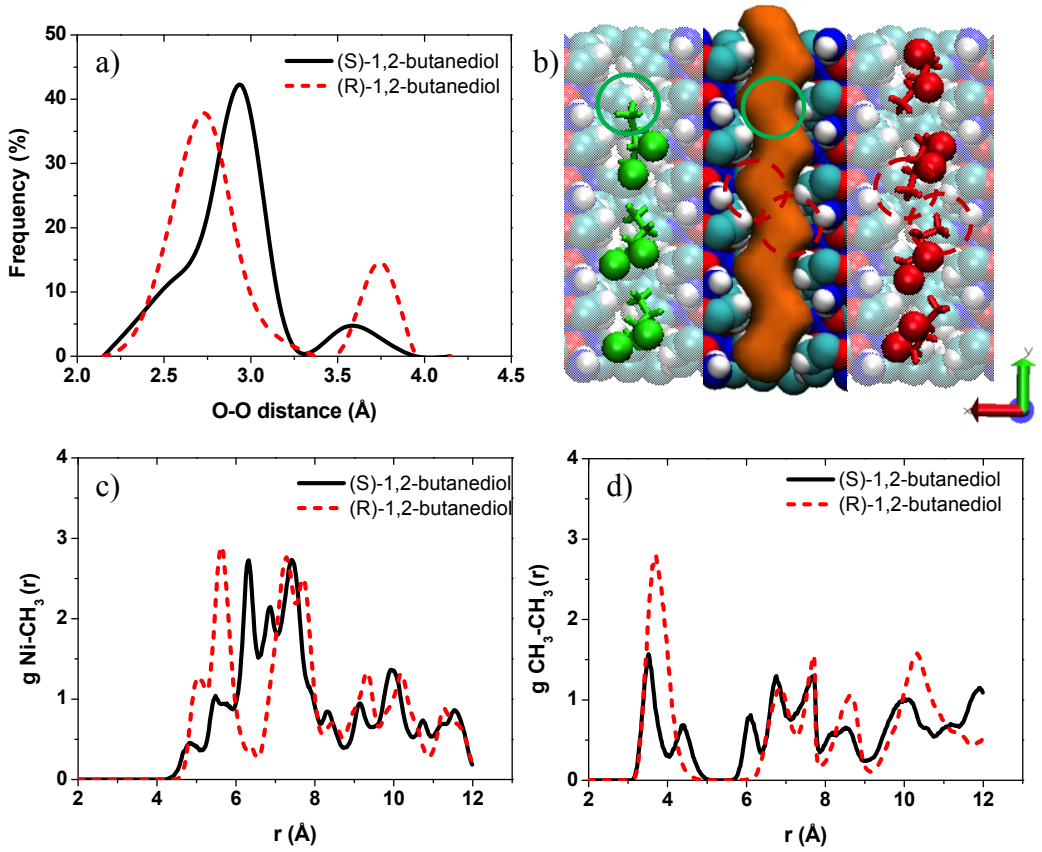

Figure 5-8 a) Histograms of intramolecular oxygen-oxygen (O(H)-O(H)) distance for 1,2-butanediol enantiomers. b) Pure component snapshots for 1,2-butanediol enantiomers: R (red), S (green). Methyl groups in (S)- and (R)-1,2-butanediol molecules are marked with solid green and dashed-red circles, respectively. Hydroxyl groups are shown in spacefill representation. The pore space with pockets is shown in orange in the middle. c) Nickel-methyl radial distribution functions, d) methyl-methyl radial distribution functions. All figures were obtained for 1,2-butanediol enantiomers adsorbed in 1 from pure component GCMC simulations at maximum loading and 278 K.

5.6.4 (S,R)-2,4-pentanediol

The adsorption behavior of 2,4-pentanediol enantiomers is similar to what is seen in 1,3-butanediol with preferential uptake of S-enantiomers and a maximum loading of ~ 1 molecule / uc. The reason for the low saturation uptake is that the S-enantiomers have both their OH groups sitting in the pockets with an O(H)-O(H) equilibrium distance of ~ 4.2 Å as shown in Figure 5-9a. This stretched form results in both bulky methyl groups being located in the centre of the channel as illustrated in Figure 5-9b. Unlike shorter diols where higher interaction energies were found for the R-form at maximum loading, this extended conformation for (S)-2,4-pentanediol is energetically more favourable at 1 molecule / uc as shown previously in Figure 5-5. With both OH groups close to the pockets (Figure 5-9c), both bulky methyl groups are located in the centre of the channel. This means that the immediate neighbouring adsorption sites remain empty as no further molecule fits in the gap between the tails of neighbouring molecules (see the shaded area in Figure 5-9b). Therefore, the maximum uptake for the S-enantiomer is 1 molecule / uc. R-enantiomers can adopt more conformations with their methyl groups close to the pockets which promotes better packing for the neighbouring molecules as shown in Figure 5-9b and d. Although this adaptability is similar to those seen for shorter diols, the longer chain and the presence of bulky methyl group in the centre of the channel creates an entropic penalty at high loadings over 1 molecule / uc. Thus, with a maximum loading of 1.06 molecules / uc, the enantiomers are too far apart to experience significant guest-guest interactions.

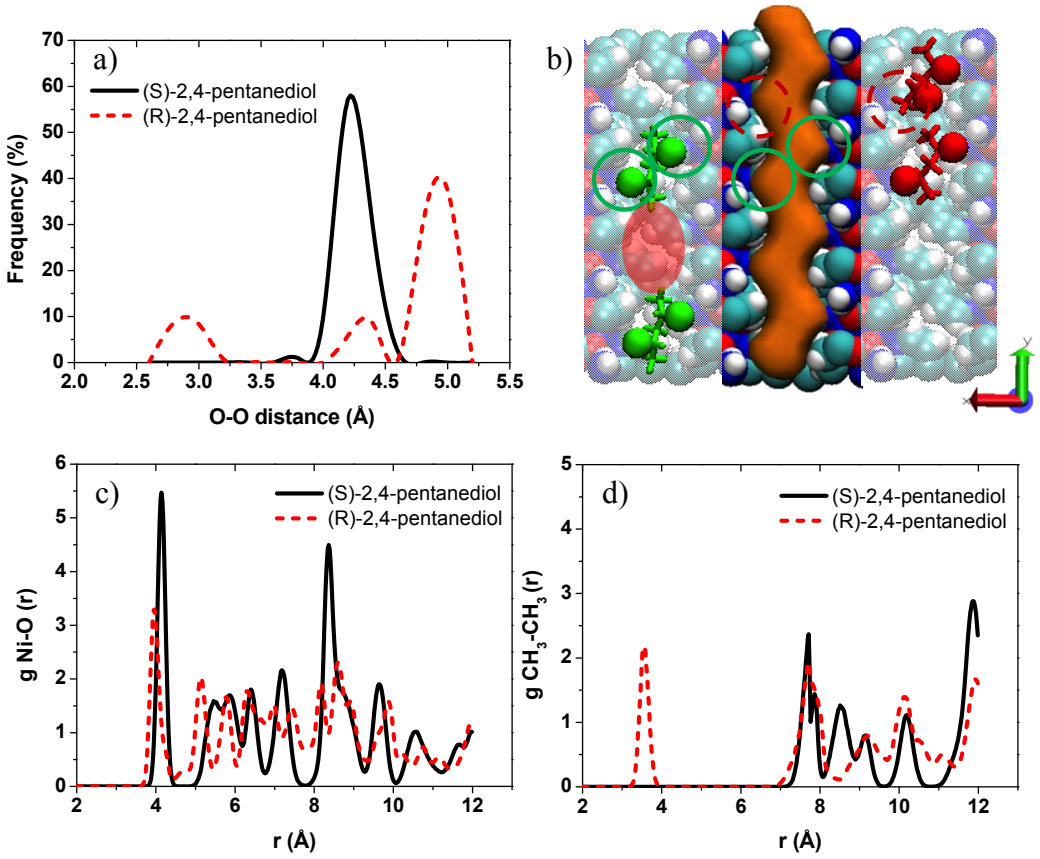

Figure 5-9 a) Histograms of intramolecular oxygen-oxygen (O(H)-O(H)) distance for 2,4-pentanediol enantiomers. b) Pure component snapshots for 2,4-pentanediol enantiomers: R (red), S (green). Hydroxyl and methyl groups in 2,4-pentanediols are marked with solid green and dashed-red circles, respectively. Hydroxyl groups are shown in spacefill representation. The pore space with pockets is shown in orange in the middle. c) Nickel-oxygen radial distribution functions and d) methyl-methyl radial distribution functions. All figures were obtained for 2,4-pentanediol enantiomers adsorbed in 1 from pure component GCMC simulations at maximum loading and 278 K.

5.6.5 (S,R)-1,2-pentanediol

Unlike 2,4-pentanediol, in the case of 1,2-pentanediol, the R-enantiomer is preferentially adsorbed over the whole pressure range and especially at low loadings as shown in Figure 5-4d. Similar to the diols studied so far, higher interaction energies and closer proximities for both OH and CH_3 groups to the pockets were observed for the R-enantiomer (Figure 5-10) suggesting better R-enantioselectivity

whereas in the case of S-enantiomer normally one OH group is placed towards the protrusions of the channel with their CH_3 groups in middle of the pocket.

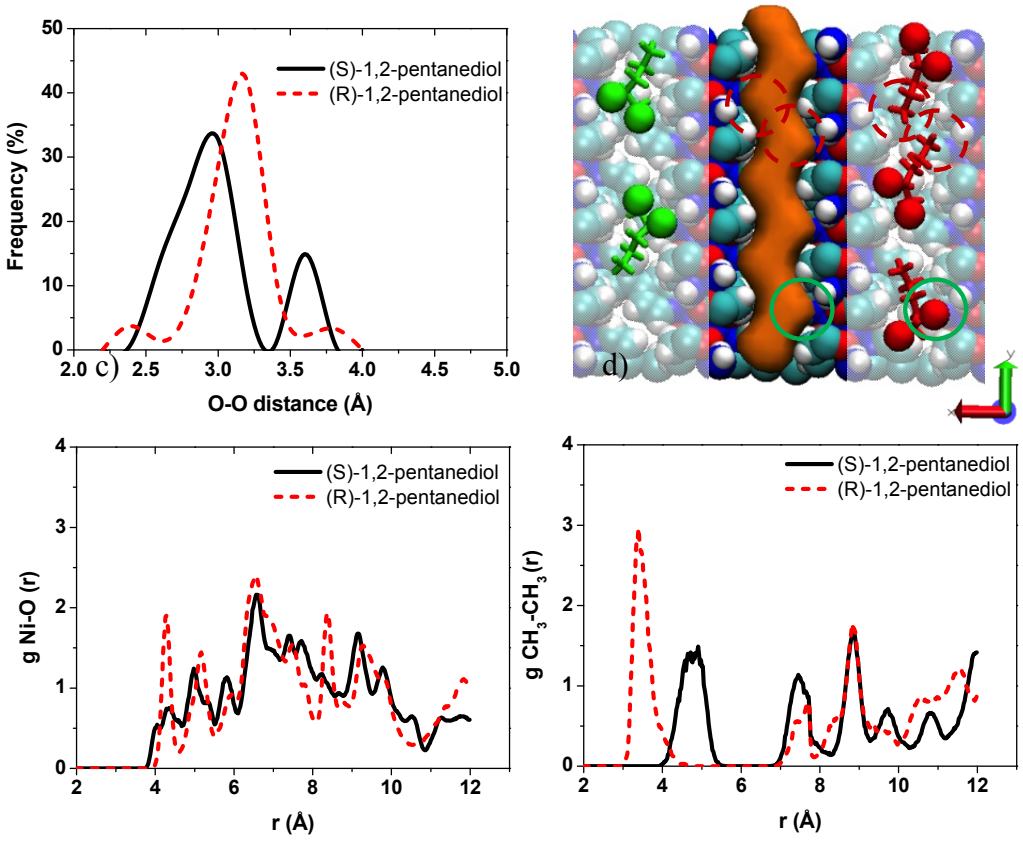

Figure 5-10 a) Histograms of intramolecular oxygen-oxygen (O(H)-O(H)) distance for 1,2-pentanediol enantiomers. b) Pure component snapshots for 1,2-pentanediol enantiomers: R (red), S (green). Hydroxyl and methyl groups in (R)-1,2-pentanediols are marked with solid green and dashed-red circles, respectively. Hydroxyl groups are shown in spacefill representation. The pore space with pockets is shown in orange in the middle. c) Nickel-oxygen radial distribution function, d) methyl-methyl radial distribution functions. All figures were obtained for 1,2-pentanediol enantiomers adsorbed in 1 from pure component GCMC simulations at maximum loading and 278 K.

However, both enantiomers show low pore fillings of ~1.1 molecule / uc with slightly higher loadings than those seen in 2,4-pentanediol (1 molecule / uc) thereby resulting in a rather unexpectedly high *ee* value of ~ 42.8. This high *ee* value shows that despite the good agreement between the experimental and simulation results for the butanediols, with a clearly larger *ee* value for 1,3-butanediol in comparison to

1,2-butanediol, the same ascending order of *ee* trend for the 1,2- and 1,3-conformation of the longest chain diol, pentanediol was not observed (simulated *ee* value of 42.8 (exp. ~ 13.9) and 21.2 (exp. ~ 24.5) for 1,2- and 2,4-pentanediol, respectively). As mentioned earlier, 2,4- and 1,2-pentanediol enantiomers can reach a maximum uptake of slightly over 1 molecule / uc in contrast to the shorter diols which show a saturation uptake of 2 molecules / uc. The change in the order of *ee* values in 1,2- and 2,4-pentanediols can be assigned to the fact that upon inclusion of larger guest molecules the framework of **1** may undergo small structural changes whereas in the simulations the framework is considered as rigid. This may hinder the favourable R-packing mechanism and steric effects to manifest as clearly as was observed for the shorter diols which showed loadings up to 2 molecules / uc.

The results so far indicate that the level of enantioselectivity and the difference in uptake of the two enantiomers become more evident at high loadings (i.e. loadings exceeding ~1 molecule / uc) due to closer packing of the R-enantiomers in the framework. Therefore, in order to investigate if promoting higher adsorption uptake for pentanediols, would lead to larger *ee* values for 2,4-pentanediol in comparison with 1,2-pentanediol, as was observed experimentally, the hard sphere diameter of the LJ potential of the framework atoms was reduced by 10% and the simulations were repeated for the pure component and mixture simulations of 2,4- and 1,2-pentanediol enantiomers at high loading. The reduction in the hard sphere diameter results in an increase of the pore diameter from 3.85 Å to 4.05 Å as shown in Figure 5-11 (Note, that such a change might occur experimentally due to framework flexibility).

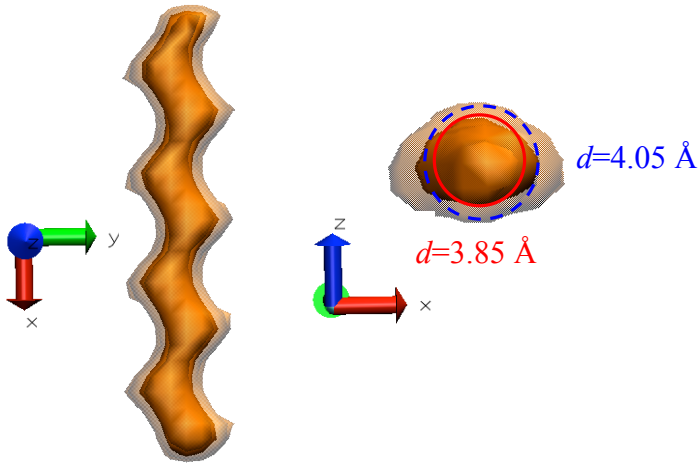

Figure 5-11: Larger channel space in 1 when the hard sphere diameter of LJ potential for all framework atoms is reduced by 10 % (shaded area). The resulting pore diameters measured by the largest sphere that can fit in the framework without overlapping are before and after reduction are shown by the red and dashed blue circle, respectively.

As the available channel space becomes larger, no significant increase in the single component uptake of S-2,4 pentanediol is observed, whereas the R-uptake increased from 1 molecule / uc to 1.25 molecules / uc. The *ee* value also increased from ~ 21.2 to ~ 41 in the racemic mixture simulation. Following the lower enantioselectivity observed for 1,2-conformations in butanediols in comparison to 1,3-conformations, in the case of 1,2-pentanediol, the reduction of the hard sphere diameter leads to a decrease in the *ee* value from ~ 42.8 to ~ 33. Notably, this descending *ee* trend from 2,4- to 1,2-pentanediol racemic mixtures follows a similar trend of *ee* values observed experimentally. This drastic change in enantioselectivity caused by subtle changes in framework structure is further confirmation that enantioselectivity depends strongly on the perfect match between guest-framework size and shape.

5.7 Conclusions

In this chapter, the adsorption mechanism of a number of chiral diols in the chiral metal organic framework $[Ni_2(L\text{-asp})_2(bipy)]$ (**1**) has been investigated by molecular simulation. For each case, the simulations were able to reproduce the preferred R-enantioselectivity observed experimentally in framework **1** derived from L-asp. Depending on the nature of the chiral diol, different modes of interaction and different *ee* values were obtained at various loadings even for diols with fixed chain length. Good agreement for the order of enantiomeric excess between experimental and simulation results was observed for propanediol and butanediol enantiomers. The reported simulation results complement the available experimental data on the molecular level and explain the role of packing effects at high loadings on the *ee* values obtained in **1**. It was also demonstrated how subtle changes in the framework pore size lead to drastic changes in the magnitude and order of enantioselectivity between 2,4- and 1,2-pentanediol enantiomers due to better packing of R-1,3-conformation.

In conclusion, it is not only the chiral environment and the channel surface chemistry which favour the uptake of either the left- or right-handed form but a more important factor for obtaining high enantioselectivities and guest-host recognition is the perfect match in terms of size and shape between the framework and guest molecules. Under these circumstances the enantioselectivity manifests itself in higher *ee*-values when packing effects at high loadings become a significant factor in favour of the more adaptable enantiomer.

Developing a flexible force field capable of reproducing subtle rearrangements of the linkers in response to the adsorption of specifically larger guest molecules should be the subject of future work. It is also interesting to repeat the simulations using framework **1** derived from enantiopure R-asp linkers instead of L-asp and a racemic phase with both L,D-asp linkers to investigate the effects of framework's chirality on enantioseparation.

Chapter 6 Summary and Conclusions

Metal-organic frameworks (MOFs) are multifunctional materials with potential applications from gas storage, separation of gases and liquids to biological applications such as drug delivery (Meek *et al.* (2011)). The use of MOFs for size and shape selectivity has made a great progress during the past few years that may open doors towards industrial selective adsorption and catalytic applications, as their versatile pores are highly tuneable. Understanding the distribution of products influenced by the highly confined pore environments provides valuable information for further development of their applications. Molecular simulations provide rapid guidelines and necessary links between synthetic chemistry and engineering by exploiting underlying molecular interactions of various components inside the confined pores of MOFs.

Extended structures containing calixarenes have attracted attention as the cavities in calixarene structure can act as extra adsorption sites. In a collaborative effort between chemistry and chemical engineering, three MOFs with two degrees of porosity corresponding to both structural and calix[4]arene based linkers were synthesised. Using molecular simulations their potential for the separation of methane and hydrogen mixtures were explored in Chapter 3. The mixture simulations showed high methane selectivity over hydrogen for all three structures mainly due to the better size match between methane and the pores leading to higher adsorption energies. Remarkably, additional adsorption sites accessible to only hydrogens were observed computationally in the Cd-MOF structure. These extra adsorption sites are located in the porosity formed by calix[4]arene-based bowl-shaped linkers. This observation can be in principle further exploited for separation applications even for larger calixarenes i.e calix[6]arene. One of the challenges in the synthesis of calix-based linker is to selectively functionalise the lower and upper rims of TBC4 in a way to obtain conformationally rigid structures. Although lower rim propyl chains in our synthesised H_2caldc keep the calix bowl structure rigid, its inclusion as a MOF linker blocks most of the pore space. Therefore, finding synthetic strategies involving less bulky groups while maintaining calix stability should be the

focus for future research. In addition, further molecular simulations should focus on different functional linkers based on TBC4 testing them for both adsorptive and separative abilities.

The separation of xylene isomers is challenging due to their similar physical properties. In industry, different modes of interaction between xylenes and zeolites are used as the driving force to separate xylene isomers. In Chapter 4 of this thesis, the suitability of MOFs for xylene separation was assessed using molecular simulations. The influence of mainly pore size on preferential adsorption towards each xylene isomer was studied through computational screening. It has been shown that MOFs with large pores (d>9 Å) are unable to impose significant steric hindrance in the pores hence low selectivity values were observed for these MOFs. MOFs with medium size of pores (6<d<8.5 Å) proved to favour o-xylene molecules as they pack more efficiently at high pore fillings. Smaller pores in MOFs (4.2<d<5.5 Å) exhibit molecular sieving effects separating p-xylene molecules from the other isomers due to its lower waist diameter. In line with experiments, the simulations showed that the functionalisation of MIL-125 further enhances the p-xylene preference as bulkier m-xylene and to some extent oX get excluded from the small tetrahedral pores. This finding can be further explored in structures like ZIFs that contain optimum window size and provide higher adsorption capacities to account for the lower adsorption of MOFs with smaller pores. This is the first time that such comprehensive computational work has been carried out for the potential of MOFs for xylene separation. Clearly, in an industrial context characteristics such as regenerability along with chemical and mechanical stability under actual process conditions must be considered before these MOFs can be considered as zeolitic rivals.

One other potential niche application of MOFs is their capability to selectively recognise chiral enantiomers. There are very few reports in the literature exploring the enantioselectivty capability of chiral MOFs and even fewer are computational. In Chapter 5, the enantioselectivity mechanism for a number of chiral diols in the chiral MOF [Ni_2(L-asp)$_2$(bipy)] was investigated by molecular simulations. The

simulations not only reproduced the preferential R-form adsorption observed in experiments from the framework derived from L-asp structure but also captured more subtle trends. The strong role of packing effects at high pore fillings on the better enantiomeric excess values for 1,3-butanediol in comparison with 1,2-butanediol and 1,2-propanediol was established. It was also demonstrated how subtle changes in the framework pore size lead to drastic changes in the magnitude and order of enantioselectivity of longer diol enantiomers (i.e. pentanediols). It was concluded that not only the chiral environment and the channel surface chemistry favour the uptake of one of the enantiomers but that a more prominent factor for obtaining high adsorption preference and guest-host recognition is the perfect match in terms of size and shape between the framework and guest molecules. These characteristics perfectly fit the synthetic flexibility in MOFs that enables considerable control over pore size and pore shape. This level of diversity is absent from traditional chiral separation techniques such as chiral receptors in chromatography. Developing rapid computational screening techniques using a library of chiral ligands (i.e. amino acid based) for the separation of target chiral molecules should be the focus of future work.

In this work, it was shown how the network topology and pore size in MOFs influence the distribution of mixtures in the adsorbed phase by means of molecular simulations. The reported preferential adsorption and selectivity along with underlying molecular interaction predictions can be used to further tailor MOFs for targeted applications. Finally, the results in this work provide valuable information for experimentalists and industrialists to develop and better assess the intriguing characteristics of MOFs as potential adsorbents for separation purposes.

References

Alaerts, L., M. Maes, L. Giebeler, P. A. Jacobs, J. A. Martens, J. F. M. Denayer, C. E. A. Kirschhock & D. E. De Vos (2008). Selective adsorption and separation of ortho-substituted alkylaromatics with the microporous aluminum terephthalate MIL-53. *Journal of the American Chemical Society,* 130**,** 14170-14178.

Alaerts, L., M. Maes, P. A. Jacobs, J. F. M. Denayer & D. E. De Vos (2008). Activation of the metal-organic framework MIL-47 for selective adsorption of xylenes and other difunctionalized aromatics. *Physical Chemistry Chemical Physics,* 10**,** 2979-2985.

Alavi, S., N. A. Afagh, J. A. Ripmeester & D. L. Thompson (2006). Molecular dynamics simulations of p-tert-butylcalix[4]arene with small guest molecules. *Chemistry – A European Journal,* 12**,** 5231-5237.

Alavi, S. & J. A. Ripmeester (2008). Simulations of p-tert-butylcalix[4]arene with multiple occupancies of small guest molecules. *Chemistry – A European Journal,* 14**,** 1965-1971.

Alavi, S., T. K. Woo, A. Sirjoosingh, S. Lang, I. Moudrakovski & J. A. Ripmeester (2010). Hydrogen adsorption and diffusion in p-tert-butylcalix[4]arene: An experimental and molecular simulation study. *Chemistry – A European Journal,* 16**,** 11689-11696.

Allen, P. & D. J. Tildesley (1989). *Computer simulation of liquids,* Oxford, Clarendon Press.

Amirjalayer, S., M. Tafipolsky & R. Schmid (2007). Molecular dynamics simulation of benzene diffusion in MOF-5: Importance of lattice dynamics. *Angewandte Chemie International Edition,* 46**,** 463-466.

Ananchenko, G. S., I. L. Moudrakovski, A. W. Coleman & J. A. Ripmeester (2008). A channel-free soft-walled capsular calixarene solid for gas adsorption. *Angewandte Chemie International Edition,* 47**,** 5616-5618.

Atwood, J. L., L. J. Barbour, P. K. Thallapally & T. B. Wirsig (2005). A crystalline organic substrate absorbs methane under STP conditions. *Chemical Communications***,** 51-53.

Bao, X., L. J. Broadbelt & R. Q. Snurr (2010). Elucidation of consistent enantioselectivity for a homologous series of chiral compounds in homochiral metal-organic frameworks. *Physical Chemistry Chemical Physics,* 12**,** 6466-6473.

Bao, X., R. Q. Snurr & L. J. Broadbelt (2009). Collective effects of multiple chiral selectors on enantioselective adsorption. *Langmuir,* 25**,** 10730-10736.

Bárcia, P. S., M. P. M. Nicolau, J. M. Gallegos, B. Chen, A. E. Rodrigues & J. A. C. Silva (2012). Modeling adsorption equilibria of xylene isomers in a microporous metal–organic framework. *Microporous and Mesoporous Materials,* 155**,** 220-226.

Barthelet, K., J. Marrot, G. Ferey & D. Riou (2004). VIII(OH){O2C-C6H4-CO2}.(HO2C-C6H4-CO2H)(DMF)(H2O) (or MIL-68), a new vanadocarboxylate with a large pore hybrid topology : Reticular synthesis with infinite inorganic building blocks? *Chemical Communications***,** 520-521.

Barthelet, K., J. Marrot, D. Riou & G. Férey (2002). A breathing hybrid organic–inorganic solid with very large pores and high magnetic characteristics. *Angewandte Chemie International Edition,* 41**,** 281-284.

Bew, S. P., A. D. Burrows, T. Düren, M. F. Mahon, P. Z. Moghadam, V. M. Sebestyen & S. Thurston (2012). Calix[4]arene-based metal-organic frameworks: Towards hierarchically porous materials. *Chemical Communications,* 48**,** 4824-4826.

Bradshaw, D., T. J. Prior, E. J. Cussen, J. B. Claridge & M. J. Rosseinsky (2004). Permanent microporosity and enantioselective sorption in a chiral open framework. *Journal of the American Chemical Society,* 126**,** 6106-6114.

Breneman, C. M. & K. B. Wiberg (1990). Determining atom-centered monopoles from molecular electrostatic potentials. The need for high sampling density in formamide conformational analysis. *Journal of Computational Chemistry,* 11**,** 361-373.

Brunauer, S., P. H. Emmett & E. Teller (1938). Adsorption of gases in multimolecular layers. *Journal of the American Chemical Society,* 60**,** 309-319.

Castillo, J. M., T. J. H. Vlugt & S. Calero (2009). Molecular simulation study on the separation of xylene isomers in MIL-47 metal-organic frameworks. *Journal of Physical Chemistry C,* 113**,** 20869-20874.

Čejka, J. (2012). Metal-organic frameworks. Applications from catalysis to gas storage. *Angewandte Chemie International Edition,* 51**,** 4782-4783.

Chen, B., J. J. Potoff & J. I. Siepmann (2001). Monte carlo calculations for alcohols and their mixtures with alkanes. Transferable potentials for phase equilibria. 5. United-atom description of primary, secondary, and tertiary alcohols. *Journal of Physical Chemistry B,* 105**,** 3093-3104.

Chen, B. Q., D. Q. Yuan, M. Y. Wu, F. L. Jiang & M. C. Hong (2009). Two coordination networks built from p-sulfonatothiacalix[4]arene tetranuclear clusters. *Zeitschrift fur Anorganische und Allgemeine Chemie,* 635**,** 1669-1672.

Chen, L., C. A. Morrison & T. Düren (2012). Improving predictions of gas adsorption in metal–organic frameworks with coordinatively unsaturated metal sites: Model potentials, ab initio parameterization, and gcmc simulations. *The Journal of Physical Chemistry C,* 116**,** 18899-18909.

Dalgarno, S. J., M. J. Hardie, J. L. Atwood & C. L. Raston (2004). Bilayers, corrugated bilayers, and coordination polymers of p-sulfonatocalix[6]arene. *Inorganic Chemistry,* 43**,** 6351-6356.

Dalgarno, S. J., M. J. Hardie & C. L. Raston (2004). PH-dependent formation of molecular capsules and coordination polymers. *Crystal Growth & Design,* 4**,** 227-234.

Dan-Hardi, M., C. Serre, T. Frot, L. Rozes, G. Maurin, C. Sanchez & G. Férey (2009). A new photoactive crystalline highly porous titanium(iv) dicarboxylate. *Journal of the American Chemical Society,* 131**,** 10857-10859.

Daschbach, J. L., X. Sun, T.-M. Chang, P. K. Thallapally, B. P. McGrail & L. X. Dang (2009). Computational studies of load-dependent guest dynamics and free energies of inclusion for CO_2 in low-density p-tert-butylcalix[4]arene at loadings up to 2:1. *The Journal of Physical Chemistry A,* 113**,** 3369-3374.

Dhakshinamoorthy, A., M. Alvaro & H. Garcia (2012). Commercial metal organic frameworks as heterogeneous catalysts. *Chemical Communications,* 10.1039/C2CC34329K.

Dubbeldam, D., S. Calero, D. E. Ellis & R. Q. Snurr (2008). Raspa 1.0. *RASPA 1.0, Northwestern University: Evanston, IL*.

Dufner, H., S. M. Kast, J. Brickmann & M. Schlenkrich (1997). Ewald summation versus direct summation of shifted-force potentials for the calculation of electrostatic interactions in solids: A quantitative study. *Journal of Computational Chemistry,* 18**,** 660-676.

Dunne, L. J. & G. Manos (2009). *Adsorption and phase behaviour in nanochannels and nanotubes,* London, Springer.

Düren, T., Y.-S. Bae & R. Q. Snurr (2009). Using molecular simulation to characterise metal-organic frameworks for adsorption applications. *Chemical Society Reviews,* 38**,** 1237-1247.

Düren, T., F. Millange, G. Férey, K. S. Walton & R. Q. Snurr (2007). Calculating geometric surface areas as a characterization tool for metal−organic frameworks. *The Journal of Physical Chemistry C,* 111**,** 15350-15356.

Dybtsev, D. N., A. L. Nuzhdin, H. Chun, K. P. Bryliakov, E. P. Talsi, V. P. Fedin & K. Kim (2006). A homochiral metal–organic material with permanent porosity, enantioselective sorption properties, and catalytic activity. *Angewandte Chemie International Edition,* 45**,** 916-920.

Enright, G. D., K. A. Udachin, I. L. Moudrakovski & J. A. Ripmeester (2003). Thermally programmable gas storage and release in single crystals of an organic van der waals host. *Journal of the American Chemical Society,* 125**,** 9896-9897.

Farrusseng, D., S. Aguado & C. Pinel (2009). Metal–organic frameworks: Opportunities for catalysis. *Angewandte Chemie International Edition,* 48**,** 7502-7513.

Farrusseng, D., C. Daniel, C. Gaudillère, U. Ravon, Y. Schuurman, C. Mirodatos, D. Dubbeldam, H. Frost & R. Q. Snurr (2009). Heats of adsorption for seven gases in three metal−organic frameworks: Systematic comparison of experiment and simulation. *Langmuir,* 25**,** 7383-7388.

Finsy, V., C. E. A. Kirschhock, G. Vedts, M. Maes, L. Alaerts, D. E. De Vos, G. V. Baron & J. F. M. Denayer (2009). Framework breathing in the vapour-phase adsorption and separation of xylene isomers with the metal–organic framework MIL-53. *Chemistry – A European Journal,* 15**,** 7724-7731.

Ford, D. C., D. Dubbeldam & R. Q. Snurr (2009). The effect of framework flexibility on diffusion of small molecules in the metal–organic framework IRMOF-1. *diffusion-fundamentals.org,* 11**,** 1-8.

Frenkel, D. & B. Smit (2002). *Understanding molecular simulation: From algorithms to applications,* 2nd edition, Academic Press.

Frisch, M. J., G. W. Trucks, H. B. Schlegel, G. E. Scuseria, M. A. Robb, J. R. Cheeseman, G. Scalmani, V. Barone, B. Mennucci, G. A. Petersson, H. Nakatsuji, M. Caricato, X. Li, H. P. Hratchian, A. F. Izmaylov, J. Bloino, G. Zheng, J. L. Sonnenberg, M. Hada, M. Ehara, K. Toyota, R. Fukuda, J. Hasegawa, M. Ishida, T. Nakajima, Y. Honda, O. Kitao, H. Nakai, T. Vreven, J. Montgomery, J. A., J. E. O. Peralta, F., M. Bearpark, J. J. Heyd, E. Brothers, K. N. Kudin, V. N. Staroverov, R. Kobayashi, J. Normand, K. Raghavachari, A. Rendell, J. C. Burant, S. S. Iyengar, J. Tomasi, M. Cossi, N. Rega, N. J. Millam, M. Klene, J. E. Knox, J. B. Cross, V. Bakken, C. Adamo, J. Jaramillo, R. Gomperts, R. E. Stratmann, O. Yazyev, A. J. Austin, R. Cammi, C. Pomelli, J. W. Ochterski, R. L. Martin, K. Morokuma, V. G. Zakrzewski, G. A. Voth, P. Salvador, J. J. Dannenberg, S. Dapprich, A. D. Daniels, Ö. Farkas, J. B. Foresman, J. V. Ortiz, J. Cioslowski & D. J. Fox (2009). Gaussian 09, revision a.02. *Gaussian, Inc., Wallingford CT, 2009.*

Gallo, M. & D. Glossman-Mitnik (2009). Fuel gas storage and separations by metal−organic frameworks: Simulated adsorption isotherms for H_2 and CH_4 and their equimolar mixture. *The Journal of Physical Chemistry C,* 113**,** 6634-6642.

Gelb, L. D. & K. E. Gubbins (1998). Pore size distributions in porous glasses: A computer simulation study. *Langmuir,* 15**,** 305-308.

Ghysels, A., M. Vandichel, T. Verstraelen, M. A. van der Veen, D. E. De Vos, M. Waroquier & V. Van Speybroeck (2012). Host-guest and guest-guest interactions between xylene isomers confined in the MIL-47(v) pore system. *Theoretical Chemistry Accounts,* 131.

Goodbody, S. J., K. Watanabe, D. MacGowan, J. P. R. B. Walton & N. Quirke (1991). Molecular simulation of methane and butane in silicalite. *Journal of the Chemical Society, Faraday Transactions,* 87**,** 1951-1958.

Greathouse, J. A., T. L. Kinnibrugh & M. D. Allendorf (2009). Adsorption and separation of noble gases by IRMOF-1: Grand canonical monte carlo simulations. *Industrial & Engineering Chemistry Research,* 48**,** 3425-3431.

Greathouse, J. A., N. W. Ockwig, L. J. Criscenti, T. R. Guilinger, P. Pohl & M. D. Allendorf (2010). Computational screening of metal-organic frameworks for large-molecule chemical sensing. *Physical Chemistry Chemical Physics,* 12**,** 12621-12629.

Gu, Z.-Y., D.-Q. Jiang, H.-F. Wang, X.-Y. Cui & X.-P. Yan (2009). Adsorption and separation of xylene isomers and ethylbenzene on two zn−terephthalate metal−organic frameworks. *The Journal of Physical Chemistry C,* 114**,** 311-316.

Gu, Z.-Y. & X.-P. Yan (2010). Metal–organic framework MIL-101 for high-resolution gas-chromatographic separation of xylene isomers and ethylbenzene. *Angewandte Chemie International Edition,* 49**,** 1477-1480.

Gübitz, G. & M. G. Schmid (2001). Chiral separation by chromatographic and electromigration techniques. A review. *Biopharmaceutics & Drug Disposition,* 22**,** 291-336.

Guo, G.-Q., H. Chen & Y.-C. Long (2000). Separation of p-xylene from C8 aromatics on binder-free hydrophobic adsorbent of MFI zeolite. I. Studies on static equilibrium. *Microporous and Mesoporous Materials,* 39**,** 149-161.

Gupta, A., S. Chempath, M. J. Sanborn, L. A. Clark & R. Q. Snurr (2003). Object-oriented programming paradigms for molecular modeling. *Molecular Simulation,* 29**,** 29-46.

Gutsche, C. D. (1998). *Calixarenes revisited,* Cambridge, Royal Society of Chemistry.

Hafizovic, J., M. Bjørgen, U. Olsbye, P. D. C. Dietzel, S. Bordiga, C. Prestipino, C. Lamberti & K. P. Lillerud (2007). The inconsistency in adsorption properties and powder XRD data of MOF-5 is rationalized by framework interpenetration and the presence of organic and inorganic species in the nanocavities. *Journal of the American Chemical Society,* 129**,** 3612-3620.

Haile, J. M. (1997). *Molecular dynamics simulation: Elementary methods,* New york, John Wiley & Sons.

Hao, H.-Q., Z.-J. Lin, S. Hu, W.-T. Liu, Y.-Z. Zheng & M.-L. Tong (2010). Nanoporous metal-organic framework comprising of 1D cobalt oxalate chains and flexible ligands exhibiting both dynamic gas adsorption and antiferromagnetic chain behaviours. *CrystEngComm,* 12**,** 2225-2231.

Hare, P. E. & E. Gilav (1979). Separation of D-amino and L-amino-acids by liquid-chromatography - use of chiral eluants. *Science,* 204**,** 1226-1228.

Hattori, H., M. Iwai, S. Kurono, T. Yamada, K. Watanabe-Suzuki, A. Ishii, H. Seno & O. Suzuki (1998). Sensitive determination of xylenes in whole blood by capillary gas chromatography with cryogenic trapping. *Journal of Chromatography B: Biomedical Sciences and Applications,* 718**,** 285-289.

Herm, Z. R., R. Krishna & J. R. Long (2012). CO_2/CH_4, CH_4/H_2 and $CO_2/CH_4/H_2$ separations at high pressures using Mg2(DOBDC). *Microporous and Mesoporous Materials,* 151**,** 481-487.

Hill, T. L. (1960). *An introduction to statistical thermodynamics,* Reading, Addison-Wesley.

Hinks, N. J., A. C. McKinlay, B. Xiao, P. S. Wheatley & R. E. Morris (2010). Metal organic frameworks as no delivery materials for biological applications. *Microporous and Mesoporous Materials,* 129**,** 330-334.

Huxford, R. C., J. Della Rocca & W. Lin (2010). Metal–organic frameworks as potential drug carriers. *Current Opinion in Chemical Biology,* 14**,** 262-268.

Hyun, M. H., S. C. Han & S. H. Whangbo (2003). New ligand exchange chiral stationary phase for the liquid chromatographic resolution of alpha- and beta-amino acids. *Journal of Chromatography A,* 992**,** 47-56.

Isaeva, V. & L. Kustov (2010). The application of metal-organic frameworks in catalysis (review). *Petroleum Chemistry,* 50**,** 167-180.

Jorgensen, W. L. (1986). Optimized intermolecular potential functions for liquid alcohols. *Journal of Physical Chemistry,* 90**,** 1276-1284.

Jorgensen, W. L., D. S. Maxwell & J. Tirado-Rives (1996). Development and testing of the OPLS all-atom force field on conformational energetics and properties of organic liquids. *Journal of the American Chemical Society,* 118**,** 11225-11236.

Jorgensen, W. L. & T. B. Nguyen (1993). Monte-carlo simulations of the hydration of substituted benzenes with OPLS potential functions. *Journal of Computational Chemistry,* 14**,** 195-205.

Kang, I. J., N. A. Khan, E. Haque & S. H. Jhung (2011). Chemical and thermal stability of isotypic metal–organic frameworks: Effect of metal ions. *Chemistry – A European Journal,* 17**,** 6437-6442.

Kärger, J. & D. M. Ruthven (1992). *Diffusion in zeolites and other microporous solids,* New York, John Wiley.

Kennedy, S., G. Karotsis, C. M. Beavers, S. J. Teat, E. K. Brechin & S. J. Dalgarno (2010). Metal–organic calixarene nanotubes. *Angewandte Chemie International Edition,* 49**,** 4205-4208.

Keskin, S., J. Liu, R. B. Rankin, J. K. Johnson & D. S. Sholl (2009). Progress, opportunities, and challenges for applying atomically detailed modeling to molecular adsorption and transport in metal-organic framework materials. *Industrial & Engineering Chemistry Research,* 48**,** 2355-2371.

Keskin, S. & D. S. Sholl (2009). Efficient methods for screening of metal organic framework membranes for gas separations using atomically detailed models. *Langmuir,* 25**,** 11786-11795.

Konstas, K., T. Osl, Y. Yang, M. Batten, N. Burke, A. J. Hill & M. R. Hill (2012). Methane storage in metal organic frameworks. *Journal of Materials Chemistry,* 22**,** 16698-16708.

Krishna, R. (2009). Describing the diffusion of guest molecules inside porous structures. *Journal of Physical Chemistry C,* 113**,** 19756-19781.

Kulprathipanja, S. (2010). *Zeolites in industrial separation and catalysis,* Glasgow, John Wiley & Sons.

Kurup, A. S., K. Hidajat & A. K. Ray (2005). Optimal operation of an industrial-scale parex process for the recovery of p-xylene from a mixture of C8 aromatics. *Ind Eng Chem Res,* 44**,** 5703-5714.

Lachet, V., A. Boutin, B. Tavitian & A. H. Fuchs (1999). Molecular simulation of p-xylene and m-xylene adsorption in y zeolites. Single components and binary mixtures study. *Langmuir,* 15**,** 8678-8685.

Lee, J., O. K. Farha, J. Roberts, K. A. Scheidt, S. T. Nguyen & J. T. Hupp (2009). Metal-organic framework materials as catalysts. *Chemical Society Reviews,* 38**,** 1450-1459.

Li, J.-R., R. J. Kuppler & H.-C. Zhou (2009). Selective gas adsorption and separation in metal-organic frameworks. *Chemical Society Reviews,* 38**,** 1477-1504.

Li, J.-R., Y. Ma, M. C. McCarthy, J. Sculley, J. Yu, H.-K. Jeong, P. B. Balbuena & H.-C. Zhou (2011). Carbon dioxide capture-related gas adsorption and separation in metal-organic frameworks. *Coordination Chemistry Reviews,* 255**,** 1791-1823.

Li, W., S. Grimme, H. Krieg, J. Möllmann & J. Zhang (2012). Accurate computation of gas uptake in microporous organic molecular crystals. *The Journal of Physical Chemistry C,* 116**,** 8865-8871.

Liu, B., O. Shekhah, H. K. Arslan, J. Liu, C. Wöll & R. A. Fischer (2012). Enantiopure metal–organic framework thin films: Oriented surmof growth and enantioselective adsorption. *Angewandte Chemie International Edition,* 51**,** 807-810.

Liu, J., J. T. Culp, S. Natesakhawat, B. C. Bockrath, B. Zande, S. G. Sankar, G. Garberoglio & J. K. Johnson (2007). Experimental and theoretical studies of gas adsorption in Cu-3(btc)(2): An effective activation procedure. *Journal of Physical Chemistry C,* 111**,** 9305-9313.

Liu, J. & J. Johnson (2009). Prediction of CH_4/H_2 mixture selectivity in zn(tbip) from computer simulations. *Journal of Low Temperature Physics,* 157**,** 268-276.

Liu, Y. B., W. P. Liao, Y. F. Bi, X. F. Wang & H. J. Zhang (2009). Assembly of seven supramolecular compounds with p-sulfonatocalix[6]arene. *Crystal Growth & Design,* 9**,** 5311-5318.

Ma, L., J. M. Falkowski, C. Abney & W. Lin (2010). A series of isoreticular chiral metal–organic frameworks as a tunable platform for asymmetric catalysis. *Nat Chem,* 2**,** 838-846.

Ma, S. (2009). Gas adsorption applications of porous metal-organic frameworks. *Pure and Applied Chemistry,* 81**,** 2235-2251.

Mayo, S. L., B. D. Olafson & W. A. Goddard (1990). Dreiding: A generic force field for molecular simulations. *The Journal of Physical Chemistry,* 94**,** 8897-8909.

McKinlay, A. C., R. E. Morris, P. Horcajada, G. Férey, R. Gref, P. Couvreur & C. Serre (2010). Biomofs: Metal–organic frameworks for biological and medical applications. *Angewandte Chemie International Edition,* 49**,** 6260-6266.

Meek, S. T., J. A. Greathouse & M. D. Allendorf (2011). Metal-organic frameworks: A rapidly growing class of versatile nanoporous materials. *Advanced Materials,* 23**,** 249-267.

Metropolis, N., A. Rosenbluth, M. Rosenbluth, A. Teller & E. Teller (1953). Equation of state calculations by fast computing machines. *Journal of Chemical Physics,* 21.

Mikami, K. & S. Matsukawa (1997). Asymmetric synthesis by enantiomer-selective activation of racemic catalysts. *Nature,* 385**,** 613-615.

Miller, S. R., P. A. Wright, C. Serre, T. Loiseau, J. Marrot & G. Ferey (2005). A microporous scandium terephthalate, Sc2(O2CC6H4CO2)3, with high thermal stability. *Chemical Communications***,** 3850-3852.

Minceva, M. & A. E. Rodrigues (2005). Uop´s parex: Modeling, simulation and optimization. *Enpromer, Brasil*.

Moreira, M. A., J. C. Santos, A. F. P. Ferreira, J. M. Loureiro, F. Ragon, P. Horcajada, K.-E. Shim, Y.-K. Hwang, U. H. Lee, J.-S. Chang, C. Serre & A. E. Rodrigues (2012). Reverse shape selectivity in the liquid-phase adsorption of xylene isomers in zirconium terephthalate mof UIO-66. *Langmuir,* 28**,** 5715-5723.

Murray, L. J., M. Dinca & J. R. Long (2009). Hydrogen storage in metal-organic frameworks. *Chemical Society Reviews,* 38**,** 1294-1314.

Nijem, N., H. Wu, P. Canepa, A. Marti, K. J. Balkus, T. Thonhauser, J. Li & Y. J. Chabal (2012). Tuning the gate opening pressure of metal–organic frameworks (mofs) for the selective separation of hydrocarbons. *Journal of the American Chemical Society,* 134**,** 15201-15204.

Olguin, J., A. Castillo, V. Gomez-Vidales, S. Hernandez-Ortega, R. A. Toscano, E. Munoz & I. Castillo (2009). Construction of acetate-bridged dicopper(ii) hybrid organic-inorganic networks with calix[4]arene-derived nitrogenous ligands. *Supramolecular Chemistry,* 21**,** 502-509.

Padmanaban, M., P. Muller, C. Lieder, K. Gedrich, R. Grunker, V. Bon, I. Senkovska, S. Baumgartner, S. Opelt, S. Paasch, E. Brunner, F. Glorius, E. Klemm & S. Kaskel (2011). Application of a chiral metal-organic framework in enantioselective separation. *Chemical Communications,* 47**,** 12089-12091.

Perles, J., M. Iglesias, M.-Á. Martín-Luengo, M. Á. Monge, C. Ruiz-Valero & N. Snejko (2005). Metal−organic scandium framework: Useful material for hydrogen storage and catalysis. *Chemistry of Materials,* 17**,** 5837-5842.

Pham, M.-H., G.-T. Vuong, A.-T. Vu & T.-O. Do (2011). Novel route to size-controlled Fe–MIL-88b–NH2 metal–organic framework nanocrystals. *Langmuir,* 27**,** 15261-15267.

Pichon, A., A. Lazuen-Garay & S. L. James (2006). Solvent-free synthesis of a microporous metal-organic framework. *CrystEngComm,* 8**,** 211-214.

Ramsahye, N. A., G. Maurin, S. Bourrelly, P. L. Llewellyn, T. Loiseau, C. Serre & G. Ferey (2007). On the breathing effect of a metal-organic framework upon

co2 adsorption: Monte carlo compared to microcalorimetry experiments. *Chemical Communications***,** 3261-3263.

Rapaport, D. C. (1995). *The art of molecular dynamics simulation,* Cambridge, Cambridge University Press.

Rappe, A. K., C. J. Casewit, K. S. Colwell, W. A. Goddard & W. M. Skiff. 1992. *Uff, a full periodic table force field for molecular mechanics and molecular dynamics simulations.* 114, American Chemical Society.

Rappe, A. K., C. J. Casewit, K. S. Colwell, W. A. Goddard & W. M. Skiff (1992). UFF, a full periodic table force field for molecular mechanics and molecular dynamics simulations. *Journal of the American Chemical Society,* 114**,** 10024-10035.

Rekoske, J. E. (2001). Chiral separations. *AIChE Journal,* 47**,** 2-5.

Ripmeester, J. A., G. D. Enright, C. I. Ratcliffe, K. A. Udachin & I. L. Moudrakovski (2006). What we have learned from the study of solid p-tert-butylcalix[4]arene compounds. *Chemical Communications***,** 4986-4996.

Rodríguez-Ropero, F., D. Zanuy & C. Alemán (2008). Molecular dynamics of a calix[4]arene-containing polymer in dichloromethane solution: Ability of the solvent molecules to fill the cavity of the macrocycle. *Journal of Computational Chemistry,* 29**,** 1233-1241.

Rouquerol, J., D. Avnir, C. W. Fairbridge, D. H. Everett, J. H. Haynes, N. Pernicone, J. D. F. Ramsay, K. S. W. Sing & K. K. Unger (1994). Recommendations for the characterization of porous solids. *Pure and Applied Chemistry,* 66**,** 1739-1758.

Sarkisov, L. & A. Harrison (2011). Computational structure characterisation tools in application to ordered and disordered porous materials. *Molecular Simulation,* 37**,** 1248-1257.

Scheirs, J. & T. E. Long (2005). *Modern polyesters: Chemistry and technology of polyesters and copolyesters,* Edithvale, John Wiley & Sons.

Schröder, M. (2010). *Functional metal-organic frameworks: Gas storage, separation and catalysis,* Heidelberg, Springer.

Seo, J. S., D. Whang, H. Lee, S. I. Jun, J. Oh, Y. J. Jeon & K. Kim (2000). A homochiral metal-organic porous material for enantioselective separation and catalysis. *Nature,* 404**,** 982-986.

Serre, C., F. Millange, C. Thouvenot, M. Noguès, G. Marsolier, D. Louër & G. Férey (2002). Very large breathing effect in the first nanoporous chromium(iii)-based solids: MIL-53 or CrIII(OH)·{O2C−C6H4−CO2}·{HO2C−C6H4−CO2H}x·H2Oy. *Journal of the American Chemical Society,* 124**,** 13519-13526.

Sheldon, R. A. (1993). *Chirotechnology: Industrial synthesis of optically active compounds,* New York, Marcel Dekker, INC.

Shiau, L.-D., C.-C. Wen & B.-S. Lin (2008). Separation of p-xylene from the multicomponent xylene system by stripping crystallization. *AIChE Journal,* 54**,** 337-342.

Sholl, D. & J. A. Steckel (2009). *Density functional theory: A practical introduction,* Hoboken, John Wiley & Sons.

Skoulidas, A. I. & D. S. Sholl (2005). Self-diffusion and transport diffusion of light gases in metal-organic framework materials assessed using molecular dynamics simulations. *Journal of Physical Chemistry B,* 109**,** 15760-15768.

Sun, D., Y. Ke, D. J. Collins, G. A. Lorigan & H.-C. Zhou (2007). Construction of robust open metal−organic frameworks with chiral channels and permanent porosity. *Inorganic Chemistry,* 46**,** 2725-2734.

Tafipolsky, M., S. Amirjalayer & R. Schmid (2010). First-principles-derived force field for copper paddle-wheel-based metal−organic frameworks. *The Journal of Physical Chemistry C,* 114**,** 14402-14409.

Tang, L., L. Shi, C. Bonneau, J. Sun, H. Yue, A. Ojuva, B.-L. Lee, M. Kritikos, R. G. Bell, Z. Bacsik, J. Mink & X. Zou (2008). A zeolite family with chiral and achiral structures built from the same building layer. *Nat Mater,* 7**,** 381-385.

Thallapally, P. K., G. O. Lloyd, T. B. Wirsig, M. W. Bredenkamp, J. L. Atwood & L. J. Barbour (2005). Organic crystals absorb hydrogen gas under mild conditions. *Chemical Communications***,** 5272-5274.

Thallapally, P. K., B. P. McGrail & J. L. Atwood (2007). Sorption of nitrogen oxides in a nonporous crystal. *Chemical Communications***,** 1521-1523.

Tranchemontagne, D. J., J. R. Hunt & O. M. Yaghi (2008). Room temperature synthesis of metal-organic frameworks: MOF-5, MOF-74, MOF-177, MOF-199, and IRMOF-0. *Tetrahedron,* 64**,** 8553-8557.

Vaidhyanathan, R., D. Bradshaw, J.-N. Rebilly, J. P. Barrio, J. A. Gould, N. G. Berry & M. J. Rosseinsky (2006). A family of nanoporous materials based on an amino acid backbone. *Angewandte Chemie International Edition,* 45**,** 6495-6499.

Vermoortele, F., M. Maes, P. Z. Moghadam, M. J. Lennox, F. Ragon, M. Boulhout, S. Biswas, K. G. M. Laurier, I. Beurroies, R. Denoyel, M. Roeffaers, N. Stock, T. Düren, C. Serre & D. E. De Vos (2011). P-xylene-selective metal–organic frameworks: A case of topology-directed selectivity. *Journal of the American Chemical Society,* 133**,** 18526-18529.

Wang, L. (2012). *Molecular dynamics - theoretical developments and applications in nanotechnology and energy,* Rijeka, InTech.

Wee, L. H., L. Alaerts, J. A. Martens & D. De Vos (2011). *Metal–organic frameworks as catalysts for organic reactions, in metal-organic frameworks: Applications from catalysis to gas storage (ed d. Farrusseng),* Weinheim, Wiley-VCH Verlag GmbH & Co. KGaA.

Weissermel, K. & H. J. Arpe (2008). *Industrial organic chemistry,* Weinheim, John Wiley & Sons.

Wilmer, C. E., M. Leaf, C. Y. Lee, O. K. Farha, B. G. Hauser, J. T. Hupp & R. Q. Snurr (2012). Large-scale screening of hypothetical metal–organic frameworks. *Nat Chem,* 4**,** 83-89.

Wolf, D., P. Keblinski, S. R. Phillpot & J. Eggebrecht (1999). Exact method for the simulation of coulombic systems by spherically truncated, pairwise r(-1) summation. *Journal of Chemical Physics,* 110**,** 8254-8282.

Won, E., Y. Jin & D.-Y. Jung (2002). A coordination polymer of cobalt(II)−glutarate: Two-dimensional interlocking structure by dicarboxylate ligands with two different conformations. *Inorganic Chemistry,* 41**,** 501-506.

Wu, D., C. Wang, B. Liu, D. Liu, Q. Yang & C. Zhong (2012). Large-scale computational screening of metal-organic frameworks for CH_4/H_2 separation. *AIChE Journal,* 58**,** 2078-2084.

Xiang, S., Y. He, Z. Zhang, H. Wu, W. Zhou, R. Krishna & B. Chen (2012). Microporous metal-organic framework with potential for carbon dioxide capture at ambient conditions. *Nature Communications 3***,** doi:10.1038/ncomms1956.

Xie, S.-M., Z.-J. Zhang, Z.-Y. Wang & L.-M. Yuan (2011). Chiral metal–organic frameworks for high-resolution gas chromatographic separations. *Journal of the American Chemical Society,* 133**,** 11892-11895.

Xuan, W., C. Zhu, Y. Liu & Y. Cui (2012). Mesoporous metal-organic framework materials. *Chemical Society Reviews,* 41**,** 1677-1695.

Yang, Q., S. Vaesen, M. Vishnuvarthan, F. Ragon, C. Serre, A. Vimont, M. Daturi, G. De Weireld & G. Maurin (2012). Probing the adsorption performance of the hybrid porous MIL-68(Al): A synergic combination of experimental and modelling tools. *Journal of Materials Chemistry,* 22**,** 10210-10220.

Yang, Q. & C. Zhong (2005). Molecular simulation of adsorption and diffusion of hydrogen in metal−organic frameworks. *The Journal of Physical Chemistry B,* 109**,** 11862-11864.

Yang, Q. & C. Zhong (2006). Molecular simulation of carbon dioxide/methane/hydrogen mixture adsorption in metal−organic frameworks. *The Journal of Physical Chemistry B,* 110**,** 17776-17783.

Yassaa, N., E. Brancaleoni, M. Frattoni & P. Ciccioli (2006). Isomeric analysis of btexs in the atmosphere using β-cyclodextrin capillary chromatography coupled with thermal desorption and mass spectrometry. *Chemosphere,* 63**,** 502-508.

Yazaydin, A. O., R. Q. Snurr, T.-H. Park, K. Koh, J. Liu, M. D. LeVan, A. I. Benin, P. Jakubczak, M. Lanuza, D. B. Galloway, J. J. Low & R. R. Willis (2009). Screening of metal−organic frameworks for carbon dioxide capture from flue gas using a combined experimental and modeling approach. *Journal of the American Chemical Society,* 131**,** 18198-18199.

Nomenclature

Roman letters

a_i	acceleration of *i*-th atom
A	macroscopic property
A_i	property A in microstate *i*
$\langle A \rangle$	ensemble average for macroscopic property A
D_s	self-diffusion
E	energy
E_i	energy of microstate *i*
f	fugacity
F_i	force acting upon *i*-th atom
h	Planck's constant
K	force constants (bond stretching, bending and torsion)
k_B	Boltzmann constant
m	mass of a molecule
n	new configuration
N	number of molecules
n_{ads}	amount adsorbed
o	old configuration
P	pressure
P	probability
P_i	probability of microstate *i*
q	point charge
Q	partition function for the canonical ensemble
r	position

r	distance between bonded atoms
$r^2(t)$	mean square displacement
r_{ij}	distance between interaction sites *i* and *j*
r_c	cut-off radius
r_{eq}	equilibrium distance between bonded atoms
S	selectivity
t	time
T	temperature
U	potential energy
U_{ij}	potential between two interaction sites *i* and *j*
V	volume
x_i	mole fraction of component *i* in the adsorbed phase
y_i	mole fraction of component *i* in the bulk phase
z	activity

Greek Letters

Λ	de Broglie wave length
Ξ	partition function of the grand canonical ensemble
β	$(k_B T)^{-1}$
ε	potential well depth
ε_{ij}	potential well depth for sites *i* and *j*
ε_0	permittivity in vacuum
θ	bond angle
θ_{eq}	equilibrium bond angle
μ	chemical potential
σ	Lennard-Jones diameter
σ_{ij}	Lennard-Jones diameter for sites *i* and *j*
ϕ	torsion angle
Φ	energy of a system